UNIVERSITÀ
DI PARMA

UNIVERSITÀ DEGLI STUDI DI PARMA

DOTTORATO DI RICERCA IN FISICA

CICLO XXXI

Enhancing muon spin spectroscopy: from atomistic simulation of muon implantation site to hyperfine coupling calculation.

Coordinatore:
Prof. Cristiano VIAPPIANI

Tutor:
Prof. Roberto DE RENZI

Co-tutor:
Dr. Pietro BONFÀ

Dottorando:
Ifeanyi John ONUORAH

Anni 2015-2018

Thesis Reviewers:
Prof. Matteo Calandra
Dr. Peter Baker

Commission of the final examination:

External:
Prof. Stephen Blundell
Prof. Alessandro Lascialfari

Internal:
Prof. Paolo Santini

Final examination:
25th February, 2019

Università degli studi di Parma, Dipartimento di Scienze Matematiche, Fisiche e Informatiche

Abstract

This thesis consists mainly of density functional theory (DFT) calculations, complemented by specific theoretical developments, to determine the implantation site of the positive muon and its magnetic hyperfine coupling in a range of selected materials, whose intriguing properties attract current scientific interest.

The study is mainly motivated considering that in muon spin spectroscopy (μSR), whereby matter is probed by means of implanted muons, the site of muon implantation and the value of the different contributions to their magnetic coupling with the host environment are not known *a-priori*. They are crucial towards understanding certain physical properties of the materials, since knowledge of the muon implantation sites, muon hyperfine coupling and extent of perturbation of the muon's local environment in the host allows important information, beyond the values of the best fit parameters, to be indirectly extracted from μSR spectra. Notable examples are the magnitude of total magnetic moments and even the spin structure of some magnetic materials.

The strategy for assigning the muon site with the DFT method is discussed and used successfully in the following selected materials; $NaFe_{1-x}Ni_xAs$, $Yb_2Pd_2In_{1-x}Sn_x$ and Sr_2RuO_4. Evidence for the coexistence of magnetism and superconductivity in $NaFe_{1-x}Ni_xAs$ is provided by μSR measurements and the moment size on Fe, crucial in the context of iron pnictides, is determined by means of dipole sum calculations at the muon sites identified by DFT. In $Yb_2Pd_2In_{1-x}Sn_x$, the muon sites are first calculated by DFT and then validated comparing a dipolar simulation with measured local fields. Furthermore, a steep increase in the measured muon local field by application of hydrostatic pressure at intermediate Sn doping is accounted for by assuming a transition to a different symmetry-allowed spin order. Lastly, the calculated muon implantation site in the superconducting Sr_2RuO_4 allows investigation of the extent of the muon perturbation and its effect on the time reversal symmetry breaking mechanism, in relation to the observation of this phenomenon with μSR in a very highly cited paper.

I then proceed to discuss a systematic analysis of the accuracy of the calculation of the *ab initio* estimation of muon hyperfine contact field on elemental transition metals, using the projector-augmented pseudopotential approach. This approach allows one to include the core state effects and accounts principally for the success of the calculated contact hyperfine field in Fe, Ni, Co. The same method is also used to calculate the contact field in non-centrosymmetric metallic compounds, presently of topical interest for their spiral magnetic structure giving rise to skyrmion phases, such as MnSi and MnGe. To further improve the accuracy of

the calculated contact hyperfine field, I addressed the zero point vibration of the muon, not captured in the DFT treatment within the Born-Oppenheimer approximation. A published stochastic self-consistent harmonic approximation method is further developed specifically for the very light muon and used to successfully average the effect of the muon zero point vibrations on the calculated contact hyperfine field, improving the accuracy of the results.

The last part of this thesis is the study of the charged and neutral states of hydrogen, an analogue of the implanted positive muon if one ignores zero point vibrations, in MnO and NiO. Hydrogen defect states at the band gap are observed to exist in these materials. The stability of these defect states is also discussed together with the magnetic coupling of the muon in the antiferromagnetically ordered transition metal mono-oxides. This allows to determine the easy axis of magnetization in MnO and NiO, a very subtle property to gain experimental access to, and a very nice example of the enhanced scope of μSR when used in conjunction with atomistic simulation.

Riassunto

Titolo: Potenziamento della spettroscopia di spin muonica: dalla simulazione atomistica del sito di localizzazione ai calcoli dell'accoppiamento iperfine del muone.

La tesi consiste principalmente in calcoli di teoria del funzionale densitá (DFT), integrati da sviluppi teorici specifici, rivolti a determinare il sito di impianto del muone positivo e il suo accoppiamento iperfine in una serie di materiali le cui proprietá singolari attraggono oggi notevole interesse.

Lo studio é motivato in primo luogo dal fatto che in spettroscopia di spin muonica (μSR) non sono noti a priori né il sito di impiantazione del muone né i diversi contributi al suo accoppiamento magnetico con il circondario all'interno della materia non sono noti a priori. Questi sono dati cruciali per ottenere alcune proprietá fisiche dei materiali, dato che la conoscenza del sito occupato dal muone, il suo accoppiamento iperfine e la rilevanza della perturbazione che esso introduce nell'immediato circondario consentono di estrarre ulteriore informazione indiretta dal best fit degli spettri, oltre ai puri valori dei parametri di fit. Esempi notevoli sono la grandezza dei momenti magnetici totali e persino la struttura di spin di alcuni materiali magnetici.

La strategia per assegnare il sito del muone con l'aiuto del metodo DFT é discussa ed utilizzata con successo in tre materiali selezionati, $NaFe_{1-x}Ni_xAs$, $Yb_2Pd_2In_{1-x}Sn_x$ and Sr_2RuO_4. La coesistenza di magnetismo e superconducttivitá in $NaFe_{1-x}Ni_xAs$ é evidenziata dai risultati di μSR e il momento magnetico del Fe, importante nel contesto dei pnictidi superconduttori, é stimato grazie all'attribuzione del sito del muone. Nel $Yb_2Pd_2In_{1-x}Sn_x$ drogato con Sn i siti del muone sono calcolati in DFT, e quindi convalidati dal confronto tra somme dipolari e campi locali misurati. Inoltre un'incremento brusco dei campi interni sotto pressione a drogaggio intermedio di Sn é ben giustificata assumendo una transizione ad un diverso ordine di spin compatibile con la simmetria. Per finire il sito calcolato in Sr_2RuO_4 consente di discutere la perturbazione introdotta dal muone nel suo circondario e il suo effetto sul meccanismo di time reversal symmetry breaking. Il contributo é significativo perché il time reversal symmetry breaking in Sr_2RuO_4 é evidenziato, non senza controversie, da un lavoro *highly cited* basato spettroscopia μSR.

Procedo quindi a discutere una analisi sistematica dell'accuratezza dei calcoli per la stima *ab initio* del campo iperfine di contatto al muone sui composti elementali di metalli di transizione utilizzando l'approccio degli pseudo-potenziali *projector-augmented*. Questo approccio permette di includere efficacemente il con-

tributo di *core* e rende conto prevalentemente del successo delle predizioni per Fe, Ni, Co. Lo stesso metodo é utilizzato anche per calcolare il campo di contatto nei composti non centrosimmetrici come MnGe e MnSi, di grande interesse attuale per le loro strutture magnetiche spirali che danno luogo a fasi skyrmioniche. Per migliorare l'accuratezza del campo iperfine di contatto ho affrontato l'influenza delle vibrazioni di punto zero del muone, ignorata nell'approssimazione di Born-Oppenheimer, a causa della massa leggere del muone. L'approssimazione armonica stocastica autoconsistente, giá nota in letteratura, é stata sviluppata ulteriormente per il muone molto leggero e utilizzata con successo per migliorare il confronto tra risultati ed esperimento.

L'ultima parte di questa tesi presenta uno studio dei diversi stati di carica dell'idrogeno, analogo al muone positivo se si ignora l'energia di punto zero, nel caso di MnO e NiO. Difetti di idrogeno consistenti in stati localizzati nella gap sono stati osservati in questi due materiali. La loro stabilitá viene discussa qui assieme all'accoppiamento magnetico dell'idrogeno (muone) nello stato atiferromagnetico dei monossidi di metalli di transizione. Ció consente di determinare l'asse facile di magnetizzazione del MnO e NiO, una proprietá molto difficile da misurare sperimentalmente e al contempo un ottimo esempio del maggior potenziale di indagine della μSR, se assistita da simulazione atomistica.

Contents

List of Figures

List of Tables

Notations

List of Abbreviations

AFM	Antiferromagnet
BFGS	Broyden–Fletcher–Goldfarb–Shanno
BO	Born-Oppenheimer
BTRS	Broken Time Reversal Symmetry
CBM	Conduction Band Minimum
CG	Conjugate Gradient
DBO	Double Born-Oppenheimer
DFT	Density Functional Theory
DOS	Density of States
ESR	Electron Spin Resonance
FM	Ferromagnet
GGA	Generalized Gradient Approximation
GPU	Graphics processing units
HPC	High performance computing
HTS	High Temperature Superconductors
IRs	Irreducible Representations
LDA	Local Density Approximation
LSDA	Local Spin Density Approximation
NEB	Nudge Elastic Band
NMR	Nuclear Magnetic Resonance
PAW	Projector Augmented Wave
PBE	Perdew Burke Ernzerhof
PC	Pressure Cell
PDOS	Partial Density of States

PM	Paramagnet
QE	Quantum ESPRESSO code
RF	Radio Frequency
RKKY	Ruderman-Kittel-Kasuya-Yoshida
SC	Superconductor
SSCHA	Stochastic Self-Consistent Harmonic Approximation
TMMO	Transition Metal Mono-oxides
TRS	Time Reversal Symmetry
TRSB	Time Reversal Symmetry Breaking
UEP	Unperturbed Electrostatic Potential
VBM	Valence Band Maximum
μSR	Muon Spin Rotation and Relaxation spectroscopy

List of Symbols

$\hbar$	Normalized Planck's constant
μ^+	Positively charged muon
μ_B	Bohr Magneton
m_e	Mass of electron
m_μ	Mass of muon
M_p	Mass of muon proton

1

Introduction and motivation

In this thesis, I present the description of ab initio calculation approaches, in particular the density functional theory (DFT) method together with other theoretical approximations to determine the implantation site of the muon and its magnetic hyperfine coupling in a range of selected materials of current scientific interest. The results from these calculations allowed further understanding, interpretation and analysis of material properties observed from the experimental muon spin spectroscopy measurements.

Muon spin rotation, relaxation and resonance spectroscopy (μSR) is an experimental technique used for probing the properties of matter at the microscopic level, by exploiting the possibility of implanting highly spin polarized muons. μSR has been used to study a wide range of condensed matter systems and those considered in this thesis are a subset of superconducting, strongly electron correlated and magnetic materials, whose spin orbital correlations display interesting behaviour that shows up directly or indirectly, in the experimental muon decay anisotropy. The implanted muons thermalize in inorganic crystalline solids almost invariably at interstitial sites in the lattice and the magnetic local field that characterize the muon at this site(s) is recorded in the μSR data. However, the site of implantation together with different contributions/components to the local field at the muon are not known apriori from the experiment. In a number of cases, the rough accuracy in the estimation of the position where the muon stops in the sample, of the local perturbation introduced by the muon itself and of the Fermi-contact hyperfine coupling that enters the description of the muon-electron interactions, limit the number of information that can be extracted from the experimental data analysis. However, crucial material properties, especially the ground state magnetic moment in ordered materials and possibly the long range magnetic order as well, can only be determined in μSR by the knowledge of the muon implantation site and of the interaction constants between the muon and its atomic surrounding. The knowledge of both implantation site and contact hyperfine couplings contribution to the local coupling are essential for this information to be retrieved.

However, it is important to point out that there are a lot of material proper-

ties that can be accessed form μSR spectra without any prior knowledge of the muon site and the details of its coupling. With the muon local field both in superconductors and in magnetically ordered materials, the temperature dependence of the order parameter are measured, critical fluctuations are reflected in relaxation rates, the presence of additional phase transitions is easily detected, just to quote a few examples.

Various experimental approaches including the use of the measured precession frequency for magnetic materials, measurement of angular and field scans of the Knight shifts in single crystals, level crossing resonance method and paramagnetic shift measurements provide insights in the localization site and contact coupling of the muon. However, there are various limitations in the use of these approaches especially considering that they are not general in their application to all materials.

A different approach is to use computational methods to estimate these quantities with *ab inito* approaches. This is following significant advancement in electronic structure theory methods, especially the success of DFT in describing properties of materials and advent of High Performance Computing (HPC) that allows the implementation and use of these methods. This may in principle allow to unveil the full set of parameters governing the interaction between the implanted muon and its surroundings in the hosting compound provided that the description of the electronic and the nuclear degrees of freedom entering the theory is sufficiently accurate. *Ab initio* DFT has been successfully employed in the determination of the muon site. In this thesis, I continue to use the DFT method while describing the strategies within these methods that allow the determination of the muon site in a range of magnetic and superconducting materials. This approach also allows the investigation of the effect and perturbation induced by the implanted muon in the sample. Furthermore, with the *ab initio* DFT method, the approach for calculating and determining the Fermi contact hyperfine interaction of the muon in metallic systems was presented.

Further computational studies discussed include a new approach towards solving the zero point motion energy of the muon after its implantation in the host material. I have described a stochastic self-consistent harmonic approach that requires much less computational resources for describing the muon's zero point motion. This allowed to incorporate in our calculations involving the muon, the effect of the muon's zero point vibration.

1.1 Structure of the thesis

The structure and outline of the thesis include:

Chapter 2 - **Muon Spin Rotation Resonance and Relaxation Spectroscopy**: The μSR experimental technique relevant to understanding the research is described. Also, the magnetic coupling of the muon is described.

Chapter 3 - **Electronic structure theory**: The density functional theory including other electronic structure theory approximations used for calculations in this thesis are presented.

Chapter 4 - **Muon stopping sites in selected materials**: The calculation strategy and approach used for muon site determination are described. Furthermore, I present results of muon implantation site calculations together with those of μSR measurements in selected samples including $NaFe_{1-x}Ni_xAs$ an Fe based superconductor, $Yb_2Pd_2In_{1-x}Sn_x$ a heavy fermion compound and Sr_2RuO_4 a layered superconductor. Further analysis of sample properties by the combined μSR data and calculated muon sites is also presented.

Chapter 5 - **Muon contact hyperfine field in metals**: The effectiveness of a DFT-based approach in the calculation of the contact hyperfine field is presented. This is demonstrated on simple magnetic metals including Fe, Co, Ni, and further on chiral magnets of current high interest, MnSi and MnGe.

Chapter 6 - **Muon quantum motion effects and hyperfine fields in metals**: A stochastic self-consistent harmonic approximation for treating the zero point energy and motion of the muon is described. Further application of this method and effects of the muon zero point motion on the contact hyperfine field is described.

Chapter 7 - **Hydrogen defect states and muon hyperfine coupling in MnO and NiO**: The stability and effect of defect states in the band gap of the charged and neutral hydrogen defects in MnO and NiO is described. Further, analysis of the muon magnetic coupling and discussion on the magnetic moment alignment in these antiferromagnetically ordered samples are presented.

Chapter 8 - **Summary and Conclusion**

2

Muon spin relaxation, rotation and resonance spectroscopy

Muon spin relaxation, rotation and resonance spectroscopy (μSR) is an experimental technique that exploits the implantation of spin polarized muons to probe local properties of solid state materials, by means of the local magnetic field at the muon, together with its dynamics on the scale of the muon's mean lifetime (≈ 2.2 μs). Notably, this experimental technique makes predominant use of the positive antiparticles (μ^+). The basis of this technique lies in the anisotropic positron emission at the muon decay, peaked around the muon spin direction. The anisotropy is a hallmark of weak interactions in the three-body decay, and the very high muon spin polarization (almost 100%) relies on the same violation in the two-body pion decay that originates this probe particle. The evolution of the muon spin direction may be thus detected over several microseconds, with very fine time resolution, over an ensemble of individually implanted particles. Thus, the muon spin relaxation, rotation and resonance spectroscopy may be considered akin to Nuclear Magnetic Resonance (NMR), with the advantage of a broader applicability and a non resonant broadband detection. In analogy to NMR and ESR, the muon spin relaxation, rotation and resonance spectroscopy is represented by the acronym μSR, which generally represents studies involving interactions of the muon spin by asymmetric decay or the muon's magnetic moment and its use in the probe of materials. The foremost applications are in superconducting and magnetic materials, including very weak magnets, thanks to the good sensitivity provided by the large muon gyromagnetic ratio (≈ 135 MHz/T).

In this chapter, I will describe the important properties of the muon and the μSR experimental technique that are necessary to understand and follow the studies and results presented in this thesis. Other reviews on the the μSR technique can be found in Refs. [1–4] (to mention but a few).

2.1 The muon discovery and properties

The muon was discovered as one of the radiations from the cosmic rays in 1936 by Carl Anderson and Seth Neddermeyer [5]. Over the years, the properties of the muon and its mystery has been dissipated. The muon has mass of 105.7 MeV/c^2 which is almost 9 times less than that of a proton and 200 times that of an electron. Just like the electron, the muon is a charged spin 1/2 particle. However, unlike the electrons and other elementary particle, the muon has a mean lifetime of ≈ 2.2 μs and decays spontaneously to a positron (e^+), an electron neutrino (ν_e) and a muon anti-neutrino ($\overline{\nu}_\mu$) pair for a positively charged muon (μ^+), and for the negatively charged muon (μ^-), it decays to an electron, a neutrino and anti-neutrino pair. The three body decay is represented below:

$$\begin{aligned} \mu^+ &\rightarrow e^+ + \nu_e + \overline{\nu}_\mu \\ \mu^- &\rightarrow e^- + \overline{\nu}_e + \nu_\mu \end{aligned} \tag{2.1}$$

The decay process of the positive charged muon and the anisotropic emission of the positron, peaked around the muon spin direction forms the basis of its application in μSR. Also, the positive muon used for probe in μSR is likened to a light proton. However, the muon has a magnetic moment 3.18 times larger than that of a proton. This property of the muon makes it an extremely sensitive microscopic probe of magnetism. The muon gyromagnetic ratio is $(\frac{\gamma_\mu}{2\pi}) \approx 135.538$ MHz T^{-1}.

2.2 The muon production

The use of muon as a probe for matter started flourishing, following the parity violation laws in weak interaction by Chen Ning Yang and Tsung-Dao (T.D.) Lee [6] and the experimental discovery by Richard Garwin *et.al* [7] together with other experiments showing decay of pions to muons and then muons to electrons and pair neutrinos.

Muons are naturally created by proton-proton interactions when cosmic rays hit the atmosphere and by particle accelerators involving high-energy decays and particle decay in the laboratories. For the purpose of μSR, low energy muons capable of stopping in the samples are required. These low energy muons originate from the two-body pion decay. Thus, a pion has to be made first. The production of pions are from collisions of high-energy protons (above 500 MeV) with the carbon targets or other light elements which allows minimizing the scattering of the beam of protons and maximizing pion production. The charged pions (π^+ or π^-) are short lived for 26.033 nanoseconds and spontaneously decay to a charged

muon and the muon neutrino (or anti-neutrino). The pion decay is represented below as:

$$\begin{aligned} \pi^+ &\rightarrow \mu^+ + \nu_\mu \\ \pi^- &\rightarrow \mu^- + \overline{\nu}_\mu \end{aligned} \tag{2.2}$$

In μSR facilities, the kinetic energy and type of charged muon (negative or positive) produced depend on the pion process. For the so called *surface muon*, the muon is emitted isotropically with a kinetic energy of 4.119 MeV and momentum of 29.8 MeV/c from a pion that decays at rest on the surface of the target. Only the positive muon can be produced by this approach because a negatively charged pion stopping at the production target will always be captured by a nucleus from the low lying orbitals of pionic atoms even before it decays. In order to overcome this phenomenon,the so called *backward muon* approach is used. Both the negatively and positively charged muon can be produced by this approach. It involves allowing the decay of the pions *in flight* within a long superconducting solenoid, while the muons are emitted opposite to the direction of the pion momentum. The *decay muon* has a higher momentum than the former in the range of 50-100 MeV/c, this increases the stopping density of the muon in the sample. Also, the *decay muon* has a much larger phase space than the *surface muon* and this lowers the luminosity. However, even though these two features of the *decay muon* are less enticing, they still remain the means of allowing muon implantation and μSR studies of samples that are enclosed in thick vessels like the pressure cells for high-pressure studies and for gas and liquids contained in a vessel.

However, in μSR experiments the positive muons (μ^+) are mostly used and preferred since because of their positive charge they avoid the host nuclei in the sample while the negatively charged muon (μ^-) can mostly be captured in the nucleus. Also a significant amount of the spin polarization of μ^- is lost during the capture process, thus introducing a lot of signal noise in the time evolution. For the purpose of this study, the experimental results are of μSR utilizing the positive muon μ^+, which sometimes bear the acronym μ^+SR.

2.2.1 The muon beam

There are few proton accelerators with intense muon beam facilities in the world, they include:

- The Tri-University Meson Facility (TRIUMF) in Canada,
- The Paul Scherrer Institute (PSI) in Switzerland,

- ISIS at the Rutherford Appleton Laboratory (RAL) in the United Kingdom, and the Japanese Institute of Physical and Chemical Research (RIKEN) at the ISIS facility.
- The MUSE (Muon Science Establishment) at the Japan Proton Accelerator Research Complex (J-PARC).

The muon beams used for μSR experiments at these facilities are said to be *continuous* or *pulsed* depending on the time structure of the proton source.

- The **continuous** beam facilities have a nearly continuous proton source that produces muons arriving at the experimental stations and thus the sample. This muon beam allows better time resolution ($\approx$ 100 ps) of μSR instruments. With better time resolution, fast relaxing signals and stronger magnetic fields are detected. The muon beam at PSI and TRIUMF facilities are the *continuous* type.
- The **pulsed** muon beams are so named because the protons from the source directly arrive to the production target in bunched beams. Hence, the pulsed structure and timing of the muon beams reflect that of the proton that is smeared out by the pion lifetime. The time width of the pulses are on the order of tens-of-nanoseconds and thus must be shorter than the muon lifetime, so that the pulse repetition time must be longer than the muon lifetime. These conditions limits the time resolution. With the pulsed beam almost all the incoming muons are used and there are almost no background signal from accidental coincidence of the muon and positron. The advantages of pulsed muon sources include; measuring slowly relaxing signals and weak magnetic fields. The muon beam at J-PARC and ISIS facilities are of the *pulsed* type.
- **Beams of low energy muons** have been developed to satisfy the increasing desire to investigate surfaces, thin films and multi-layered interfaces with muons unlike the conventional surface muons that are used for study of small samples. The low energy muons are transported with mean energy of about 15 keV with approximately 0.5keV minimum energy of implantation. These low energy muons are capable of stopping at depths in the order of fractions of nanometer to a few hundred of nanometers. The low energy muons are produced by moderation in thin condensed gas targets. A major set back for the low energy muon is that the intensity is reduced compared to the incident surface muon beams.

2.3 Asymmetry parameter and μSR

The fundamental unique properties of the pion and muon decay that allows the use of the μSR technique in probing condensed matter systems include:

- The emitted muon from the pion decay at rest arrives almost 100 percent spin polarized to the sample. This is made possible by the maximal parity violation of the pion weak interaction decay. This particular property provides a considerable advantage in comparison to other magnetic probe methods like NMR and ESR methods where the required polarization is achieved by applying strong magnetic field or at very low temperatures.

- Also, following the parity violation process in the weak decay, the muon decays to a positron preferentially along its spin direction. Thus for muons implanted under the same conditions, the average muon spin direction can be determined by measuring the *time dependent distribution* of the decay positrons. The anisotropic probability of positron emission, maximum at the muon spin direction, follows the evolution of the spin in time, and it can be measured averaging over the fate of many muons, each starting with the same initial spin direction.

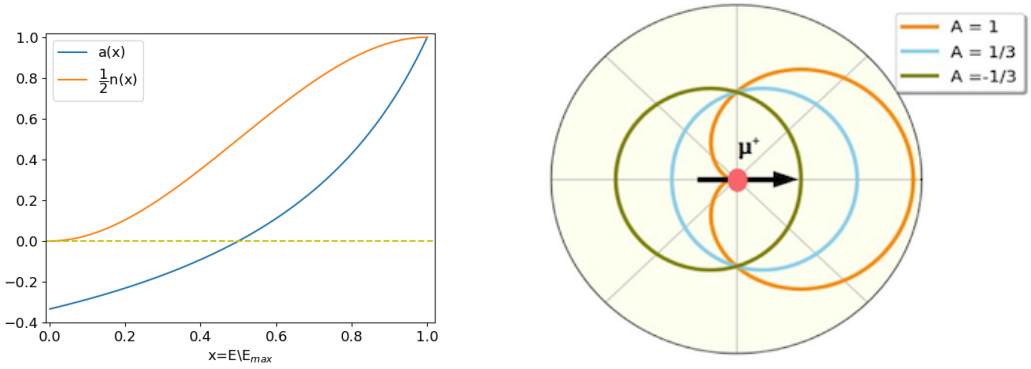

(a) Asymmetry function plot

(b) Polar diagram

Figure 2.1: (a) plot of the symmetry function $a(x)$ and emission number $n(x)$ (b) Polar Diagram of the angular distribution of the positron $P(\theta)$ from decay of positively charged muons, μ^+. Orange, green and light blue represent the anisotropy function Eq. 2.3, for a positron of maximum, minimum energy, and for the average over all energies, respectively.

The distribution function for the positron emission depending on energy and angle is defined as:

$$\frac{dW(x,\theta)}{dxd\Omega} = \frac{n(x)}{4\pi}(1 + a(x)cos\theta) \tag{2.3}$$

In the equation above, $x = E/E_{max}$, where E represents positron energy, $E_{max} = 52.8MeV$, θ is the angle between the positron trajectory and the μ^+ spin, $a(x)$ is an asymmetry function of positron energies while $n(x)$ is an emission number. Functions defining a(x) and n(x) are shown in Fig. 2.1a and defined as:

$$a(x) = \frac{2x-1}{3-2x}$$
$$n(x) = 2x^2(3-2x)$$

With the positron energies in Eq. 2.3, the probability distribution of the positron emission which is correlated to the direction of the muon spin is given as:

$$P(\theta) \propto (1 + A_0 \cos\theta) \tag{2.4}$$

where A_0 corresponds to the average over all positron energies (light blue shape in Fig. 2.1b) and is written as;

$$A_0 \equiv \langle a(x) \rangle = \int_0^1 a(x)n(x)dx = \frac{1}{3} \tag{2.5}$$

This value is reduced by experimental efficiency, and further averaging over large solid angles typically to values in the range of 0.2-0.27.

2.4 μSR experimental technique

In μSR experiment, deceleration occurs when muons are implanted in the sample, during which their energy is quickly lost in a time frame of approximately 100 ps, shorter than a typical μSR histogram bin. The muons thermalize while slowing down towards an implantation site without any appreciable loss of their spin polarization. The principle that allows the use of muons for probing materials is not lost. This is also because all the processes that occur during the thermalization are Coulombic.

The implanted muons normally stop at interstitial sites especially for inorganic samples. Also, depending on the nature and depth of the potential at the muon site, the muon can be trapped at the site or diffuse locally between interstitial sites. At high temperature muons may hop rapidly among equivalent sites over larger distances. For metallic samples the charge of the positive muon is screened by the

conduction electrons, that the muon is in a state experimentally indistinguishable from a diamagnetic muon. However, in insulators and semiconductors, the muon can pick up an electron to be in the paramagnetic state forming the muonium (μ^+e-) or can still remain in the diamagnetic state.[8]

2.4.1 Experimental setup

In μSR technique, depending on the properties and phenomena one would want to investigate, there are a number of experimental setups to choose characterized by the absence or presence of an external magnetic field and by its alignment with respect to the initial muon spin direction. One distinguishes:

- **Zero Field Muon Spin Relaxation (ZF-μSR)**: ZF-μSR involves the study of the muon spin time evolution only upon the influence of the internal magnetic field, here an external magnetic field is not applied. For magnetically ordered phases, the approach is mostly used to measure the muon precession frequency, giving direct information on the temperature dependence of the order parameter and indirectly also on the magnetic structure and static magnetic moments. ZF-μSR is very sensitive for detecting weak magnetism and can detect very low static moments, giving μSR an advantage over other experimental techniques, notably neutron diffraction.

- **Longitudinal Field Muon Spin Relaxation (LF-μSR)**: In LF-μSR, the external magnetic field is applied parallel to the initial muon spin polarization direction (see Fig. 2.2a). Like ZF-μSR, the time evolution of the muon polarization is measured along its original direction. It is used to study the origin of depolarization by applying external field stronger than the internal field, such that the static inhomogenous distribution of the internal fields (if present) will not affect the time evolution of the muon polarization.

- **Transverse Field Muon Spin Rotation (TF-μSR)**: In experiments involving this technique, an external magnetic field is applied perpendicular to the initial muon spin polarization direction (see Fig. 2.2b). The muon spin precesses in a plane perpendicular to the external magnetic field with a frequency proportional to the size of the total field at the muon implantation site. TF-μSR allows the measurement of the magnetic field distribution of the vortex lattice in a type II superconductor since generally, it allows to study the inhomogeneities of the local field distribution at the muon interstitial site, due to the formation of an Abrikosov flux lattice, from the transverse dephasing of the muon precession and the corresponding depolarization. Also with this experimental setup, the μ^+ Knight shift in systems

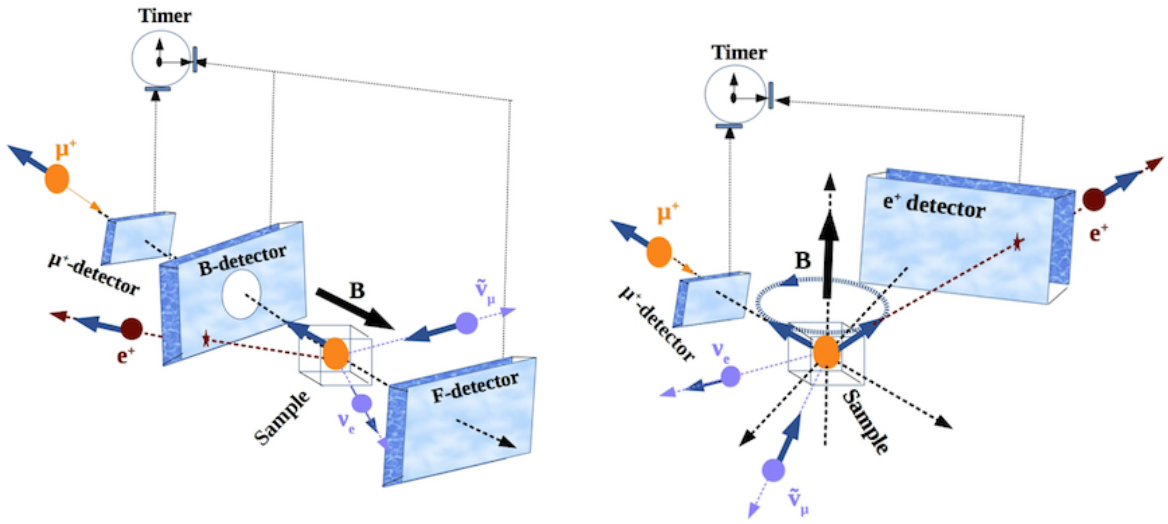

(a) LF-μSR **(b)** TF-μSR

Figure 2.2: Schematic diagram of a) LF-μSR and b) TF-μSR technique

can be retrieved, it provides relevant information on the hyperfine fields and thus the local susceptibility (see Sec. 2.5).

- Other types of μSR experiments include; **(Avoided) Level Crossing Resonance (μALCR and μLCR)** and **Muon Spin Echo (μSE)**. In μSR, resonance studies are normally performed when a radio-frequency (rf) pulse is used to reorient the muon spin from the initial muon spin polarization, such that resonance occurs when the rf matches an energy splitting of one of the muon states in the sample. In μALCR and μLCR techniques, the resonance are observed as a '*dip*' in the evolution of the muon polarization as the applied magnetic field is varied, typically in the range of (1-3 T) for molecules. They are used for various purposes which include; measuring the muon hyperfine coupling constants in radical structures [9], investigation of spin dynamics [10] and determination of muon implantation site in semiconductors [11, 12]. In μSE, a muon spin echo appears in the time evolution of the muon polarization as a timed rf is applied after the muon comes to rest in the sample. μSE technique is mostly used to determine the different contributions of the dynamic and static local field to μSR experiment.

2.4.2 Count rates

In a typical μSR experimental setup (see Fig. 2.2), the polarized muon beam enters from the left, and a muon detector provides the start signal for a clock. The muon then penetrates the sample and comes to rest at an interstitial site. Its spin then precesses around the local field $\mathbf{B}$ at the Larmor frequency ω_μ. The frequency is given by $\omega_\mu = \gamma_\mu \mathbf{B}$, where $\gamma_\mu/2\pi = 135.538$ MHz/T, is the gyromagnetic ratio for the muon.

If the positron from the muon decay hits a detector in a given direction, the signal thus generated will stop the clock, measuring the muon lifetime. An event will be added to a histogram at the corresponding time bin. This produces average count rates versus time for the chosen direction.

Assuming two directions, forward (F) and backward (B) with respect to the initial muon spin, the count rates N(t) have the form:

$$N(t) = N_0 e^{-t/\tau_\mu}[1 + A_0 \mathbf{P}(t) \cdot \hat{n}] + B_0 \tag{2.6}$$

where N_0 is the initial count rate, A_0 is asymmetry, τ_μ is the average muon life time and B_0 is a time independent background

$\mathbf{P}(t) \cdot \hat{n}$ is defined as the projection of $\mathbf{P}$(t) along the initial direction polarization, $\hat{n}$. The rate of change of $\mathbf{P}$ is given as;

$$\frac{d\mathbf{P}}{dt} = \gamma_\mu(\mathbf{P} \times \mathbf{B}(t)) \tag{2.7}$$

where $\mathbf{B}(t)$ is the total field at the muon site (i.e including applied field) and $\mathbf{P} = \frac{<\mathbf{S}>}{1/2\hbar}$ with $\mathbf{S}$ the muon spin operator.

At the muon site, when the muon feels a perpendicular internal or applied magnetic field, the polarization due to the spin precession around the field is given by: $\cos(\gamma_\mu |\mathbf{B}_\mu| t + \theta)$, where θ represents the initial phase the muon makes with respect to the detector.

The time evolution of the number of positrons detected after the muon decay on the forward and backward detectors $N_F(t)$ and $N_B(t)$ are shown in Figs. 2.3a and 2.3b for a longitudinal and transverse applied magnetic field. The relations that describe the counts are given by:

$$N_F(t) = N_0 e^{-t/\tau_\mu}[1 + A_0 \mathbf{P}(t).\hat{n}] \tag{2.8}$$

$$N_B(t) = N_0 e^{-t/\tau_\mu}[1 - A_0 \mathbf{P}(t).\hat{n}] \tag{2.9}$$

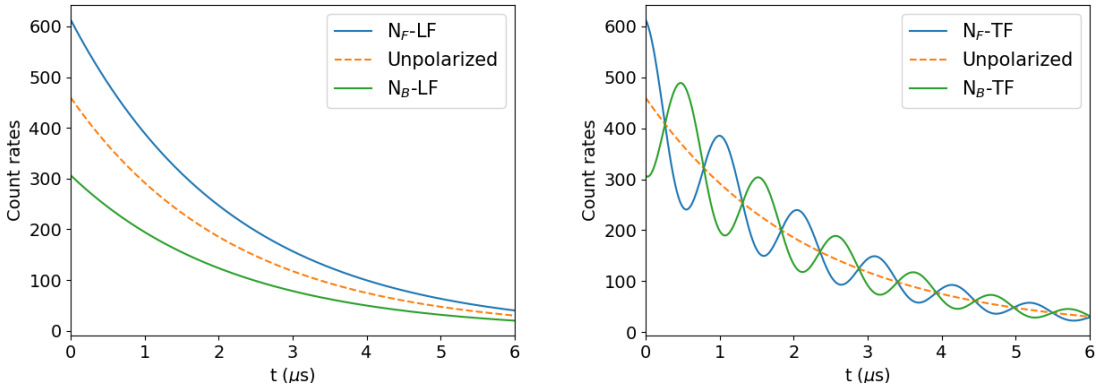

(a) For LF **(b)** For TF

Figure 2.3: Count rates and asymmetry plots for fields applied longitiduanlly (LF) and transversely (TF) to muon spin polarization direction and ideal asymmetry-polarization evolution plots.

The normalized difference of these functions, after fitting and subtracting the background B_0 gives the the asymmetry function $A(t) \equiv A_0\mathbf{P}(t).\hat{n}$ and given as:

$$A(t) = \frac{N_F(t) - N_B(t)}{N_F(t) + N_B(t)} \tag{2.10}$$

$A(t)$ describes the time evolution of the muon polarization, thus containing crucial information of the static and dynamical fluctuations of the muon spins as functions of temperature, pressure and applied magnetic field.

The asymmetry function evolution with time can be normalized with A_0 to one and this gives the muon spin autocorrelation function, $G(t) = A(t)/A_0$. This represents the time dependent spin polarization of the muon. In μSR experiment, from the resulting signal, the asymmetry parameter and spin polarization evolution are extracted from a ZF, LF and TF data.

2.4.3 μSR Precession and relaxation functions

In order to describe the different forms of the spin autocorrelation function $G(t)$ and if the muon is capable of detecting and studying the internal magnetic field, we revisit the muon precession process (see Fig. 2.4). If the direction of the initial muon spin polarization is along $\hat{\mathbf{z}}$ and the local magnetic field, B_μ makes an angle θ with $\hat{\mathbf{z}}$, the muon spin will precess around B_μ as shown in Fig. 2.4 with the precession frequency $\omega_\mu = \gamma_\mu |B_\mu|$.

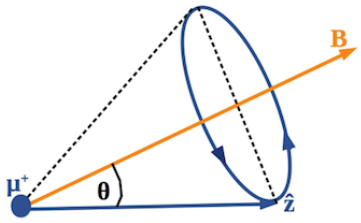

Figure 2.4: Muon spin precession around a local magnetic field B_μ at an angle θ between the initial muon spin polarization direction $\hat{\mathbf{z}}$ and B_μ.

From Fig. 2.4, the muon spin polarization evolves in time as:

$$G(t) = cos^2\theta + sin^2\theta cos(\gamma_\mu |B_\mu| t) \tag{2.11}$$

Such that, for randomly oriented magnetic field with well defined modulus, for example in polycrystalline sample, averaging the internal magnetic field over all directions will yield:

$$G(t) = \frac{1}{3} + \frac{2}{3} cos(\omega_\mu t) \tag{2.12}$$

Let us now consider a static muon probing a distribution of static random field such as those due to nuclear dipole moments in a lattice. The randomly oriented nuclear dipolar fields will be seen as static in μSR (see refs [1, 2] and references therein). The spin autocorrelation function along z will be the average over the distribution, approximated as a Gaussian of width $\frac{\Delta}{\gamma_\mu}$ for each component x,y,z of the random nuclear field. The function can be written in the form:

$$G(t) = \frac{1}{3} + \frac{2}{3} e^{-\Delta^2 t^2/2}(1 - \Delta^2 t^2) \tag{2.13}$$

The form of the function (Eq. 2.13) is equivalent to an over-damped oscillation of amplitude 2/3 at the frequency Δ, (since $1 - \Delta^2 t^2 \approx \cos(\Delta t)$ at short times) including a 1/3 constant. They represent respectively over-damped precessions around two transverse components, x,y of the local fields and a stationary state for the third longitudinal z components. This function was first derived theoretically by Kubo and Toyabe in 1966 [13], hence it is known as the Kubo-Toyabe relaxation function. Fig. 2.5 shows the plot of the Kubo Toyabe function. The second moment of the Gaussian distribution can be represented by $\frac{\Delta^2}{\gamma^2}$.

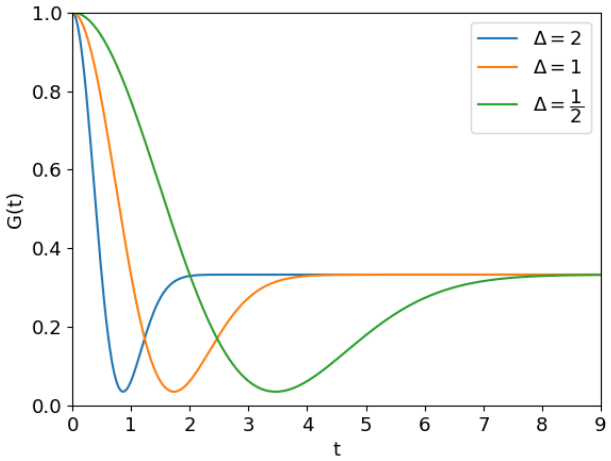

Figure 2.5: Kubo Toyabe relaxation function for different values of Δ

However, if the distribution of each component of the random local field is Lorentzian (as in the case of a diluted nuclear spin on a lattice), then the function is of the form:

$$G(t) = \frac{1}{3} + \frac{2}{3}e^{-at}(1 - at) \tag{2.14}$$

where $\frac{a}{\gamma_\mu}$ represents the half-width at half maximum of the Lorentzian function.

For cases where there is a rapid diffusion of the muon from one interstitial site to another and also for cases of rapid spin fluctuations, such that there are fast fluctuations with fluctuation time τ, the depolarization function at initial times will relax in this form:

$$G(t) = e^{-2\Delta^2\tau t} \tag{2.15}$$

The origin of the depolarization in Eq. 2.15 can be investigated by using the longitudinal field LF technique, since by using a parallel (to the initial spin polarization) applied field H_{ext} stronger than the internal field, the muon spin is decoupled from the internal fields and thus not depolarized by an inhomogeneous internal field even at longer times in the evolution.

TF relaxation functions: As already mentioned, in an applied transverse field B_{ext} in the absence of relaxation, the muon's precessing asymmetry function is a cosine function. However, for real samples the muon precession is modulated by a relaxation function, G(t) depending on the distribution induced by the local field B_0 in the sample, where the precessing asymmetry is given as:

$$A(t) = A_0 \cos(\gamma_\mu B_{ext} t) G(t) \tag{2.16}$$

where A_0 is the initial asymmetry. If the distribution is Gaussian, the precessing asymmetry will have the form;

$$A(t) = A_0 \cos(\gamma_\mu B_{ext} t) e^{-\Delta^2 t^2/2} \tag{2.17}$$

In TF experiments, the relaxation function has a non trivial form if $B_{ext} << B_0$. However for large $B_{ext} >> \Delta/\gamma_\mu$ the relaxation function is independent of the applied transverse field but on those of the internal fields [14].

2.5 Muon magnetic coupling Hamiltonian

Implanted muons almost invariably thermalize in inorganic crystalline solids at interstitial sites in the lattice, so that the detected internal field is that at an interstitial of an extremely diluted impurity. The experimental value of the muon local field, including both its static value and its fluctuating dynamical components, provides important clues towards understanding the magnetic properties of the host material.

Following the description for a generic nucleus described in Ref [15] and already extended for the muon in Ref [4]. The muon has spin 1/2 and couples to a magnetic field. The muon magnetic moment is defined as $\boldsymbol{\mu}_i^\mu = -g_\mu \mu_B \mathbf{S}_i^\mu$ where g_μ is the muon spin g-factor, $\mathbf{S}^\mu$ is the muon spin operator and μ_B is the Bohr magneton.

Within a non relativistic quantum mechanical description, the Hamiltonian H of an electron coupled to the muon in the presence of a magnetic vector potential $\mathbf{A}$ produced at the muon by the magnetic moment $\boldsymbol{\mu}^\mu$ that is far from the muon by a radius vector $\mathbf{r}$, is given as;

$$H = \frac{1}{2m_e}(\mathbf{p} + e\mathbf{A})^2 + g_e \mu_B \mathbf{S}^e \cdot \nabla \times \mathbf{A} \tag{2.18}$$

where m_e is the electron mass, $\mathbf{p}$ the momentum operator, e the positive unit charge, g_e the electron spin g-factor and $\mathbf{S}^e$ the electron spin operator.

The magnetic vector potential is given as;

$$\mathbf{A} = \frac{\mu_0}{4\pi} \frac{\boldsymbol{\mu}^\mu \times \mathbf{r}}{r^3} = \frac{\mu_0}{4\pi} \left(\nabla \times \left(\frac{\boldsymbol{\mu}^\mu}{r} \right) \right) \tag{2.19}$$

where μ_0 is the vacuum permeability.

If one considers only to the first order while neglecting the higher order terms in Eq. 2.18 using perturbation theory including neglecting the kinetic energy of the electrons since the interest is on the muon coupling, then Eq. 2.18 becomes;

$$H = \frac{e}{2m_e}(\mathbf{p} \cdot \mathbf{A} + \mathbf{A} \cdot \mathbf{p}) + g_e \mu_B \mathbf{S}^e \cdot \nabla \times \mathbf{A} \tag{2.20}$$

Substituting equation Eq. 2.19 in Eq. 2.20 and considering that the electron orbital momentum operator is $\hbar\mathbf{L} = \mathbf{r} \times \mathbf{p}$,[1] then the Hamiltonian in Eq. 2.20 can be written as;

$$H = \frac{\mu_0 \mu_B}{4\pi} \left(\frac{2\mathbf{L} \cdot \boldsymbol{\mu}^{\mu}}{r^3} + g_e \mathbf{S}^e \cdot \nabla \times \left(\nabla \times \frac{\boldsymbol{\mu}^{\mu}}{r} \right) \right) \tag{2.21}$$

Further using the relation $\nabla \times (\nabla \times A) = \nabla(\nabla \cdot \mathbf{A}) - \nabla^2 \mathbf{A}$ where ∇^2 is the Laplacian, Eq. 2.21 becomes

$$\begin{aligned} H = \frac{\mu_0 \mu_B}{4\pi} \Bigg(& \frac{2\mathbf{L} \cdot \boldsymbol{\mu}^{\mu}}{r^3} + g_e \left[(\mathbf{S}^e \cdot \nabla)(\boldsymbol{\mu}^{\mu} \cdot \nabla) - \frac{1}{3}(\mathbf{S}^e \cdot \boldsymbol{\mu}^{\mu}) \nabla^2 \right] \frac{1}{|r|} - \\ & \frac{2}{3} g_e (\mathbf{S}^e \cdot \boldsymbol{\mu}^{\mu}) \nabla^2 \frac{1}{|r|} \Bigg) \end{aligned} \tag{2.22}$$

The above Hamiltonian contains the various contributions in the coupling of the electron to the muon. In order to recognize the physical meaning of the right hand side terms we need to consider that;

- In magnetic materials, the muon is coupled e.g. to the (mean) field of more than one electron.
- Since the interest is on the muon coupling to the electrons, the muon Hamiltonian is gotten by multiplying the total Hamiltonian H with the electron density $\psi_e^* \psi_e$ and integrating over the electron coordinates as;

$$H_{\mu} = \langle H \rangle = \int d\mathbf{r} \psi_e^* H \psi_e \tag{2.23}$$

If one considers in the integration, the case for r different from zero ($r \neq 0$), i.e when there is a negligible probability for the electron to be at the muon site. Here, the first term in Eq. 2.22 gives a vanishing contribution considering that the electrons do not orbit around the interstitial implanted muon site but around the lattice sites. The third (last) term also gives a vanishing contribution considering the Laplacian while the second term results in the dipolar contribution, same as that of a dipole interaction from classical electromagnetism and is given as;

$$H_{dip} = -\frac{\mu_0}{4\pi} \sum_i \left[\frac{3(\boldsymbol{\mu}^{\mu} \cdot \mathbf{r}_i) \cdot (\boldsymbol{\mu}_i^e \cdot \mathbf{r}_i)}{r_i^5} - \frac{\boldsymbol{\mu}_i^e \cdot \boldsymbol{\mu}^{\mu}}{r_i^3} \right] \tag{2.24}$$

[1] It is important to remember that; $\mathbf{r} \times \mathbf{p} = -\mathbf{p} \times \mathbf{r}$ and $(\boldsymbol{\mu}^{\mu} \times \mathbf{r}) \cdot \mathbf{p} = \boldsymbol{\mu}^{\mu} \cdot (\mathbf{r} \times \mathbf{p})$ together with $\mathbf{p} \cdot (\boldsymbol{\mu}^{\mu} \times \mathbf{r}) = \mathbf{r} \cdot \mathbf{p} \times \boldsymbol{\mu}^{\mu}$

where $\boldsymbol{\mu}_i^e$ is the spin moment operator of the ith electron, given as $\boldsymbol{\mu}_i^e = -g_e\mu_B\mathbf{S}_i^e$ while $-g_e\mu_B = \gamma_e\hbar$ with γ_e being the electron gyromagnetic ratio. Here the moment is due to the spin only angular momentum which holds typically for 3d electrons where angular momentum is *quenched* in the crystal field. In cases, where there are strong spin-orbit coupled interaction especially for the 4f and 5f localized electrons, such that the spin and orbital contribution are not disentangled, the spin moment operator $\mathbf{S}_i^e$ is replaced by the total angular momentum operator $\mathbf{J}_i^e$ given as $\mathbf{J}_i^e = \mathbf{L}_i^e + \mathbf{S}_i^e$.

For r$\rightarrow$0, i.e when there is a finite electron density probability to be at the muon. If the wave function ψ_e is expanded as a sum of spherical harmonics ($\sum_{l,m} a_{l,m}Y_l^m$) around the muon site, only the $l = 0$ term yields a finite contribution, since for all $l > 0$ the wavefunction behaves as r^{-l} in the vicinity of the muon. Hence if the muon is surrounded by a spherically symmetric cloud of electrons, only the third term in Eq 2.22 gives a finite contribution and is given as:

$$H_c = -\frac{2\mu_0}{3}\sum_i (\boldsymbol{\mu}_i^e \cdot \boldsymbol{\mu}^\mu)\delta(\mathbf{r}_i) \tag{2.25}$$

such that after integration Eq. 2.25 becomes:

$$H_c = -\frac{2\mu_0}{3}\left|\psi^e(\mathbf{r})\right|^2 (\boldsymbol{\mu}^e \cdot \boldsymbol{\mu}^\mu) \tag{2.26}$$

This term exists only for a partial s-electron around the muon and is called Fermi contact interaction.

Summarizing, two contributions have been identified in the muon-electron magnetic coupling, which are: the dipole term and the contact term. We have neglected so far a possible additional contribution of $l > 0$ spherical harmonics through the dipole term. This gives rise to the so-called pseudo-dipolar term, a rank 2 constant tensor coupling that adds to the scalar contact term. This term often vanishes and I will ignore it henceforth.

The magnetic coupling of the muon to its environment can be described by an effective Zeeman Hamiltonian H_Z, considering that from Eqs. 2.21, 2.24 and 2.25, H, H_{dip} and H_c are linear in $\boldsymbol{\mu}^\mu$. Hence;

$$H_Z = -\boldsymbol{\mu}^\mu \cdot \mathbf{B}_\mu \tag{2.27}$$

where $\mathbf{B}_\mu$ is the local field at the muon consisting of the dipolar and Fermi contact contribution.The local field at the muon undergoes fluctuations due to electron and lattice dynamics, and can be written as;

$$\mathbf{B}_\mu = \langle \mathbf{B}_\mu \rangle + \delta\mathbf{B}_\mu \tag{2.28}$$

where the first term which generally is non-null in an ordered magnetic state while the second is the fluctuation term and drives the muon spin relaxation.

Summarily, in the absence of external magnetic field and considering the muon magnetic Hamiltonian coupling in Eq. 2.22 and the Zeeman interaction in Eq. 2.27. The contribution to the local field at the muon is given by;

$$\mathbf{B}_\mu = \mathbf{B}_{dip} + \mathbf{B}_c \tag{2.29}$$

where the dipolar $\mathbf{B}_{dip}$ contribution is given as;

$$\mathbf{B}_{dip} = \frac{\mu_0}{4\pi} \sum_{i=1}^{N} \left[\frac{3\mathbf{r}_i(\boldsymbol{\mu}_i \cdot \mathbf{r}_i)}{r_i^5} - \frac{\boldsymbol{\mu}_i}{r_i^3} \right] \tag{2.30}$$

with $\boldsymbol{\mu}_i$ as the magnetic moment of the ith atom in units of μ_B, r_i constitute the distance between the ith atom and the muon site, while N is the total number of magnetic moments.

The Fermi contact contribution ($\mathbf{B}_c$) is effectively given by;

$$\mathbf{B}_c = \frac{2\mu_0}{3} \left|\psi^e(\mathbf{r}_\mu)\right|^2 \eta(\mathbf{r}_\mu)\boldsymbol{\mu}^e \tag{2.31}$$

where $\eta(\mathbf{r}_\mu)$ is the so called enhancement factor describing the muon perturbation on its immediate surrounding and effects on the lattice, an issue I shall address by DFT in the next chapters.

2.5.1 Calculation of $\mathbf{B}_c$

Unlike the dipolar contribution that can be retrieved by classical methods, the contact interaction contribution requires an accurate quantum mechanical treatment which still presents challenging aspects for ab-initio simulations in magnetic materials. I address the electronic structure theory approach that allowed for accurate calculation of this contribution in chapter 5. In this chapter, the correct estimation of the imbalance in spin density distribution at the muon site is optimized particularly for metallic systems. In this approach, the muon is introduced as an impurity in the lattice at the site of implantation, such that the perturbation due to the muon is captured in the self-consistent evolution of the electronic distribution and wavefunction. The true behaviour of the muon distortion on the lattice and electric gradient is captured in the electronic wavefuntion, ψ_e, such that the enhancement factor $\eta(\mathbf{r}_\mu)$ already enters in it and considering the collinear spin approximation, $\mathbf{B}_c$ can then be rewritten as;

$$\mathbf{B}_c = \frac{2\mu_0\mu_B}{3}\rho_s(\mathbf{r}_\mu) \tag{2.32}$$

where $\rho_s = [\rho_s^{\uparrow} - \rho_s^{\downarrow}]$ is the spin density at the muon position $\mathbf{r}_\mu$, $\rho^{\uparrow}$ and $\rho^{\downarrow}$ are the density associated to each spinor component with $\rho_s^{\sigma} = |\psi^{\sigma}|^2$.

The localized electronic contribution vanishes for s and p electrons and only $\mathbf{B}_c$ contributes besides the small contribution of the nuclear moment. However, for d and f electrons, asides the dipolar contributions, there are the second order processes which includes: indirect RKKY interactions for metals and transferred interactions in insulators. The transferred interactions in insulators is from the overlap of the host localized magnetic wavefunction and the muon wavefunction. [1, 4] These second-order magnetic interactions are short ranged and are directly captured with the electronic structure method used for calculating the Fermi-contact contribution in this work.

2.5.2 Summation of $\mathbf{B}_{dip}$ in direct space

The dipolar tensor is rather easy to estimate with sufficient accuracy using a classical dipole approximation. The muon dipolar coupling results from interaction between the muon moments and dipole moment of the host atoms. For the evaluation of the dipolar fields and summation of the long range dipoles in real space, a Lorentz sphere construction approach is usually improvised such that within the sphere a lattice sum as depicted in Eq. 2.30 gives the dipolar field while the summation outside the sphere leads to the Lorentz term.The Lorentz field $\mathbf{B}_L$ arises from the calculation of the averaged dipole at the μ^+ stopping site by separating the dipoles into near and far with an imaginary sphere around the muon [4, 16, 17].[2]

Furthermore, there is the demagnetization term that accounts for the dipoles that exist on the surface of the sample. Both the demagnetization and Lorentz terms sum up to null in systems with antiferromagnetic ordering.

In LF and TF experiments, an external field $\mathbf{H}_{ext}$ is also present. This is typically the case for investigations in the paramagnetic phase of a magnetic material, where a non-vanishing expectation value of the electron magnetic moment appears, at each site i

$$\langle \mathbf{S}_i^e \rangle = \chi_i \mathbf{H}_{ext} \tag{2.33}$$

where χ_i may in principle depend on the point symmetry of the $i-th$ moment, with the macroscopic χ given by $\chi = \sum_i \chi_i$ restricted to the magnetic unit cell.

Notice that the spin of Eq. 2.33 does not obey the low temperature spin structure (it has ferromagnetic q=0 symmetry). It yields a dipolar field $\mathbf{B}_{dip'}$ by sub-

[2]Dipolar simulations reported in this thesis were carried out by the implementation in the python codeMUESR

stitution into Eq. 2.30, and with the Lorentz sphere approach, the dipolar field at the muon implantation site has the following contribution;

$$\mathbf{B}_{dip} = \mathbf{B}_{dip'} + \mathbf{B}_L + \mathbf{B}_{dem} \tag{2.34}$$

where $\mathbf{B}_{dip'}$ is the dipolar field sums of Eq. 2.30, calculated within the sphere, $\mathbf{B}_L$ and $\mathbf{B}_{dem}$ are the Lorentz and demagnetization field respectively.

The demagnetization fields are due to dipoles on the sample surface and as such they depend on the bulk magnetization $\mathbf{M}_b$ and the shape of the sample. This is given as;

$$\mathbf{B}_{dem} = \overline{\mathbf{N}} \cdot \mathbf{M}_b \tag{2.35}$$

where $\overline{\mathbf{N}}$ is the demagnetization tensor.

$\mathbf{B}_{dem}$ is uniform inside the sample only for an ellipsoid where there exist uniform demagnetization and $\overline{\mathbf{N}}$ can be calculated with trace of the diagonal of the tensor equal to 1. The simple cases of shape and field direction dependent factor referred to as the demagnetization coefficient for each sample shape is given as :

- for sphere = $\frac{4\pi}{3}$
- for $\mathbf{H}_{ext}$ applied parallel to a cylinder = 0
- for $\mathbf{H}_{ext}$ applied perpendicular to a cylinder = 2π
- for $\mathbf{H}_{ext}$ applied perpendicular to a thin plate = 4π

On the other hand, the Lorentz field is a sum of the contribution that arises from the moments lying outside the Lorentz sphere and is given as

$$\mathbf{B}_L = \frac{4\pi}{3}\mathbf{M}_b \tag{2.36}$$

where $\mathbf{M}_b$ is the bulk magnetization, hence $\mathbf{B}_L$ and $\mathbf{B}_{dem}$ vanish for antiferromagnets, helical and conical phases.

With the above formalism of the local field at the muon $\mathbf{B}_\mu$ and in the presence of applied external magnetic field $\mathbf{H}_{ext}$, the muon Knight shift K_μ can be extracted considering the shift in frequency, K^*_μ. On effecting corrections of the Lorentz and demagnetization fields, the frequency shift K^*_μ is given as:

$$K^*_\mu = \frac{|\mathbf{B}_\mu| - |\mathbf{H}_{ext}|}{|\mathbf{H}_{ext}|} = \frac{\langle\omega_\mu\rangle}{\omega_{ext}} - 1 \tag{2.37}$$

and the muon knight shift K_μ can be calculated as:

$$K_\mu = K^*_\mu - \left(\frac{4\pi}{3} - \overline{\mathbf{N}}\right)\chi \tag{2.38}$$

where χ is the bulk magnetic susceptibility

2.6 Experimental methods for muon stopping site determination

As already pointed out, muon stopping sites in samples are not known *a priori* in μSR experiments and are crucial for the complete analysis and understanding of local interactions with the μSR method. The muon site can be assigned, in fortunate cases, directly by experiments, such as:

- **ZF-μSR and muon dipolar field sum method:** For magnetically ordered materials, ZF-μSR measures the muon precession frequency and in turn the local field at the muon site. For magnetic samples where the Fermi-contact field at the muon is negligible, the magnetic moments and the spin structure are known, it may be sufficient to guess the muon site in order to compute the dipolar field sums. A comparison with the experimental local field can be used to validate the assignment. This is also done for the fields from nuclear dipoles in materials without magnetic order. Also, for the muon forming bonds with fluorine in some fluoride materials, the muon site can be determined from the F-μ-F oscillations. This is not a universal protocol, but in fortunate cases a very good agreement may provide convincing evidence.

- **Measurement of dipolar contribution to the Knight shifts in single crystals:** The dipolar contribution to the Knight shift depends on the dipolar coupling tensor. This method is not readily available since it requires adequate single crystals. It basically involves measuring the angular dependence of the Knight shift in μSR experiment and comparing them with the calculated angular dependence of the dipolar fields for different sampled muon sites. This approach has been employed to determine and predict the muon stopping sites in hcp structured materials of UPd_2Al_3, $PrNi_5$ and $LaNi_5D_3$ ([18] and references therein).

- **Level crossing resonance (LCR) method:** The LCR approach can be used to determine the implantation site of paramagnetic muonium (μ) and diamagnetic muon (μ^+) in semiconducting samples. The location site of the muon are determined by the positions of the resonances that allow both the angles and bond distances of the implanted muon and the host nuclei to be found. However, it is required for the host nuclei to be quadrupolar, since the LC resonances can occur at fields for which the muon Zeeman energy matches the combined Zeeman and quadrupolar energy of the nucleus. Also, with the LCR method, the hyperfine structure of the nuclei can be resolved, with this the local environment and muon implantation site can be determined. These approaches combined with the ZF- μSR method described above has been

used to determine the muon site and muon bond distances in GaAs [11, 12] since both the Ga and As nuclei are quadrupolar ($I > 1/2$). This method cannot be used in a wide range of materials since it can only be used in samples with quadrupolar nuclei and samples were it is expected for the muon to bond with the host nuclei.

From the descriptions above, one can deduct that the muon implantation stopping sites are not immediately obtained from μSR data, further calculations and analysis are always needed to be able to determine the muon site. The theoretical approaches proposed and described in this thesis allow to determine the candidate muon implantation sites in magnetic materials. For validation purposes, the calculated muon implantation sites were compared and used to reproduce experimentally measured data. Also, with the above experimental methods, the effect of the muon and the extent of the distortion induced by the muon in the sample especially on nearest neighbour are not known. However, the theoretical *first principle* approaches proposed allow to describe and quantify the muon effects in these samples.

2.7 Experimental methods for muon contact field determination

The hyperfine field at the muon is not easy to determine by experimental methods, since it requires the knowledge of the muon site which is not known apriori.

Experimental methods for the calculation of the Fermi-contact hyperfine field include:

- If the muon site is known, local field at the muon is given by μSR and the magnetic structure of the lattice is known, in principle the contact hyperfine field is determined by subtraction from Eq. 2.29. This scheme might apply if e.g. DFT calculations of the local site yield a non controversial unique assignment.

- From Eq. 2.31 the muon hyperfine coupling is proportional to the spin density at the muon site. Experimental methods including neutron diffraction has been used to measure the spin density of the unperturbed unit cell. An enhancement factor is introduced to mimic the effect of the muon on the lattice. This approach is quite rough. It was used in early experiments to estimate the muon hyperfine field of elementary transition metals[19, 20]

- Also measuring the paramagnetic shift provides some information on the spin density at the muon site. It involves a shift in the muon precision

frequency for a sample in the paramagnetic static induced by an applied magnetic field. Knight shift measurements on single crystals, scanning many different sample orientations in the external field provide a mapping of the shift tensor. This is a hard experiment if demagnetization is relevant, since it requires an ellipsoidal sample shape. The comparison of experimental data to predictions from Eq. 2.34, 2.37 and 2.38 depend on four constants: the muon site coordinates and the contact coupling. This approach has been used to estimate the contact hyperfine field of MnO [21, 22].

However, in this thesis I described the approach to calculate the muon contact hyperfine field from first principles and demonstrated the accuracy of this approach in selected metallic compounds.

3

Electronic structure theory

This chapter contains a short description of electronic structure theory and methods used for the calculations presented in this thesis.

3.1 Many-body problem

Systems made up of interacting electrons and nuclei are generally described by the many body problem. To obtain the properties of these systems, it is required to solve the Schrödinger equation in the form:

$$\hat{H}_{tot}\Psi(\{\mathbf{r}_i\},\{\mathbf{R}_I\}) = E\Psi(\{\mathbf{r}_i\},\{\mathbf{R}_I\}) \tag{3.1}$$

where in atomic units,

$$\hat{H}_{tot} = -\sum_i \frac{{\nabla_i}^2}{2} - \sum_I \frac{{\nabla_I}^2}{2M_I} + \frac{1}{2}\sum_{i\neq \mathrm{j}} \frac{1}{|\mathbf{r}_i - \mathbf{r}_j|} - \sum_{i,I} \frac{Z_I}{|\mathbf{r}_i - \mathbf{R}_I|} + \frac{1}{2}\sum_{I\neq J} \frac{Z_I Z_J}{|\mathbf{R}_I - \mathbf{R}_J|} \tag{3.2}$$

The total Hamiltonian operator, $\hat{H}_{tot}$ depends on the electronic coordinates $\mathbf{r}_i$ and on the nuclear coordinates $\mathbf{R}_I$. The terms on the right in Eq. 3.2 are: the electronic and nuclei kinetic energy, Coulombic repulsion between electrons and nuclei, attraction between electrons and nuclei and repulsion between nuclei. The system energy is represented by E and $\Psi(\{\mathbf{r}_i\},\{\mathbf{R}_I\})$ is the wavefunction dependent on electronic and nuclear coordinates. The form of this wavefunction is not known, if known then all the observable quantities of the system can be calculated.

To solve this problem, first one considers the *Born-Oppenheimer* (BO) approximation [23]. Here, considering that the nucleus is heavier than an electron by at least 1840 times, the problem can be separated into electronic and nuclear problem. The BO approximation allows to write the many body wavefunction $\Psi(\{\mathbf{r}_i\},\{\mathbf{R}_I\})$ separately into the electronic wavefunction $\psi(\mathbf{r}_i,\mathbf{R}_I)$ and nuclear wavefunction $\Phi(\mathbf{R}_I)$ in the form;

$$\Psi(\{\mathbf{r}_i\},\{\mathbf{R}_I\}) = \psi(\mathbf{r}_i,\mathbf{R}_I)\Phi(\mathbf{R}_I) \tag{3.3}$$

Hence, the Hamiltonian H for the electronic problem solved by $\psi(\mathbf{r}_i, \mathbf{R}_I)$ can be written as;

$$H = -\sum_i \frac{{\nabla_i}^2}{2} + \frac{1}{2}\sum_{i \neq \text{J}} \frac{1}{|\mathbf{r}_i - \mathbf{r}_j|} - \sum_{i,I} \frac{Z_I}{|\mathbf{r}_i - \mathbf{R}_I|} \tag{3.4}$$

With the BO approximation, the nuclear problem is solved with an *effective* potential resulting from the electronic problem, while various approximations including the the Hartree and Hartree-Fock methods[24–26] have been employed in solving the Schrödinger equation of the electronic system. The Hartree-Fock method neglects electron-electron correlation, whereas DFT accounts for it. DFT has a primary role for calculations in this thesis, both for this reason as well as for the wide availability of its computational implementation.

3.2 Density functional theory

DFT allows the ground state properties of many interacting electron wavefunction to be treated as functionals of one electron density. Thus, with DFT the problem of finding the wavefunction of N interacting electrons is transformed into a problem of determining the electron density with a one-electron potential. The basis of the DFT method is contained in the two theorems of Hohenberg and Kohn.[27] The theorems include:

- **First Theorem**: This theorem states that any physical quantity of the interacting electron gas and the external potential $V_{ext}(\mathbf{r})$ of a many particle system are uniquely determined by the ground state particle density.
- **Second Theorem**: In this theorem it is shown that that the exact ground state density is the density functional that minimizes the total energy functional $E[n(\mathbf{r})]$. Such that, if the form of the energy functional $E[n(\mathbf{r})]$ is known, then the ground state one body density is delivered by solving the minimum energy problem. The value of the functional at the minimum that gives the ground state is of the form;

  $$\min E[n(\mathbf{r})] \equiv E[n_o(\mathbf{r})] \equiv E_o \tag{3.5}$$

  where the total energy functional is given by;

  $$E[n(\mathbf{r})] = T[n(\mathbf{r})] + U(\mathbf{r}_i, ..., \mathbf{r}_N) + \int d\mathbf{r} n(\mathbf{r}) v_{ext}(\mathbf{r}) \tag{3.6}$$

  $T[n(\mathbf{r})]$ represents the internal kinetic energy, $v_{ext}(\mathbf{r})$ represents the external potential energy and $U(\mathbf{r}_i, ..., \mathbf{r}_N)$ represents the inter-particle interaction.

Even though the form of the energy functional has been demonstrated by the Hohenberg-Kohn theorems, the method of approaching the solution to this functional was not given, however with the Kohn-Sham equations this task is achieved.

3.2.1 Kohn-Sham equation

Kohn and Sham proposed that provided that the ground state density of interacting particles system is same as that of a non-interacting one, thus the density functional problem of interacting particles can be replaced by a self-consistent problem of non-interacting particles.[27] This implies that any interacting one-body density is also a solution of the non-interacting problem. In practice, for any interacting density $n(\mathbf{r})$ there is a suitable effective potential $\tilde{v}(\mathbf{r})$ that delivers $n(\mathbf{r})$ as solution of the non-interacting problem, so that the total energy functional is of the form:

$$E[n] = T_0[n] + U_H[n] + E_{xc}[n] + \int d\mathbf{r} n(\mathbf{r}) v(\mathbf{r}) \tag{3.7}$$

where $T_0[n]$, $U_H[n]$ and $E_{xc}[n]$ are the independent-electron kinetic energy, Hartree energy, exchange-correlation energy respectively. The minimum condition for the interacting system is in the form:

$$\frac{\delta E}{\delta n(\mathbf{r})} = \frac{\delta T_0}{\delta n(\mathbf{r})} + v_H(\mathbf{r}) + v_{xc}(\mathbf{r}) + v_{ext}(\mathbf{r}) = \frac{\delta T_0}{\delta n(\mathbf{r})} + \tilde{v}(\mathbf{r}) = \mu \tag{3.8}$$

where

$$v_{xc}([n];\mathbf{r}) = \frac{\delta E_{xc}}{\delta n(\mathbf{r})} \tag{3.9}$$

$$v_H([n];\mathbf{r}) = \frac{\delta U_H}{\delta n(\mathbf{r})} = \int d\mathbf{r} \frac{n(\mathbf{r}')}{|\mathbf{r} - \mathbf{r}'|} \tag{3.10}$$

$\tilde{v}$ is the effective potential, which is also referred to as the Kohn-Sham potential. This potential results form the summation of the Hartree (v_H), exchange-correlation (v_{xc}) and external (v_{ext}) potential.

Thus, with Eq. 3.8 the many-particle interacting problem can be solved as a non-interacting one in an effective density-dependent external potential $\tilde{v}(\boldsymbol{r})$, with the Kohn-Sham equation written in the form;

$$\left[-\frac{\nabla^2}{2} + \tilde{v}(\boldsymbol{r})\right] \psi_i(\mathbf{r}) = \epsilon_i \psi_i(\mathbf{r}) \tag{3.11}$$

where $\psi_i(\mathbf{r})$ is a single-electron wavefunction. Therefore, the Kohn-Sham (KS) equation is a single electron Schrödinger equation with an effective potential.

In DFT, the solution to the density and total energies are achieved *self-consistently*. The starting point of the iteration is the choice of the guess initial density $n(\mathbf{r})$, after which further iteration of the Kohn-Sham equation continues until self-consistency and other convergence criteria are achieved. Fig. 3.1 contains the flow chart that describes the iteration process.

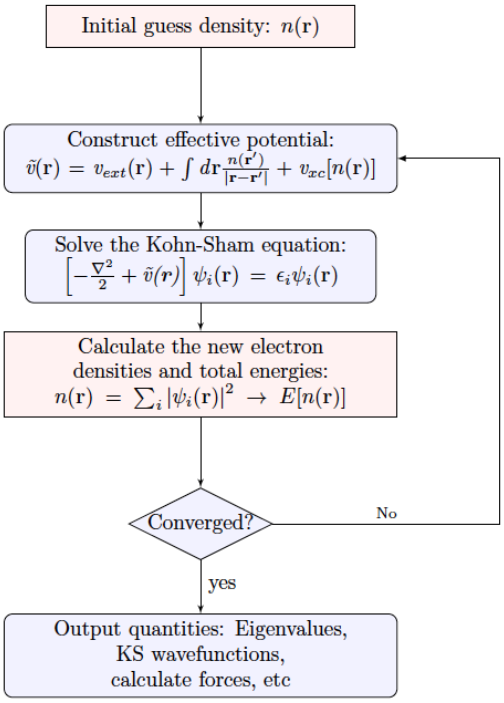

Figure 3.1: Self-consistent iteration flow chart

3.2.2 Exchange-correlation functional

As already described, in the DFT method, the interactions between electrons are accounted for by the Hartree term and the exchange-correlation functional E_{xc}. However, the actual form of E_{xc} is not known and are described by approximate functionals based upon the electron density. Two most popular approximations including the one used for the studies presented in this thesis are; the local density approximation(LDA) and the generalized gradient approximation (GGA).

- **LDA**: In this approximation, the exchange-correlation energy density at a point $\mathbf{r}$ is equal to the exchange-correlation energy density of a uniform electron gas that has the same density at that point. The form of this

functional is given as;

$$E_{xc}[n(\mathbf{r})] \simeq \int n(\mathbf{r})\epsilon_{xc}(n(\mathbf{r}))d\mathbf{r} \tag{3.12}$$

One of the limitation of the LDA approach is that it doesn't capture the inhomogeneities in the electron density about $\mathbf{r}$. A homogeneous electron density is always assumed with this approximation. Because of this, the LDA is known to over-bind, especially in molecules.

Some examples of exchange-correlation functional parametrized with the LDA method include: PZ(Perdew-Zunger) [28] and PW92(Perdew-Wang-92)[29].

- **GGA**: Unlike the LDA method, in other to account for inhomogeneities in the electron density, the GGA functional depends on the local density as well as on the gradient of the density. The general form of the GGA is:

$$E_{xc}[n(\mathbf{r})] \simeq \int n(\mathbf{r})\epsilon_{xc}(n(\mathbf{r}), \nabla n(\mathbf{r}))d\mathbf{r} \tag{3.13}$$

Some common variations of the parametrized exchange correlation functional include: Perdew-Burke-Ernzerhof (PBE) [30] and LYP [31] including Becke gradient exchange functional [32].

3.3 Hubbard U correction (DFT+U)

In strongly-correlated electron systems, the LDA and GGA approximations to V_{xc} gives poor and inaccurate band gap description. Also, they fail to reproduce correctly the properties in magnetic systems. The over-localization observed with LDA and GGA are due to the electron self interaction.

The DFT+ Hubbard corrections popularly known as *DFT + U*, involves using the Hubbard model with effective on-site interactions on *localized* orbitals to the correction of the approximate DFT energy. [33–36] The Hubbard term principally offers correction to the unphysical curvature of the DFT energy with a contribution that penalizes partial orbital occupation. The correction to this unphysical curvature in the DFT+U energy can be written in the form;

$$E_{DFT+U}[n] = E_{DFT}[n] + E_U[n_i^\sigma] \tag{3.14}$$

where the second term on the right is a simple approximation to Hubbard corrections.[36] Mostly, the effect of the on-site U on the band structure, is to lower the valence band maximum and shifting the conduction band minimum to higher energies giving a larger band gap. Also, determining the value of U for each specific material is crucial to the proper use of this approximation.

3.3.1 Calculation of the U value

In DFT+U calculations, the values of U are sometimes determined by choosing values that give calculations results that are consistent with the experimentally observed results. This approach can limit the usefulness of the whole approach for *ab initio* predictions.

In addition, conflicting values of U have been used for calculations relating to the same material. It is important to note however, that the value of U is not universal and depends on the approximation and chemical environment of the sample considered, since U in this case is not necessarily the Hubbard exchange interaction but rather a correction on the DFT energy. The value of U can be estimated *ab initio* and self consistently by means of the linear response to small perturbations in the form: [36, 37]

$$U = \frac{\partial \alpha_I^{KS}}{\partial n_I} - \frac{\partial \alpha_I}{\partial n_I} = (\chi_0^{-1} - \chi^{-1})_{II} \tag{3.15}$$

where α is a small shift on the Kohn-Sham potential KS, n_I the occupation levels of each atom site I, the suffix II indicates the diagonal element for the difference on the right and χ are the response matrices of the change in the occupation number for small perturbations.

In practice, small perturbation is applied to the Kohn-Sham potential in an adequate supercell size, collecting atom occupations in the response matrix. Sufficient supercell size is required to avoid the interaction error of the applied small potential perturbation.

The value of U is obtained self-consistently in a series of steps:

- First the U_{out} is calculated by the linear response method without an input value of (U_{in}) i.e for U=0.0
- Then, more values of U_{out} are calculated for different input values of U_{in}. This allows to include in the determination of the U value the effect of the changes in the occupation number due to the Hubbard correction.
- Lastly, instead of imposing straightforward self consistency [36, 37], a corrected self consistent value U_{scf} is obtained by a finite-U linear extrapolation (as shown in Fig. 3.2) in the form:

$$U_{out} = U_{scf} - \frac{U_{in}}{m} \tag{3.16}$$

where m is an effective degeneracy parameter on the changing orbitals due to the small perturbation.

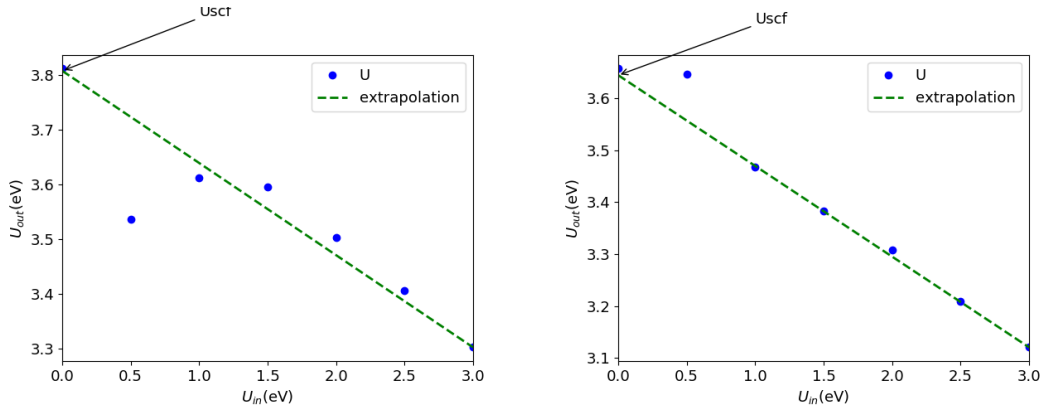

(a) For NaFeAs **(b)** For $NaFe_{0.5}Ni_{0.5}As$

Figure 3.2: Self-consistent calculated value of U, U_{scf} using the linear response to small perturbation approach.

I have used the self-consistent linear response method to evaluate the U value on Fe atom in NaFeAs and $NaFe_{0.5}Ni_{0.5}As$. The values of U are 3.808 and 3.644 eV respectively. These values for NaFeAs are specifically for calculations discussed in Sec. 4.2. Fig. 3.2 contains the self-consistent linear response for the calculations of U in NaFeAs and $NaFe_{0.5}Ni_{0.5}As$.

3.4 Magnetism in DFT

Magnetism originates from incomplete or open shells in atoms, typically those of the d and f shells. In DFT, magnetism are described in relation to spin polarization such that spin alignment are considered.

For a spin unpolarized system, the spin up ($\uparrow$) and spin down ($\downarrow$) are same, so that only half of the Kohn-Sham orbitals are considered. The form of the density n($\mathbf{r}$) is written as:

$$n(\mathbf{r}) = 2\sum_{i=1}^{N/2} |\psi_i(\mathbf{r})|^2 \tag{3.17}$$

where N is the total number of electrons in the system. Extra occupancy factors are needed in the density description when densities in metals are considered.

However, for a spin polarized system, by choosing an axis of quantization for instance the z direction, the densities for the spin up and spin down states can be written in the form;

$$n^{\uparrow}(\mathbf{r}) = 2\sum_{i=1}^{N^{\uparrow}} \left|\psi_i^{\uparrow}(\mathbf{r})\right|^2 \tag{3.18}$$

and

$$n^{\downarrow}(\mathbf{r}) = 2\sum_{i=1}^{N^{\downarrow}} \left|\psi_i^{\downarrow}(\mathbf{r})\right|^2 \tag{3.19}$$

Here, one can observe that there are now different orbitals for the up and down spin $\psi^{\uparrow}$ and $\psi^{\downarrow}$, such that the total number of electrons N, is now a sum of the up and down spin components; $N = N^{\uparrow} + N^{\downarrow}$. With this, the total charge density $n(\mathbf{r})$ can be written as;

$$n(\mathbf{r}) = n^{\uparrow}(\mathbf{r}) + n^{\downarrow}(\mathbf{r}) \tag{3.20}$$

and total magnetization $m(\mathbf{r})$ as ;

$$m(\mathbf{r}) = n^{\uparrow}(\mathbf{r}) - n^{\downarrow}(\mathbf{r}) \tag{3.21}$$

The consequence of the spin polarization is such that the Kohn-Sham total energy functional already shown in Eq. 3.7 is now a functional of the spin up and spin down densities. Then, the total energy functional can now be written as;

$$E[n^{\uparrow}, n^{\downarrow}] = T_0[n] + E_{ext}[n] + E_H[n] + E_{xc}[n^{\uparrow}, n^{\downarrow}] \tag{3.22}$$

One can notice that from the definition of the total density above, Eq. 3.20 $E_H[n] = E_H[n^{\uparrow} + n^{\downarrow}]$. With spin polarization, the minimization of the total energy functional already described in Eq. 3.8 with the two different up and down densities are not equal, i.e;

$$\frac{\delta E}{\delta n^{\uparrow}(\mathbf{r})} \neq \frac{\delta E}{\delta n^{\downarrow}(\mathbf{r})} \tag{3.23}$$

From Eq. 3.22, one can deduce that the description of the magnetic ground state of the system, enters into the exchange and correlation energy functional as $E_{xc}[n^{\uparrow}, n^{\downarrow}]$. Considering Eq. 3.20 and 3.21 the exchange and correlation functional can be written as functionals of the total density and magnetization as $E_{xc}[n, m]$. Such that $E_{xc}[n, m]$ is now minimized as;

$$v_{xc}(\mathbf{r}) = \frac{\delta E_{xc}[n, m]}{\delta n(\mathbf{r})} \tag{3.24}$$

and

$$B_{xc}(\mathbf{r}) = \frac{\delta E_{xc}[n, m]}{\delta m(\mathbf{r})} \tag{3.25}$$

where $B_{xc}(\mathbf{r})$ represents the exchange correlation potential part that describes the spin polarization. The Kohn-Sham equation in Eq. 3.11 for the spin polarized case in the collinear regime is now written as;

$$\begin{aligned}\left[-\frac{\nabla^2}{2} + v_{ext}(\mathbf{r}) + v_H(\mathbf{r}) + v_{xc}(\mathbf{r}) + B_{xc}(\mathbf{r})\right]\psi_i^{\uparrow}(\mathbf{r}) = \epsilon_i^{\uparrow}\psi_i^{\uparrow}(\mathbf{r}) \\ \left[-\frac{\nabla^2}{2} + v_{ext}(\mathbf{r}) + v_H(\mathbf{r}) + v_{xc}(\mathbf{r}) - B_{xc}(\mathbf{r})\right]\psi_i^{\downarrow}(\mathbf{r}) = \epsilon_i^{\downarrow}\psi_i^{\downarrow}(\mathbf{r})\end{aligned} \tag{3.26}$$

The two KS equations are independently solved such that it requires twice more computational resources to perform the calculation for a spin polarized calculation than that for a non polarized calculation. The DFT treatment of the exchange correlation functional within the spin polarized formalism is generally referred to as *Local Spin Density Approximation* (LSDA). However, the total DFT energy of the spin polarization in the collinear formalism described above does not depend on the axis of quantization, the spin-orbit coupling effects are require to realize this.

3.5 Basis set and Brillouin zone integration

In solving the Kohn-Sham equations, the density distribution $n(r)$ and KS wavefunction are expanded using a basis set. With the periodicity of the crystal lattice, and following the Bloch's theorem, the one electron wavefunction with wave-vector $\mathbf{k}$ can be written in the form:

$$\psi_{i,k}(\mathbf{r}) = u_{i,k}(\mathbf{r})e^{i\mathbf{kr}} \tag{3.27}$$

with $u_{i,k}(\mathbf{r})$ being periodic and written as $u_{i,k}(\mathbf{r}) = u_{i,k}(\mathbf{r} + \mathbf{R})$. If the periodic function $u_{i,k}(\mathbf{r})$ is expressed in the plane wave basis set, then the one electron wavefunction is a combination of reciprocal lattice vectors (G) plane waves in the form:

$$\psi_{i,k}(\mathbf{r}) = \sum_G c_{i,k+G}e^{i(\mathbf{k}+\mathbf{G}).\mathbf{r}} \tag{3.28}$$

The summation over all the reciprocal lattice vector G is truncated by a cut off energy, E_{cut} such that for each $\mathbf{k}$ the lattice vector included in the summation is $|\frac{(\mathbf{k}+\mathbf{G})^2}{2}| < E_{cut}$.

The Brillouin zone integrations were performed using the Monkhorst-Pack scheme [38]. This scheme involves sampling the reciprocal cell with a uniform $(n \times n \times n)$ grid mesh that allows the number of k-points in the Brillouin zone

to be reduced to the minimum, the so-called irreducible wedge. The choice of the mesh used for the integration is chosen considering the convergence of the properties investigated.

For metals, because of the presence of the Fermi surface, the discontinuities in occupation numbers are smeared out by introducing a fictitious temperature in the delta function smoothening within the Marzari-Vanderbilt [39] function, with the width of the function determined by convergence tests.

3.5.1 Pseudopotentials

In the vicinity of the nucleus, there is a rapid oscillation of the electronic wavefunction, that for rapidly varying functions the plane-wave expansion converges very slowly. In order to circumvent this problem and considering that the valence electrons are most important in determining the properties of solids, the *pseudopotential* formalism are used to replace the potential in a small core region around the nucleus. . Pseudopotential formalism involves transforming the rapidly oscillating wavefunctions into smooth wavefunctions, giving an effective potential that mimics the effects of the nucleus and the core electrons on the valence electrons. This is such that at distances larger than a sufficient cutoff $\mathbf{r}_c$, the all-electron wavefunction ψ^σ and the pseudo wavefunction $\tilde{\psi}^\sigma$ coincide.

$$\psi^\sigma(\mathbf{r}) = \tilde{\psi}^\sigma(\mathbf{r}),\ \mathbf{r} > \mathbf{r}_c \tag{3.29}$$

Various flavours of the pseudopotential formalism exist, they include:

- **Norm-Conserving Pseudopotential (NC)**: In this formalism, the pseudopotential is constructed with the condition that the total charge of the pseudo wavefunction equals that of all-electron wavefunction. However, in order to achieve this, short core radius is required, such that the cutoff is large. This Pseudo is often referred to as *hard* and requires large number of plane waves.
- **Ultrasoft Pseudopotentials (UP)**: This formalism relaxes the charge constraint criterion to obtain smoother pseudo-wavefunctions. With the smoothening less number of plane waves are required.
- **Projector Augmented-Wave Method (PAW)**: The PAW[40–43] method involves the mapping of the valence pseudo wavefunctions $\left|\tilde{\psi}_i^\sigma\right\rangle$ onto the corresponding all-electron wavefunctions $|\psi_i^\sigma\rangle$, with a linear transformation operator $\mathcal{T}$, such that;

$$|\psi_i^\sigma\rangle \simeq \mathcal{T}\left|\tilde{\psi}_i^\sigma\right\rangle \tag{3.30}$$

and

$$\mathcal{T} = 1 + \sum_{\lambda} [|\phi_\lambda\rangle - \left|\tilde{\phi}_\lambda\right\rangle] \langle \tilde{p}_\lambda | \mathcal{T} = 1 + \sum_{i} \left(|\phi_i\rangle - |\tilde{\phi}_i\rangle \right) \langle p_i | \tag{3.31}$$

where the index λ represents the angular momenta and number of projectors localized as atomic sites $\mathbf{R}$, $|\phi_\lambda\rangle$ are the all-electron atomic like states from the solution of an isolated atom, $\left|\tilde{\phi}_\lambda\right\rangle$ the corresponding pseudo states and $\langle \tilde{p}_\lambda|$ are localized projector functions with the condition $\left\langle \tilde{p}_\lambda | \tilde{\phi}_\nu \right\rangle = \delta_{\lambda\nu}$. With the projector functions, the PAW pseudo-wavefunction and the all-electron wavefunction have the same accuracy.

One of the advantages of the PAW method is that it gives access to the behaviour of the wavefunction in the core region, approximated by the pseudopotential approach. This is done by a frozen-core reconstruction of the pseudo-wavefunction to the all electron wavefunction. This particular property of the PAW is very important for the calculation of the muon hyperfine parameters, since the core region effect which has a significance contribution are included with this approach.

3.6 Structure optimization

An important concept in DFT is that the equilibrium structure of a crystal (at zero temperature) can be achieved by requiring that the energy converges and the forces on the atoms vanish. The minimization algorithm used is that of Broyden–Fletcher–Goldfarb–Shanno (BFGS).[44] The force calculation is practicable thanks to the Hellmann-Feynman theorem[45], a quantum mechanical version of the classical theorem of virtual forces, that relates the conservative force acting on a mass to the gradient of the potential. The force $\mathbf{F}_I$ on atom I is written as;

$$\mathbf{F}_I = -\frac{\partial E(\mathbf{R})}{\partial \mathbf{R}_I} = -\left\langle \Psi(\mathbf{R}) \left| \frac{\partial H_{BO}(\mathbf{R})}{\partial \mathbf{R}_I} \right| \Psi(\mathbf{R}) \right\rangle \tag{3.32}$$

This means that trial lattice parameters can be chosen as a starting point, and, assuming that they are not too far from equilibrium conditions they can be varied until all forces vanish, thus providing a DFT estimate of the lattice parameter values. The process is normally referred in DFT parlance as *relaxation*.

3.6.1 Implementation

For the DFT calculations presented in this thesis unless otherwise stated, the Quantum ESPRESSO (QE) suite of codes [46] was used. In this code, mainly

the plane-wave DFT and other electronic structure approximations used for the calculations are implemented. The QE code is parallelized for optimal usage on available high performance computing (HPC) and graphics processing units (GPU) computers [1]. For large cells required for the muon/hydrogen impurity treatment, the parallelism levels in QE were used for optimal performance in the calculation on the supercomputers.

[1] The following supercomputers were used to perform the calculations: Piz-Daint at the Swiss National supercomputing center (CSCS) Switzerland, SCARF Cluster at the STFC computing centre United Kingdom and cluster at UNIPR Italy.

4

Muon stopping sites in selected materials

In this chapter, I carried out atomistic simulations in selected materials of current interest in which μSR experiments were carried out either directly by us or in collaboration with other experimental groups. The first aim of my effort is to determine the stopping site of the muon, to help in the data interpretation. DFT offers an opportunity to further investigate the properties of the material and to assess the extent of lattice and electronic structure perturbation by the induced muon. The three compounds considered in this chapter belong to the category of materials, where unconventional properties emerge from the interplay of charge, spin, and orbit degrees of freedom. Therefore this part of the work represents an application of the techniques that I have been developing in cases of current interest.

In low-temperature μSR experiments the incident muons thermalize with the lattice and stops at interstitial sites. The implantation site of the muon in various materials has been successfully identified with a number of increasingly accurate theoretical approaches. In earlier calculations, the identification of muon sites were based on the analysis of the unperturbed Coulomb or electrostatic potential within either the simple Thomas Fermi model or the DFT approach. In this approach the muon implantaion site is taken to be at the locations of the unperturbed electrostatic potential (UEP) where positive charged impurities are likey to be trapped. It requires limited computer resources and has been used specifically for muon sites in various family of high temperature superconductors (HTS), including the (1111)[47–49], (11) [50] and (122)[51] iron pnictides. It is reasonably accurate in good metals, where the muon positive charge is efficiently screened by conduction electrons and the muon often does not form a chemical bond.

The UEP more commonly fails in insulators and intrinsic semiconductors, where the formation of a muon bound state produces non negligible local rearrangements of the atoms. An alternative approach that captures these distortions consists in inserting the muon positive charge, identical to that of a charged hydrogen , in the *ab-initio* calculations. The equilibrium state is obtained minimizing the

forces acting on the cell. In the equilibrium configuration the masses of the atoms are irrelevant and, within Born-Oppenheimer approximation, the mass difference between the muon and the proton is irrelevant. The muon mass was discussed in Chapter 6. In the present chapter it is ignored: muon and hydrogen are equivalent in the DFT context.

Another important practical issue is that this method requires a rather large supercell to treat the muon as an extremely diluted impurity, and this requires much larger computer resources. I will refer to this DFT method as the supercell method.

The supercell method has been used to study the muon implantation site in a variety of materials, including insulators[52, 53], semiconductors[41, 54], high temperature superconductors [55, 56], and and on systems with special interest because of their magnetic structure [57–60] etc. It has been used in particular in some fluoride insulators [61, 62], where a strong dipolar coupling between the muon and its few nearest neighbour fluorine nuclei provides an experimental measure of the muon-fluorine distance [63].

The supercell method may be optimized by several different strategies, that I will briefly sketch end exemplify in the rest of this chapter. Since the choice of a method must compromise between accuracy and computer resource cost, the combination of UEP and supercell method often turns out to be the solution of choice[60, 64]. More detailed reviews on these methods and the materials where the muon site has been calculated can be found in Refs. [65, 66].

The rest of the chapter is dedicated to the calculation of the implantation site of the muon with DFT method and subsequent dipolar field simulations in selected materials of interest. I first discuss the different strategies to identify the muon sites, and then illustrate them with three specific cases of magnetic and superconducting materials where this knowledge provided new insight on their properties: in $NaFe_{1-x}Ni_xAs$, one of the many families of iron pnictide superconductors, where μSR probes the coexistence of magnetism and superconductivity; in $Yb_2Pd_2In_{1-x}Sn_x$, a heavy fermion family where the competition between Kondo physics and RKKY exchange coupling originates possibly more than one quantum critical point; finally in the unconventional superconductor Sr_2RuO_4, notably the first known example of a p-wave gap, accompanied by time reversal symmetry Breaking (TRSB) due to the onset of spontaneous orbital currents, that are directly detected by muons. The knowledge of the muon site indeed allows us to confirm structure and Fe magnetic moment in $NaFe_{1-x}Ni_xAs$; to predict the internal field at the muon site at ambient pressure in $Yb_2Pd_2In_{1-x}Sn_x$ and to suggest a structural magnetic transition at high pressure; finally, to quantify the effect of the muon-induced local distortion on the intrinsic electronic and density of state distribution of Sr_2RuO_4, advocating for the intrinsic nature of spontaneous magnetic

field experienced by muons.

4.1 Site calculation strategy with *ab initio* techniques

The failure of the UEP method to describe the muon site is due to the neglect of the possible muon induced distortions. A straightforward way to account for them is to include the muon in the lattice during the calculation.

In all the DFT calculations performed for finding the muon site in this chapter, I used the plane-wave DFT with local spin density approximation (LSDA) where required. Here the muon was introduced in the sample as a hydrogen impurity considering that DFT is a solution of only the electronic problem in the total Hamiltonian of the Schrodinger equation describing the many body problem(see Sec. 3.1, Eq. 3.4). The neutral hydrogen impurity was used in the DFT calculations in this section and this is justifiable because it is expected and has been shown [61, 62, 65] that in metals the positive charge of the muon are effectively screened by the conduction electrons that gather around it due to charge attraction, thus for the whole cell the charge neutrality is maintained. However, this is not the case for high band gap insulators where the charged cells have to be considered in the calculation.

The muon must be considered within a supercell, consisting of more unit cell replicated along the three lattice vectors. This is common practice with dilute impurity problems, since the periodic boundary conditions introduce unwanted replicas of the impurity. Muons are actually implanted in an extremely dilute limit (practically only one at a time in the sample). The minimal requirement on the DFT calculation is that muon's replicas do not interact with each other and this is achieved by checking that the farthest atoms from the muon are nearly undistorted (both structurally and electronically). Therefore the supercell size is a compromise between the extent of the muon induced distortion and the available computational resources. In the studies presented here the total number of atoms was limited to a maximum of roughly 300.

Ideally, the DFT calculation should be performed with the muon already in the interstitial site. An optimized structure with the muon is achieved in the minimization by imposing that the forces acting on any atom, muon included, vanish. The forces are calculated by the Feynman-Hellman theorem (see Sec. 3.6). Therefore the muon must be introduced at a starting trial position and by minimizing total energy as well as forces the system will relax to the global or local minimum.

This method typically produces several different local minima, each with the muon in a different crystallographic site, that may be distinguished by the value

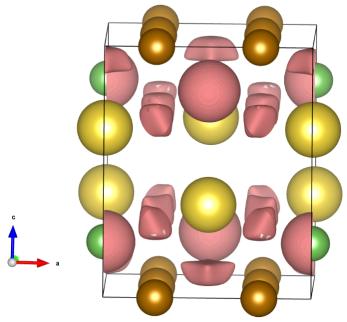

Figure 4.1: Unpertubed electrostatic potential of NaFeAs (in pink) plotted for Isosurface level of 0.78eV . The plot was visualized with *VESTA*.[67]

of the total energy calculated by DFT. In many materials muons occupy more than one site, with different probabilities, determining their contribution to the muon initial asymmetry. These sites are generally the lowest energy ones among those that an extensive DFT search can identify, but this is not necessarily the case since muon thermalization is a transient *epithermal* process (i.e. with local energies larger than k_BT). It is transient in the sense that it may not reach equilibrium in a muon lifetime. The only known solution is comparison between predictions and experiments.

Still, a thorough search of the DFT minima is a very resource-intensive process. One of the strenuous tasks is the choice of the trial starting position(s) of the muon before the force and energy minimization. I list below possible approaches for modelling the starting positions of the muon:

- **Search from the UEP minima**: Here, the electrostatic potential is calculated for the unit cell of the sample without introducing the muon while all the possible locations of trapping a positively charged impurity are considered as the starting trial muon positions. As an example I show in Fig. 4.1, the UEP sites for NaFeAs that will be discussed in the next section. However, in this case, the UEP sites are not sufficient since some of the possible implantation site of the muon are not captured with this method.

- **Uniform grid of trial positions**: Here the starting trial positions are uniformly spaced grid of positions in the unit cell with condition that the grid positions are atleast 1 Å away from the host atoms. The step of the grid must be matched to the extent of the muon site wandering in a single relaxation process, so that the entire interstitial space of the lattice is explored. The advantage of using a regular grid instead of a random site is that it allows an efficient use of symmetry to remove equivalent starting

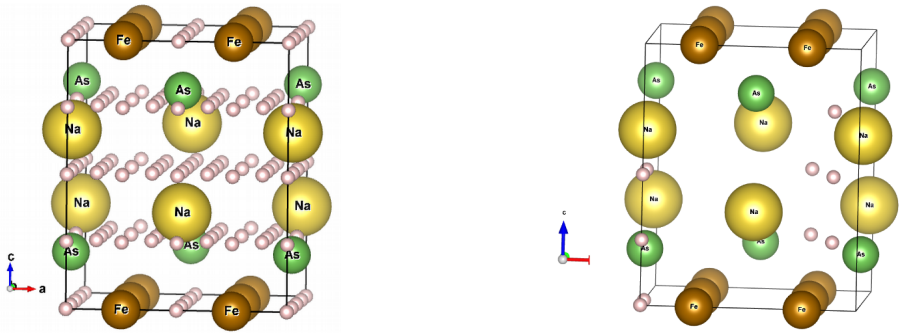

(a) **(b)**

Figure 4.2: a.) A 4×4×4 uniform grid of the initial muon position (pink balls) in NaFeAs b.) The reduction by the space group symmetry of NaFeAs of the $4 \times 4 \times 4$ grid to 10 inequivalent positions. The plot was visualized with *VESTA*.[67]

positions. This greatly reduces the number of different supercell relaxation calculations to be performed. As an example, Fig. 4.2 shows a $4 \times 4 \times 4$ uniform grid in a NaFeAs unit cell, where the 64 initial trial positions were reduced to 10 inequivalent positions imposing the space group symmetry of NaFeAs.

- **Hybrid method**: Here, the two approaches described above are combined while choosing not so large grid dimensions to reduce the starting initial positions. This also allows to optimize the computer resources requirement.

Two trial sites may relax to the same site. However the finite numerical accuracy of the two DFT calculations may lead to slightly different relaxed sites. Likewise an extensive search might result in a large number of candidate sites, distinguished by their coordinates and their total DFT energy. Combined inspection of their relative distances and energy difference allows them to be grouped in clusters of sites, adjacent to each other and with very close energy values, to be recognized as different realization of the same site. Symmetry reduction, like that used for the uniform grid, must be also applied also in this process, in order to identify symmetry equivalent crystallographic sites.

4.2 Stopping sites and magnetic moments in $NaFe_{1-x}Ni_xAs$

This section [1] includes a summary of μSR measurement and magnetic characterization describing the coexistence of magnetism and superconductivity with Ni doping in $NaFe_{1-x}Ni_xAs$ together with the DFT calculation of muon stopping sites. The candidate muon sites found with DFT allowed calculation of the local field at the muon. The comparison of these predictions with experiments provides an estimation of the Fe magnetic moment and confirms the magnetic structure in $NaFe_{1-x}Ni_xAs$.

$NaFe_{1-x}Ni_xAs$ is a member of the $'111'$ Iron-based high temperature superconductors (Fe-HTS). Fe-HTS includes the family of materials that exhibit unconventional superconductivity arising from the parent compounds with static antiferromagnetic (AFM) order of the Fe atoms. [68–70] Determining the physical mechanism that drives superconductivity in these materials is crucial to understanding the behaviour of these systems. Crucial information on these physical mechanism can be deduced by mapping and investigating the phase diagrams and also the superconducting (SC) gap structure. In the parent compound of many Fe-HTS, isovalent chemical substitution or application of pressure suppresses magnetic order and begets a SC dome.[71] Also, Fe-HTS exhibit a tetragonal-to-orthohombic structural distortion triggered by an electronic nematic order parameter at temperature T_s that precedes or occurs concurrently with the magnetic phase transition at temperature T_N. [68, 70, 72–75]

Zero-field DC susceptibility and Zero-field μSR have been performed [2] on single crystalline samples of $NaFe_{1-x}Ni_xAs$ with $x = 0, 0.4, 0.6, 1.0, 1.3$ and 1.5%. A phase diagram that summarizes the structural, magnetic, and SC transitions is shown in Fig. 4.3a, the collinear AFM spin structure of the undoped compound, NaFeAs is shown in Fig. 4.3b together with the summary of the measured magnetic and SC volume fractions in Fig. 4.3c.

The results of the volume sensitive μSR (Fig. 4.3c) offer strong evidence that both the ordered moment and fraction are partially or fully suppressed below T_C. This reduction of magnetic intensity is due to a strong reduction of both the ordered moment and magnetic volume fraction below T_C. The effect of superconductivity on magnetism intensifies as the doping level x increases, leading to

[1] The Contents of this section have been published by my research group and collaboration with other groups at [Phys. Rev. B 97, 224508 (2018)]

[2] The experiments were carried out by colleagues at the Columbia University, New York with the μSR performed using the Los Alamos Meson Physics Facility (LAMPF) spectrometer with a helium gas-flow cryostat at the M20 surface muon beamline ($\approx$ 4MeV) of TRIUMF in Vancouver, Canada and also the general purpose surface-muon instrument (GPS) at the Paul Scherrer Institute in Villigen, Switzerland.

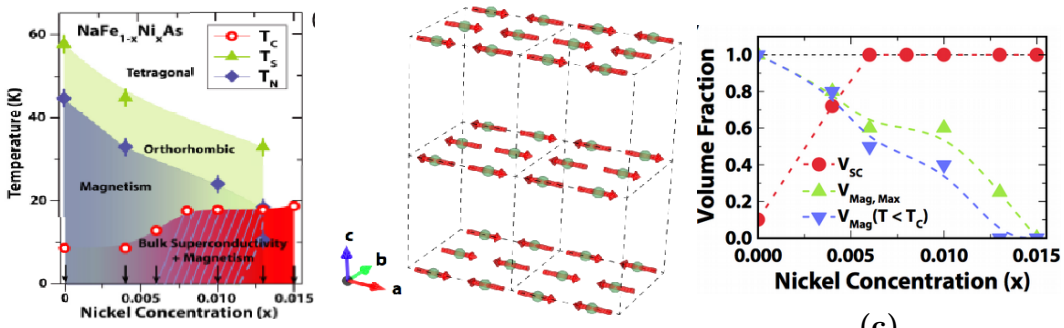

(a) (b) (c)

Figure 4.3: (a) Phase diagram of $NaFe_{1-x}Ni_xAs$ illustrating temperature and doping dependence of various orders, with structural and magnetic transitions obtained from Ref. [76] and displayed as fully-colored symbols. Transition temperatures T_N and T_C measured in this work are indicated with non-shaded symbols. (b) Collinear AFM spin structure of the undoped compound NaFeAs [67, 77] in a magnetic supercell, only Fe atoms (green) are shown for visual clarity. (c) Doping evolution of various volume fractions obtained from the present investigation. The colored dashed lines are guides to the eye to illustrate the doping dependencies of the SC volume fraction V_{SC}, the maximum magnetic volume fraction $V_{\mathrm{Mag,Max}}$ and magnetic volume fraction below T_C $V_{\mathrm{Mag}}(T < T_{\mathrm{C}})$.

a reentrant non-AFM state below T_C for $x = 1.3\%$. For x between 0 and 0.4% they are in homogeneous long range magnetically ordered state and magnetism becomes inhomogeneous for $x = 0.4\%$ and completely suppressed for $x = 1.5\%$. Ni doping increases suppressing of the magnetic order, such that there is an interplay between antiferromagnetism and superconductivity involving competition for the same electrons. There is a coexistence of AFM and SC orders, which has also been observed in several Fe-HTS including $BaFe_{2-x}Co_xAs_2$[78, 79], $Ba_{1-x}K_xFe_2As_2$[80] and $NaFe_{1-x}Co_xAs$.[81] As the temperature is lowered below T_c, the ordered magnetic moment size and nematic order parameter smoothly decrease, indicating that superconductivity and magnetic long range order compete for the same electrons. These results suggest an interesting scenario, in which the degree of competition between AFM and SC may be itself intrinsically inhomogeneous, varying as a function of position in the sample.

4.2.1 ZF-μSR and muon precession frequency

The observed μSR time spectra (muon ensemble polarization) of $x = 0$ and 0.4% in zero applied field (ZF-μSR) are shown in Figure 4.4. The spectra for $x > 0.4\%$ that completes the superconducting and magnetic characterization presented in

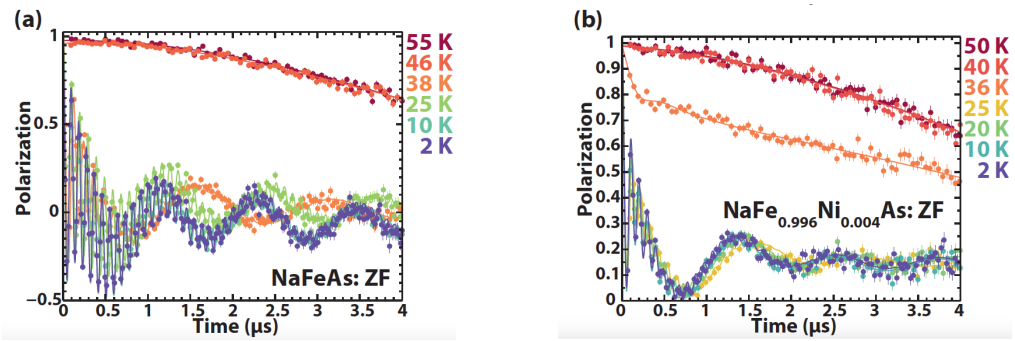

(a) **(b)**

Figure 4.4: ZF-μSR spectra on $NaFe_{1-x}Ni_xAs$. (a) and (b) are muon spin polarization in zero field for $NaFe_{1-x}Ni_xAs$ for $x = 0$ and 0.4%, respectively.Solid lines are fits of the data to the ZF-μSR model in Eq. 4.1 for each temperature.

Fig. 4.3c can be found in Ref. [82]. In these measurements, the initial muon spin polarization is in the a-b plane of the crystals, and the time spectra were obtained using up and down positron counters. At high temperatures, only a very faint depolarization of the μSR signal is observed. This weak relaxation mostly originates from the interaction of the muon spin with randomly oriented nuclear magnetic moments. Upon cooling, the relaxation of the μSR signal increases due to the proliferation of Fe-spin correlations. For $x = 0$ and 0.4% samples, three distinct precession frequencies occur in the μSR spectra, which emanate from three magnetically inequivalent muon stopping sites in $NaFe_{1-x}Ni_xAs$, in agreement with the stopping site calculations presented later in Sec. 4.2.2 .

The ZF-μSR spectra were fit to the following phenomenological model:

$$\begin{aligned} P_{\mathrm{ZF}}(t) =& F\left(\sum_{j=1}^{3}\left(f_j\cos(2\pi\nu_j t+\phi)e^{-\lambda_j t}\right)+f_L e^{-\lambda_L t}\right)+ \\ & (1-F)\left(\frac{1}{3}+\frac{2}{3}\left(1-\lambda t-(\sigma t)^2\right)e^{-\lambda t-\frac{1}{2}(\sigma t)^2}\right) \end{aligned} \tag{4.1}$$

The model in Eq. 4.1 consists of an anisotropic magnetic contribution characterized by an oscillating "transverse" component and a slowly relaxing "longitudinal" component. The longitudinal component arises due to the parallel orientation of the muon spin polarization and the local magnetic field. In polycrystalline samples with randomly oriented fields this results in a so-called "one-third tail" with $f_L = \frac{1}{3}$. For single crystals, f_L varies between zero and unity as the orientation between field and polarization changes from being parallel to perpendicular. In addition to the magnetically ordered contribution, there is a paramagnetic (PM) signal

component characterized by the densely distributed network of nuclear dipolar moments σ and dilute electronic moments with random orientations λ [83]. The temperature-dependent magnetic ordering fraction F in the range $0 \leq F \leq 1$, governs the trade-off between magnetic and PM behaviors.

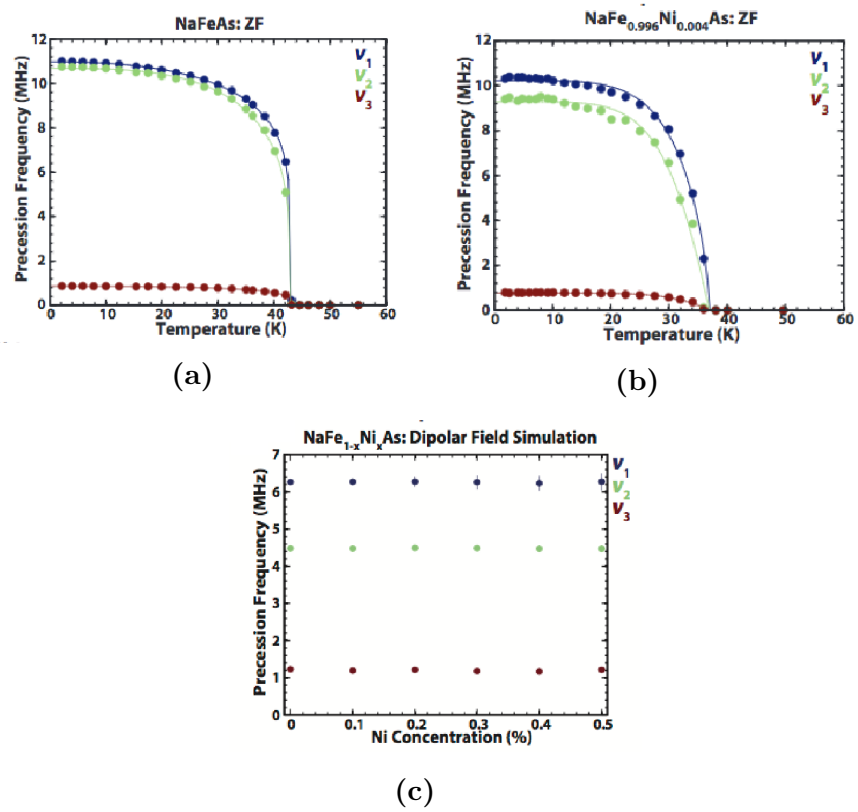

Figure 4.5: dipolar field from μSR and simulated one, Muon precession frequencies in $NaFe_{1-x}Ni_xAs$. Precession frequencies ν_j from the model used in (4.1) on the $x = 0$ and 0.4% compounds, respectively. Solid lines are power-law fits to the data. Simulation results from dipolar field calculations on lowly-doped $NaFe_{1-x}Ni_xAs$, using the three muon stopping sites obtained from DFT calculations

Shown in Figure 4.5a and 4.5b are the temperature dependence of the precession frequencies observed in the $x = 0$ and 0.4% samples. For the undoped and $x = 0.4\%$ systems, there are three distinct frequencies that share the same relationship $\nu(T) = \nu(0)(1 - (\frac{T}{T_N})^a)^b$, which are indicated by solid lines. In the parent system, a sharp step-like increase of $\nu(T)$ is observed below $T_N \approx 42$ K, which may be a signature of a first-order phase transition, although further experiments are needed to establish the character of the transition. This feature is absent in the $x = 0.4\%$ sample, which could be due to disorder effects introduced by Ni

impurities [84]. Similar ZF-μSR experiments were performed by using positron counters located in the forward and backward directions with respect to the muon beam direction. Interestingly, the two fast frequencies are absent in the non-spin-rotated spectra for $x = 0$ and 0.4%. If each frequency is associated to a different muon stopping site, these results suggest that the magnetic field directions at the high-field stopping sites are oriented along the c axis of the crystal. This feature is consistent with dipolar field simulations on muon stopping sites presented in Sec. 4.2.3.

4.2.2 DFT Calculation of Muon Stopping Sites

To investigate the effect of Ni dopants on the magnetism in $NaFe_{1-x}Ni_xAs$, I numerically simulate the behaviour of the muon in the magnetic environment of NaFeAs and $NaFe_{0.5}Ni_{0.5}As$. The $NaFe_{0.5}Ni_{0.5}As$ compound serves as a representative of the compounds with mixed Fe/Ni composition.

The DFT calculations were performed with the PBE formalism for the exchange correlation functional [30] and PAW pseudopotential [40–43]. The plane wave and charge density cutoffs used are 120 and 1080 Ry, respectively.

At low temperatures, NaFeAs crystallizes into the Cmme space group, the orthorhombic structure has lattice constants; $a = 5.6834$ Å, $b = 5.6223$ Å, and $c = 6.9063$ Å.[77]. With DFT force and energy minimization on the magnetic cell, the Fe atom is at (0.250,0.000,0.000), Na atom at (0.000,0.250,0.651) and As atom at (0.000,0.25,0.198) positions in fractional coordinate units. The atomic positions are in good agreement with experimental observed positions.[77]

Stopping site calculations and subsequent dipolar field calculations were performed on $NaFe_{1-x}Ni_xAs$ with these atomic positions. The low temperature magnetic ordered state of NaFeAs was used in the calculation with the Fe spins aligned in the collinear AFM arrangement as depicted in Fig. 4.3b. For Ni doping in $NaFe_{0.5}Ni_{0.5}As$, Fe was substituted with a non-magnetic Ni alternately along the b-axis forming an Fe-Ni stripes as for $NaFe_{0.5}Cu_{0.5}As$.[85] From the magnetic characterization plot Fig. 4.3c, magnetism is suppressed for x=0.015, however for the purpose of site calculation and understanding the effects of doping with Ni, the system was assumed to still remain in the AFM ordered state. With DFT force and energy relaxations on the doped structure, a shift away from the high symmetry positions of the Na and As atoms is observed, as the Fe-Ni stripes are formed.

To accommodate the muon impurity and AFM ordering, a $2 \times 2 \times 2$ supercell consisting of 96 Na-Fe(Ni)-As atoms was used for the calculations. The Brillouin zone was sampled on a $2 \times 2 \times 2$ Monkhorst-Pack grid [38] of k-points in the reciprocal space.

In the search for the muon stopping sites, I used the UEP and uniform grid strategy already described in Sec. 4.1 (See Figs. 4.1 and 4.2) for the starting trial

positions. 15 different trial muon positions were sampled within the supercell for NaFeAs and $NaFe_{0.5}Ni_{0.5}As$ by force and energy minimization within DFT. To accommodate for these relaxations, the forces acting on the atoms were optimized till a threshold of 10^{-3} and energies till threshold of 10^{-4} all in atomic units.

Also, I have carried out DFT+U calculations. [33–36](see Sec. 3.3) The U values used for the calculation are 3.807678 and 3.644253 eV on the Fe ions for NaFeAs and $NaFe_{0.5}Ni_{0.5}As$ respectively. I calculated the values of U using the self-consistent linear response to small perturbation method[36, 37] (see Sec. 3.3.1 and Fig. 3.2 for details). The Hubbard U correction is normally used within DFT to correctly describe correlation effects for the purpose of correct description of band behaviour and properties at and around the Fermi level. However, relaxation calculations with DFT+U, indicate that the use of Hubbard U correction has no effect on structural relaxations of the muon impurity interstitial positions in both NaFeAs and $NaFe_{0.5}Ni_{0.5}As$. Hence, the calculations for the muon site determination reported here are for those with the conventional DFT method, without the U correction.

Table 4.1: Summary of candidate muon stopping sites in NaFeAs determined by DFT. Candidate muon site cluster locations are same for $NaFe_{1-x}Ni_xAs$, with little precision changes on the positions.

Cluster	Label	No. of symmetry pos.	Site Position [a]	ΔE [b]
I	A	8n	(0.100, 0.750, 0.100)	0
I	B	8m	(0.000, 0.875, 0.100)	42
I	C	8l	(0.250, 0.500, 0.250)	183
II	D	4b	(0.750, 0.500, 0.500)	287
II	E	4g	(0.750, 0.250, 0.600)	436

[a] Site positions given in coordinates of the unit cell.
[b] DFT total energy difference with respect to site A

4.2.2.1 Candidate Muon Sites

After the force and energy convergence with the DFT minimization, the final positions of the 15 initial trial starting positions were collected and clustered considering sites with same position and DFT energy into 5 inequivalent positions that represent the plausible stopping sites for the muon in NaFeAs. The representative position for each group is shown in Table 4.1 and Fig. 4.6a. Also, the site calculations for $NaFe_{0.5}Ni_{0.5}As$ result in same plausible sites as for NaFeAs, (Table 4.1) with very little precision differences in the positions and DFT energy. This shows that for $NaFe_{0.5}Ni_{0.5}As$ the muon is expected to stop in the same inter-

stitial positions as in NaFeAs. This is assumed to be same for the other lightly Ni doped composition that were not considered in the calculations. Thus, while the doping has effect on its magnetic properties, it likely has no effect on the muon stopping sites.

The resulting positions from the DFT relaxations can be referred to as the *candidate* muon stopping sites, since absence of the muon quantum motion and nature in DFT might lead to the muon being trapped in shallow minima potential positions. I considered the corrections due to the muon light mass by taking into account the spread of the muon wave funciton within the double Born-Oppenheimer(DBO) approximation. I used the DBO approximation to examine the relative stability of the five candidate sites. Within the DBO method, a potential exploration algorithm (PEA) is used to efficiently sample the apriori unknown potential felt by the muon [56].

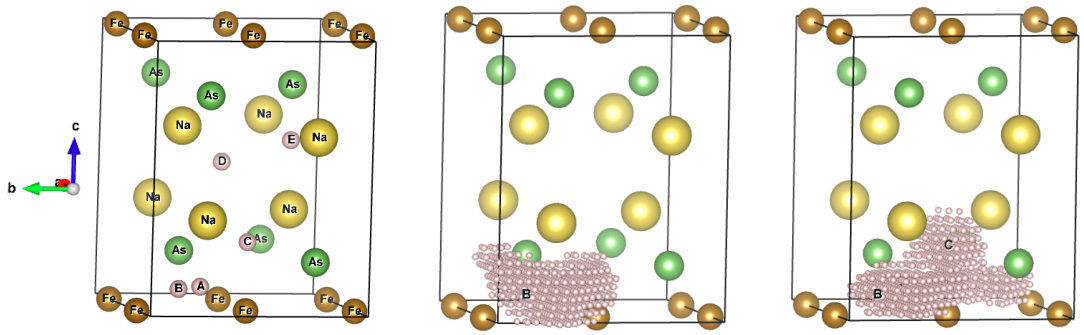

Figure 4.6: (a) Postions of the 5 candidate muon sites in the unitcell labelled A-E for the muon (pink spheres) (b) 800 different muon potential map positions by the exploration algorithm within the DBO approach starting from site B (c) 800 Muon potential map with DBO starting from site C. The potential map shows that site C relaxes into site B and A. All plots were visualized with *VESTA*.[67]

I group the five candidate sites into two clusters (Table 4.1) based on stability checks using DBO [56], which takes into account the quantum description of the muon. With the sampling of the potential, site C is observed to be a local minimum in the muon potential. site C relaxes towards sites A and B (see Fig. 4.6c), this also happens because site C has very low barrier less than 0.24 eV that is too small to bind the muon. Sites A and B are also in proximity to each other considering their positions in the lattice and the energy difference too. Consequently, I associate sites A,B, and C together as cluster I. Similarly, I also observe that sites E and

D though close in distance also relax into each other, which together form cluster II. The clustering also explains the observed frequencies, cluster I contains the low DFT energy sites that describe the high muon field observed from experiment, while cluster II contains sites that correspond to the low field.

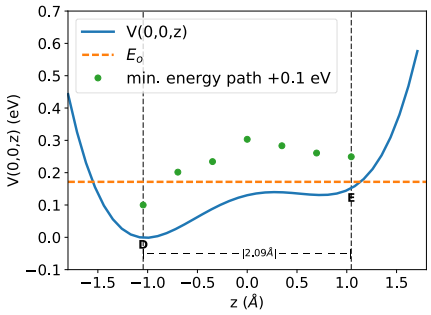

Figure 4.7: A toy model potential $V(0,0,z)$ (solid line) together with the ground state energy, E_0 from solving the Schrodinger for a muon in a potential of the form $V(x,y,z) = \frac{1}{2}a(x^2+y^2) + \frac{1}{2}b(z^4 - Z^2 + 2z) + c$. The green dashed line shows the DFT energy profile map of the path from the symmetric site D to site E. These simulations suggest that the muon is likely delocalized over the two sites in Cluster II (sites D and E).l

Shown in Fig. 4.7 are the results of further analysis of the sites in cluster II. The energy profile extracted from the DBO potential map can be represented by the toy model shown in Fig. 4.7. This enables to solve the Schrödinger equation of the muon in the trapping potential, yielding a ground state energy of 0.17 eV (independent of the interpolation method and the boundary condition, to some extent) which is greater than the barrier seen in the potential map. These findings suggest that the muon wave function for the low field sites may be delocalized over positions between sites D and E (herafter the D-E site). A a result, the low frequency detected from experiments may come from an averaging of the field at the two sites.

From our stability checks, only two of the three muon sites in the low-energy cluster proved to be stable. As a result, three plausible muon stopping locations have been determined, including two stopping sites (A,B) and a delocalized high-energy stopping position (D-E) in NaFeAs.

4.2.3 Dipolar Field Simulation

With the muon stopping sites determined, magnetic dipolar field simulations were performed by simulating the NaFeAs as a lattice of localized magnetic dipoles.

Table 4.2: Summary of dipolar field simulations in NaFeAs using muon stopping site positions obtained from DFT. Stopping site positions are given in fractional coordinates. The static ordered moments size on Fe was assumed to be $0.175\mu_B$ in the dipolar field calculations.

Site	Site Position	ν_{sim} (MHz) [a]	ν_{exp} (MHz) [b]	θ_{sim} (^{o}) [c]	θ_{exp} (^{o}) [d]
B	(0.000, 0.875, 0.100)	10.987	10.981	42.1	0
A	(0.100, 0.750, 0.100)	7.839	10.685	31.1	0
E	(0.500, 0.250, 0.600)	2.090	0.864	0.6	18
D-E	-	1.052(31)	0.864(06)	-	18(10)

[a] Muon precession frequency from dipolar field simulations
[b] Muon precession frequency from μSR experiments on NaFeAs (See Fig 4.5a)
[c] Average acute angle between the simulated field direction and the c axis
[d] The local field direction was estimated from ZF-μSR measurements with the muon spins rotated in orthogonal directions

Non-magnetic nickel impurities were randomly substituted into the Fe sites on the host NaFeAs lattice to generate $NaFe_{1-x}Ni_xAs$. By performing a vector sum of the array of (static) electronic and random nuclear dipolar moments, the internal field distribution was numerically simulated for all points in the crystal (Sec. 2.5 for details of the sum)

A $9 \times 9 \times 9$ cell of magnetic dipoles was used to model the internal field of $NaFe_{1-x}Ni_xAs$. Dipole positions and strengths for the idealized crystal structure in NaFeAs described in Sec. 4.2.2. The moments on Fe are assumed to take on a collinear AFM striped pattern, common to other Fe-HTS. To simulate the effect of doping, the magnetic Fe atoms are randomly substituted with nonmagnetic Ni atoms to achieve the desired Ni concentration x. The dipolar field at the muon site was obtained by summing over all dipoles in the $NaFe_{1-x}Ni_xAs$ supercell.

The simulated muon frequencies are related to the muon dipolar field by this relation $\nu = \gamma_\mu \mathbf{B}$ where $\gamma_\mu/2\pi = 135.538$ MHz/T, is the gyromagnetic ratio for the muon. By comparing the simulated frequencies (shown in Table 4.2) with the experimental results, the two high frequencies are associated to ν_1 and ν_2 with sites B and A, respectively. The low frequency ν_3 is identified with site E of Cluster II. A comparison between simulated and experimental results is presented in Table 4.2. However, if the muon is considered to delocalize over site D and E, the averaged simulated frequency 1.052 MHz compares well with the experimentally measured value of 0.864. Our simulations show that the experimentally observed frequency ν_1= 10.9 MHz in NaFeAs corresponds to an ordered Fe moment size of about μ_{Fe} = 0.175 μ_B. This value of the calculated Fe moment in NaFeAs is significantly more definitive and also in better agreement with the result of other techniques

compared to the earlier μSR results of 0.1-0.2 μ_B [86] and 0.10(3) μ_B [81] analyzed by different approaches, thanks to the more precise DFT method of determining the muon implantation sites.

4.2.4 Discussion

The stopping site calculations and stability analysis reveal three plausible muon stopping sites in NaFeAs. This is consistent with the observation that there are three precession frequencies in the ZF-μSR spectra in lightly doped $NaFe_{1-x}Ni_xAs$. The calculated precession frequencies are listed in Table 4.2, along with the extrapolated frequencies from power law fits of the frequencies from μSR found in Fig. 4.5. Moreover, the dipolar simulations show that the mean local fields at the two high-field sites make an acute angle of approximately 36^o with the crystal c axis, implying that the strong fields at these sites are preferentially aligned with the c axis. This is consistent with the experimental observation that the high frequency oscillations have noticeable amplitudes when the initial muon spin is not aligned with the c axis (i.e., in the spin-rotated configuration), as shown in Fig. 4.4a. Differences in the simulated and experimentally-obtained angles θ suggest that the true muon sites are likely at a small displacement from the ones listed in Table 4.2.

The doping evolution of the simulated precession frequencies are shown in Fig. 4.5b. By comparisons of the simulated and observed frequencies for Site B, the dipolar field simulation allows to estimate the ordered moment size of the Fe atoms in NaFeAs to be $\mu_{Fe} = 0.175\ \mu_B$. This moment size was used in the dipolar simulation at other sites. The difference between the simulated and experimental frequencies for the second and third sites suggests that there are contact hyperfine fields contributions to the internal field, which are not present in the dipolar model. Nonetheless, our computational investigation provides a physical interpretation of the frequencies observed in the ZF-μSR spectra and corroborates the model for the magnetic ordering in Ref. [68].

The ordered moment size in a variety of Fe-HTS has been explored experimentally using μSR, neutron scattering, and Mössbauer measurements.[95] The reported variations of the ordered Fe moments of the same specimen testifies to the differences in sensitivity across these three probes of the local moment. Table 4.3 shows a comparison of the ordered moment size of representative systems from the various classes of Fe-HTS. The estimated moment size of $\mu_{Fe} = 0.175\ \mu_B$ for NaFeAs, is consistent with the moment sizes reported from neutron scattering [87] and Mössbauer spectroscopy.[88]

Table 4.3: Comparison of the low-temperature Fe ordered magnetic moments in selected Fe-HTS. All magnetic moments are given in units of μ_B

Fe-HTS	μSR	Neutron Scattering	Mössbauer (MHz) [a]
NaFeAs	0.175	0.17[87]	0.158[88]
$BaFe_2As_2$	0.75[89]	0.87[90]	0.36[91]
LaFeAsO	0.68[47]	0.63[92]	0.34[93]
$FeSe_{0.98}$ [b]	0.20(5)[50]	undetected	0.18(1)[94]

[a] Ordered moment extrapolated from measured low-temperature hyperfine field using the scaling relation 15 T/μ_B[95]

[b] μSR moment is taken under 2.4 GPa pressure . No magnetic Bragg peaks for neutron scattering.[50] Mössbauer moment is for FeSe under 2.5 GPa pressure

4.2.5 Conclusion

In conclusion, I presented the μSR measurements, showing coexistence of magnetism and superconductivity in $NaFe_{1-x}Ni_xAs$. To explain the three precession frequency from μSR measurement and the size of the ordered moment with μSR. I carried out DFT calculations to predict the implantation site of the muon together with dipolar field simulations. DFT muon site calculations on NaFeAs and $NaFe_{0.5}Ni_{0.5}As$ show that the muon occupy same position in both materials in the AFM ordered state. This suggests that light doping of NaFeAs with Ni even though has effect on the magnetic fraction, is likely not to affect the site muon implantation in the AFM ordered state. Also, NaFeAs is one of the compounds where considering corrections on electronic correlations within DFT+U do not alter the atomic equilibrium positions in the structural relaxations and as such the determined muon implantation sites do not change with the Hubbard U corrections. With dipolar simulations and comparison with the measured muon precession frequency, the calculated muon sites gives the ordered moment size of $\mu_{Fe} = 0.175\ \mu_B$ for NaFeAs in the AFM ordered state.

4.3 Magnetic order transition under pressure in $Yb_2Pd_2In_{1-x}Sn_x$: Prediction with muon

In this section, I continue to use the ab-initio strategy described in Sec. 4.1 for the calculation of muon site in $Yb_2Pd_2In_{1-x}Sn_x$ together with dipolar field calculations and magnetic structure determination methods to understand and explain the source of the large changes in the observed muon local field under pressure in $Yb_2Pd_2In_{1-x}Sn_x$. However, before discussing the site calculation and comparison with μSR measured local field, I will first present the details of the μSR measurements.

$Yb_2Pd_2In_{1-x}Sn_x$ as well as other Ytterbium (Yb) based heavy fermion (HF) metallic and ternary systems are of interest because of the intriguing properties that results due to the interplay between the Kondo and Ruderman-Kittel-Kasuya-Yoshida (RKKY) interactions.[96–101] These interesting properties are due to the relevant roles played by the 4f manifold of the Yb ions and its interactions with the conduction d electrons of the transition metals.[102–104] Chemical doping and/or application of pressure allows control of these interaction effects, thus giving birth to new interesting properties. Quantum critical points driven by application of pressure has been reported in Ref. [98] for Yb_2Pd_2Sn. In the competition between the Kondo interaction J_K and RKKY exchange J_{ij}, the non-magnetic Kondo effect induced state occurs if the J_K is very large compared to J_{ij} and the AFM state occurs if J_{ij} is larger.[101] Both Yb_2Pd_2In and Yb_2Pd_2Sn are non magnetic [100] at the ground state. However, with doping and application of pressure the non-magnetic Yb^{2+} ($4f^{14}$) goes to the magnetic Yb^{3+} ($4f^{13}$). These changes are due to the increase in the number of 4f holes. In $Yb_2Pd_2In_{1-x}Sn_x$ a robust antiferromagnetic phase develops by varying either the In/Sn concentration or the external pressure, since both increase the RKKY exchange interaction with respect to the Kondo one. [99, 101, 105, 106] The ternary systems normally find application in optical sensors, magnetocaloric effect for refrigeration near room temperature and in memory storage.[107–110]

4.3.1 μSR-pressure measurements

Yb_2Pd_2In compound develops a low temperature long range magnetic order when doped through In-Sn substitution for Sn contents in the range 0.3 to 0.9. [96–98] To understand the effect of pressure on the magnetic ordering on the Sn doped sampled, we have performed μSR experiment under hydrostatic pressure on $Yb_2Pd_2In_{1-x}Sn_x$ (for x =0, 0.3, 0.6 and 0.8).

Series of $Yb_2Pd_2In_{1-x}Sn_x$ polycrystalline samples with x =0, 0.3, 0.6 and 0.8 were prepared from stoichiometric amounts of pure elements by high frequency,

melting the constituent materials in a closed tantalum crucible. To ensure phase purity, subsequent heat treatment at 120 K was carried out on the samples for 1 week. All the compounds in the series crystallize with the D^5_{4h} tetragonal space group with the 4h site occupied by Yb ions at the low mm symmetry point.

μSR measurements on $Yb_2Pd_2In_{1-x}Sn_x$ were performed at the SμS muon source at the Paul Scherrer Institut (PSI) Villigen, Switzerland under zero external magnetic field (ZF) with temperatures ranging from 0.2 up to 15 K. Dolly and LTF spectrometer (πE1 and πM3 beam lines) were used to carry out low-background measurements at ambient pressure as references for the experiments performed on both GPD and HAL9500 spectrometers (μE1 and πE3 beam lines) for μSR measurements as a function of external pressures up to 25 kbar and applied magnetic field up to 8 T, respectively.

In the following paragraphs we will focus on μSR measurements at GPD facility. The external pressure was applied by confining the sample in a double-wall piston-cylinder pressure cell (PC) made of MP35N alloy while Daphne oil 7373 was used as transmitting medium to assure nearly hydrostatic pressure conditions in the whole experimental range.[111, 112] In order to determine the exact pressure inside the cell at low temperature, we measured the pressure-dependent shift of the superconducting transition temperature of a small piece of Indium (In) placed near the sample in the PC. Small quantity of In was used, such that its contribution to the μSR background is negligible. An AC susceptometer was used to detect the shift of Indium's T_c with the applied pressure.[111, 112]

The normalized ZF-μSR polarization of $Yb_2Pd_2In_{1-x}Sn_x$ for $x = 0$ is shown

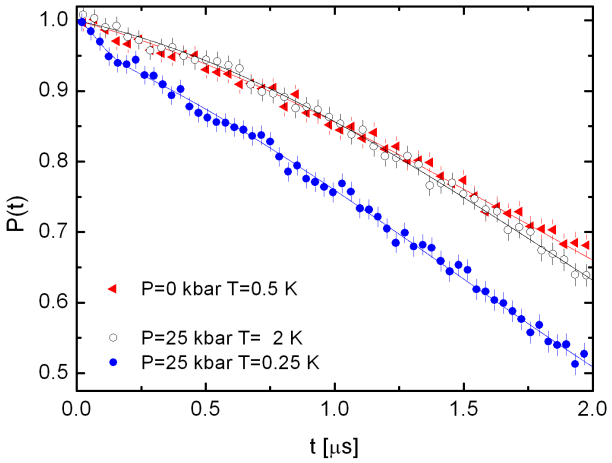

Figure 4.8: The normalized ZF-μSR polarization of $Yb_2Pd_2In_{1-x}Sn_x$ for x=0 sample as functions of temperature (T) and pressure (P). A tiny depolarization is seen only at short times in the last case.

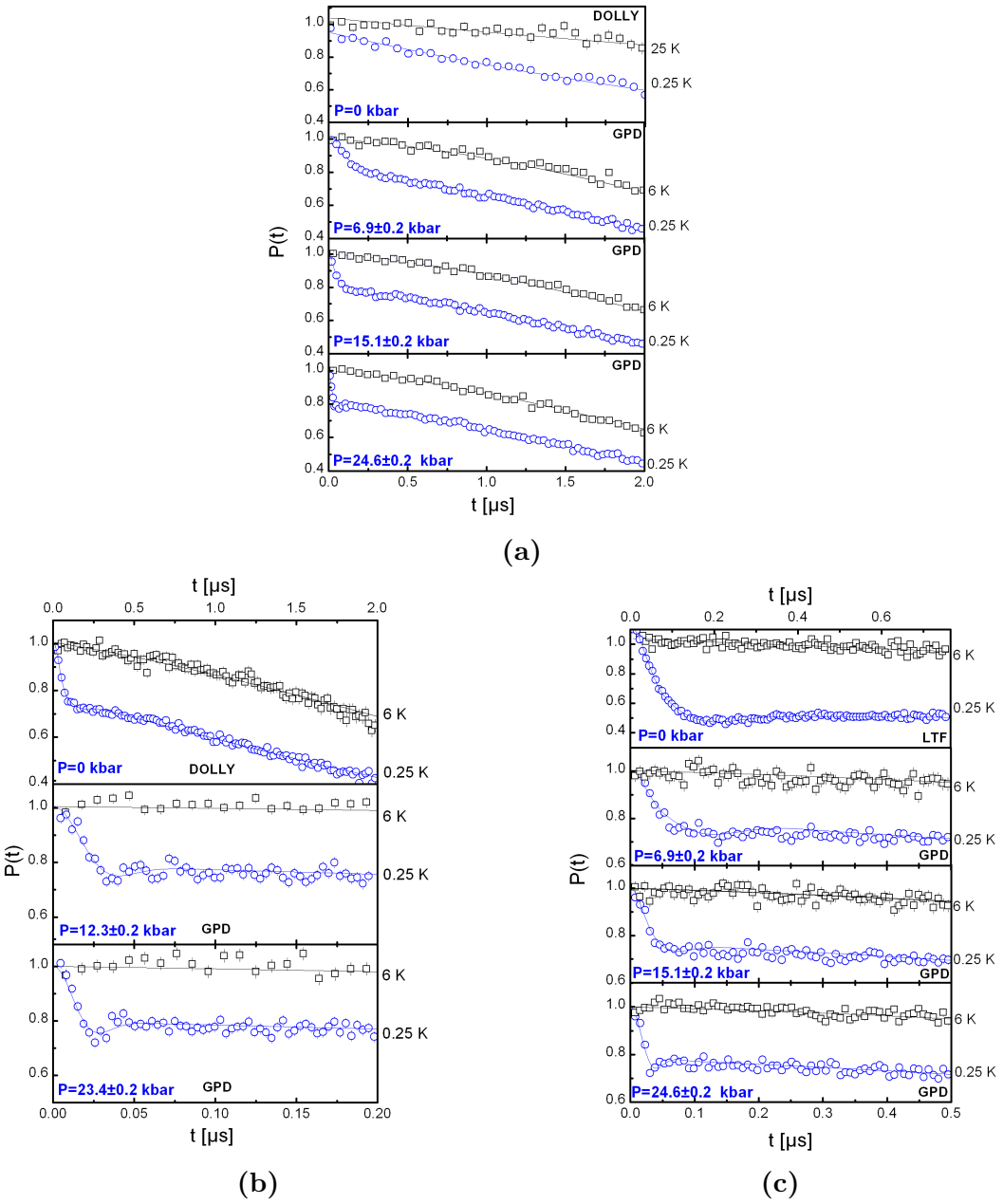

Figure 4.9: The normalized ZF-μSR polarization of $Yb_2Pd_2In_{1-x}Sn_x$ for; (a) $x = 0.3$ (b) $x = 0.6$ and (c) $x = 0.8$ as functions of pressure and temperature.

in Fig. 4.8 where a tiny depolarization is observed only at short times for pressure (P) = 25 kbar and at the lowest temperature (T=0.25 K). In Fig. 4.9 the ZF-Polarization at short times for $x = 0.3$, 0.6 and 0.8 are shown for selected tem-

peratures and pressures. The depolarization plots generally show highly damped coherent oscillations that develops by both increasing Sn doping or applied external pressure. To determine and remove the contribution from the pressure cell (PC), the time dependent muon spin depolarization was fitted with the following model;

$$P(t) = \frac{A^{\mathrm{ZF}}(t)}{A^{\mathrm{ZF}}_{\mathrm{tot}}(0)} = a_{bk}\, g(t) + [1 - a_{bk}] \cdot \{a_T\, f(\gamma_\mu B_\mu t)\, D_T(t) + a_L\, D_L(t)\}\,, \qquad (4.2)$$

where $A^{\mathrm{ZF}}_{\mathrm{tot}}(0)$ is the high-temperature value of the initial asymmetry and a_{bk} accounts for the fraction of incoming μ^+ stopping outside the sample volume. For this coefficient we can distinguish three cases: a) it is almost zero during the reference experiments performed at the low-background Dolly spectrometer (x=0.3 and 0.6 samples); 2) it represents the fraction of μ^+ implanted in Ag sample holder during LTF measurements (x=0.8 sample). In such a case we fixed $g(t) = e^{(-\lambda_{Ag} t)}$ where both a_{bk} and λ_{Ag} where determined at the lowest temperature and kept fixed during the subsequent fitting of the experimental data[3]. 3) In the GPD measurements a_{bk} accounts for the fraction of muons implanted in the PC. In such a case, $g(t)$ represents the Gaussian Kubo-Toyabe function (see Eq. 2.13).[4] The coherent muon precession in the magnetically ordered phase is taken into account by $f(t)$ using a cosine function, whereas $D_T(t) = e^{-\frac{\sigma_T t^2}{2}}$ and $D_L(t) = e^{-\lambda_L t}$ were used to account for relaxation in the precession. The former decay reflects the static distribution of local magnetic fields, whereas the latter is due to dynamical relaxation processes. B_μ is the field at the implantation site and $\gamma_\mu = 2\pi \times 135.53\,\mathrm{MHz/T}$ is the muon gyromagnetic ratio, while a_T and a_L refer to muons probing local magnetic fields in the transverse (T) or longitudinal (L) directions with respect to the initial spin polarization. In the following paragraphs we will detail these parameters for each sample.

In Fig. 4.8, for $x = 0$ i.e the Yb_2Pd_2In sample, the polarization was fitted by one Gaussian exponential decay at both (p, T)=(0 bar,0.5 K) and (p, T)=(25 kbar, 2 K) as signature of randomly oriented nuclear dipolar fields. At this very pressure, a small transverse component rises up at T=0.25 K. This means that roughly 15% of the sample develops a short range magnetic order suggesting that at this pressure the system is likely on the verge of a quantum criticality.

[3]The background contribution from the Ag sample holder (Ag plate No. 233) was determined by a transverse field experiment (H=30 Oe) at 20 mK. $a_{bk} \sim 0.25$ and $\lambda_{Ag} = (0.0158 \pm 0.009)\ \mu s^{-1}$.

[4]$a_{bk} \approx 65\%$ was determined by a transverse field run at high temperature ($T > T_N$)). The Gaussian depolarization rate σ_{bkG} was determined by fitting the asymmetry at longer time when the depolarization rate due to PC dominates. These two parameters were therefore kept fixed in the subsequent fitting iterations.

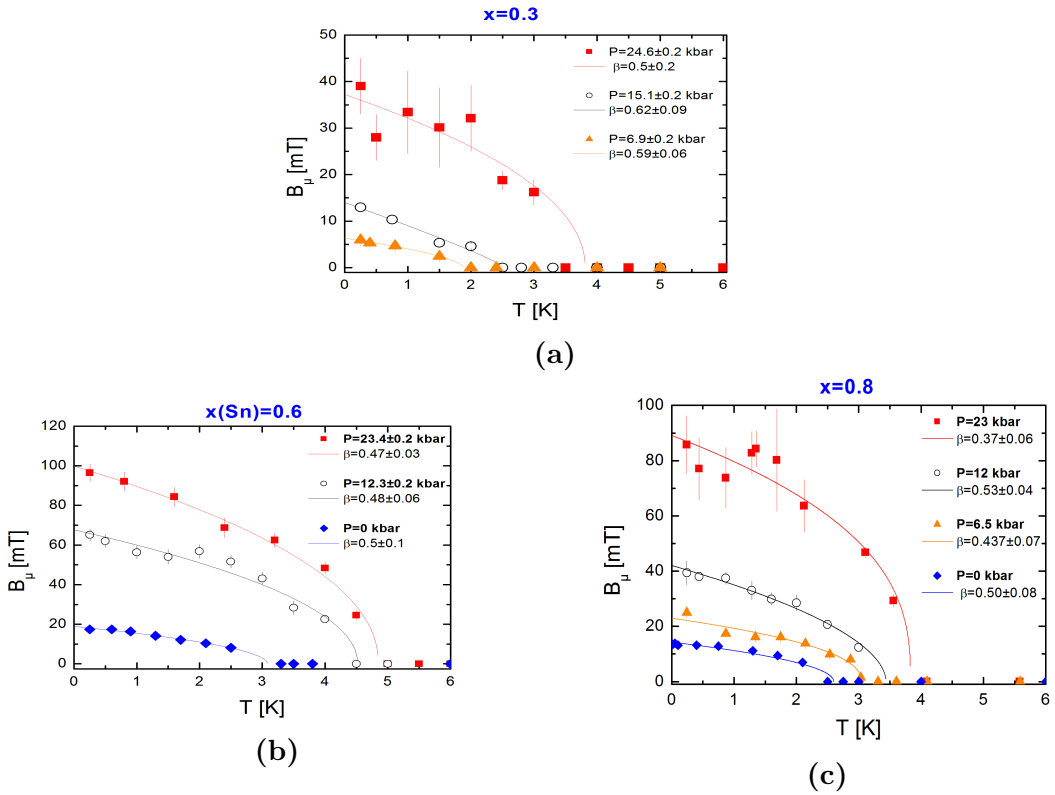

Figure 4.10: The internal field B_μ as probed by implanted muons at different applied pressure for (a)x=0.3 , (b) 0.6 and (c) 0.8 samples.

For $Yb_2Pd_2In_{0.7}Sn_{0.3}$ sample, at ambient pressure, the low background data taken at Dolly (Fig. 4.9a) at T= 25 K is well fitted by a single Gaussian depolarization due to randomly oriented nuclear dipolar fields. At the lowest temperature only a small depolarization appears suggesting that also in this case, the system is likely at the verge of a quantum criticality at ambient pressure. Interestingly, increasing the applied pressure to 12.3 and 23.4 kbar, a strongly damped oscillation is observed at 0.25 K. In this case the fitting function relative to the sample contribution was built up by two transverse component one of which with a cosine term whereas the corresponding two longitudinal ones merged in one single Lorentzian decay. It is worth to note that the frequency of the oscillating part increases rapidly with increasing pressure.

For $Yb_2Pd_2In_{0.4}Sn_{0.6}$ sample, at ambient pressure, the low background data taken at Dolly (Fig. 4.9b) at T= 0.25 K is well fitted by one transverse component consisting in a Gaussian damped cosine and one single Lorentzian decay. The same fitting function was successfully adopted for the measurements under pressure. Also in this case we note an abrupt increase of the precession frequency with

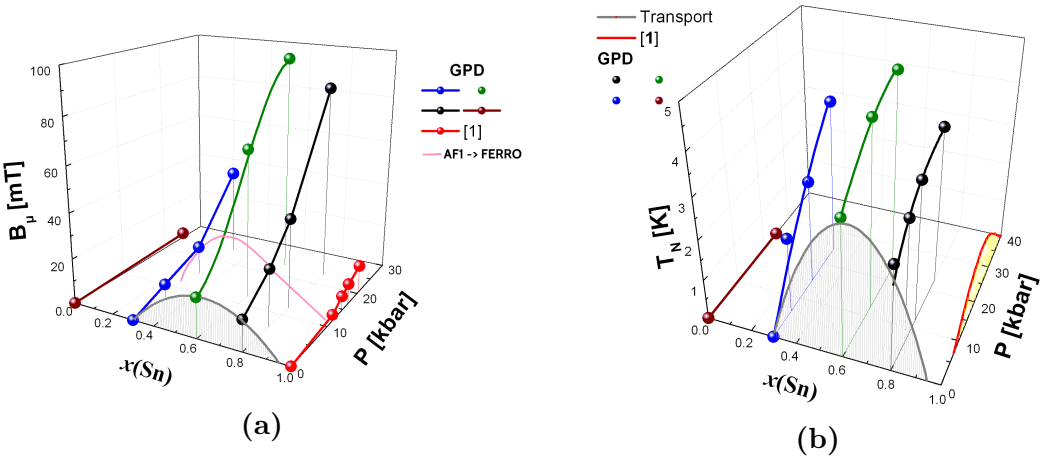

Figure 4.11: Summary plot: (a) P-B_μ-x (b) the P-T-x diagrams

increasing applied pressure.

For $Yb_2Pd_2In_{0.2}Sn_{0.8}$ sample, at ambient pressure, the low background data taken at LTF (Fig. 4.9c) at T= 25 K is well fitted by a single Gaussian depolarization due to randomly oriented nuclear dipolar fields for $T > T_N$. At the lowest temperature, the damped oscillation was fitted by two transverse component one of which is a Gaussian damped cosine term and whereas the corresponding longitudinal signals were merged in one single Lorentzian decay. In the GPD run the same fitting function was adopted for the sample component of the polarization function. Also, the frequency of the oscillating part increases rapidly with increasing pressure.

Fig. 4.10 represents the summary of the evolution of B_μ as a function of temperature for all values of the applied pressure. Fig. 4.11 summarizes the variation of the internal field B_μ and of the Néel temperature as a function of both In-Sn substitution and the applied pressure. The μSR measurements and also measurements already reported in Ref. [98] for Yb_2Pd_2Sn were included for completeness of the phase diagram. A general steep increase of the local magnetic field for all the tested samples is observed. In particular, in the $x = 0.6$ case, it rises up to 10 times to that of the ambient pressure value. In order to understand the effect of pressure on the magnetic order and account for the steep increase in the local magnetic field at the muon, the muon implantation site has to be determined.

4.3.2 Calculation of muon implantation site in Yb_2Pd_2In

To determine the implantation site of the muon in $Yb_2Pd_2In_{1-x}Sn_x$, I have carried our DFT calculations with the third strategy for initializing the search for the muon position described in Sec. 4.1. The electrostatic potential was calculated in

the unitcell of Yb_2Pd_2Sn, while the resulting minimum positions are used as trial starting positions for the muon impurity in the Yb_2Pd_2Sn supercell and then the forces and energy are minimized.

$Yb_2Pd_2In_{1-x}Sn_x$ crystallizes in the tetragonal crystal structure with space group P4/mbm. The lattice parameters are a = b = 7.5780 Å and c = 3.6350 Å with Yb on the 4h Wyckoff position at (0.1724, 0.6724, 0.5000), Pd with 4g at (0.3716, 0.8716 , 0.0000) and Sn with 2a at (0.0000, 0.0000, 0.0000). The above crystal positions were used for the DFT calculations.

The electrostatic potential was calculated for the non-magnetic Yb_2Pd_2Sn unitcell and the positions of the potential minima as shown in the isosurface plot, Fig. 4.12a were used as the starting position for the muon in the DFT relaxation. The four minima positions of the potential correspond to symmetry equivalent positions within the P4/mbm space group, thus only one starting position of the muon was considered at this level.

The muon was introduced as a hydrogen impurity at the potential minima position in a non-magnetic 160 atoms 2×2×4 supercell of both Yb_2Pd_2Sn and $Yb_2Pd_2In_{0.25}Sn_{0.75}$ with random In/Sn placement. High values of x(Sn) concentration were considered since the interest is to understand pressure effects in this range. Plane-wave DFT was used for the structural relaxations, with the GGA treatment of the exchange correlation functional within the PBE formalism [30]. For Yb and Pd atoms, the core wavefunction was approximated with the PAW method [43, 113] while for In, Sn and H the core wavefunction were approximated by the Ultrasoft pseudopotential formalism [114, 115]. The choice of the core treatement in the pseudopotential approach for each atom is justified to allow proper treatment of the localization of the f and d electrons with the PAW method and soft cutoffs within covergence limits with the Ultrasofts for In, Sn and H. 75 Ry and 750 Ry were used for the plane wave and charge density cutoffs following the reproducibility and convergence efficiency data[5] for each pseudopotential type [116, 117]. For the supercells, the Brillouin zone integration was at the gamma point. The force and total energy were minimized till threshold of 10^{-3} Ry/a.u and 10^{-4} Ry respectively.

The relaxed position for the muon is shown in Fig. 4.12b. It is worth to note that the relaxed positions are same for both $Yb_2Pd_2In_{0.25}Sn_{0.75}$ and Yb_2Pd_2Sn. This suggests that there exist little or no effect of In/Sn doping on the site of implantation of the muon. The relaxed positions are also similar to the minima potential position with little distortion (see Figs. 4.12a and 4.12b).

The 4 muon positions shown in Fig. 4.12b are symmetry equivalent positions with small distance of 0.6 Å between them. To a first approximation, we assume

[5]The data can be found in https://www.materialscloud.org/discover/sssp/table/efficiency

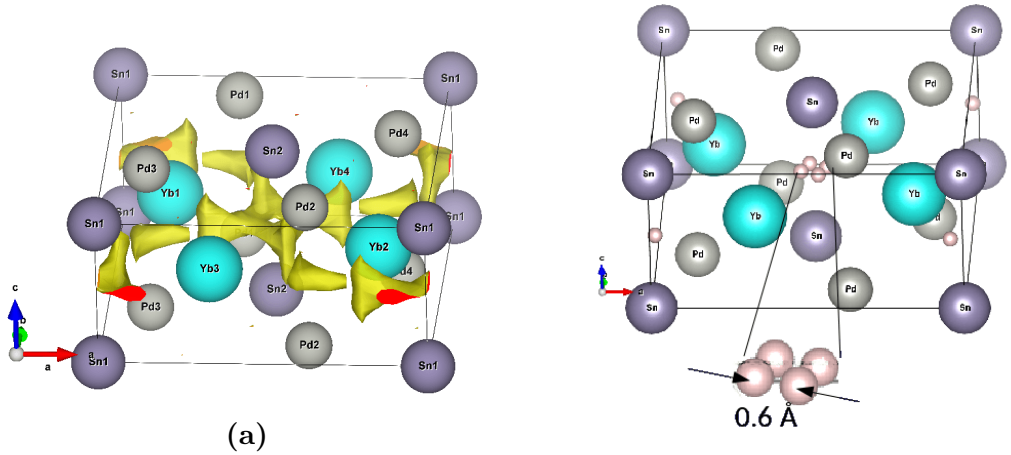

(a) (b)

Figure 4.12: (a) Muon-stopping sites: minima of the electrostatic potential (b) and the same obtained from a self-consistent DFT calculation with μ refined.

the muon position is delocalized over the 4 equivalent symmetry positions, such that the effect of the muon is an averaged effects at the 4 equivalent positions.

Since we now have the implantation site of the muon, we further explore the dipolar field at the muon to allow us understand the source of the pressure induced increase in the local field at the muon implantation site. In order, to do this, we assume that the applied hydrostatic pressure only slightly distorts the implantation site of the muon, such that the muon still remains delocalized very close to the 4 symmetry equivalent positions shown in Fig. 4.12b.

4.3.3 Magnetic order and Dipolar Simulations

The dipole sum (see Sec. 2.5) at the muon implantation site was performed at different possible allowed magnetic ordering within the P4/mbm space group. At, pressure (P) = 0, the ordered Yb was determined by neutron scattering. It's value is in the range of 0.5 - 1 μ_B for x(Sn)=0.5 - 0.9. The refined magnetic structure[6] suggests that the Yb moment points towards the centres of the square defined by their positions. However, with applied pressure above 10 kbar, the local field at the muon increases steeply from those at low and 0 pressure (see Figs. 4.10 and 4.11). To explain this we considered the dipolar simulations at all the symmetry allowed magnetic ordering of $Yb_2Pd_2In_{1-x}Sn_x$.

$Yb_2Pd_2In_{1-x}Sn_x$ has the tetragonal crystal structure of the space group P4/mbm. And with the superspace formalism[118] for the description of the magnetic symme-

[6]Paper under preparation

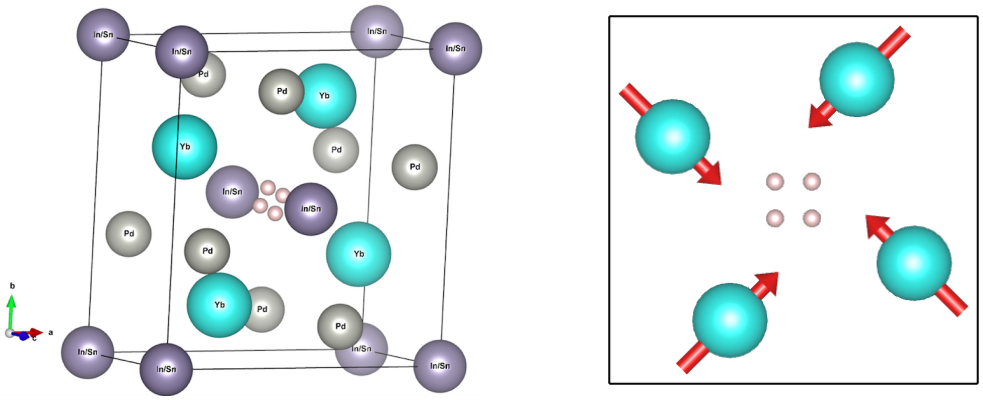

(a) **(b)**

Figure 4.13: (a) The $Yb_2Pd_2In_{1-x}Sn_x$ unit cell (b) The magnetic structure as derived from neutron scattering.[100]

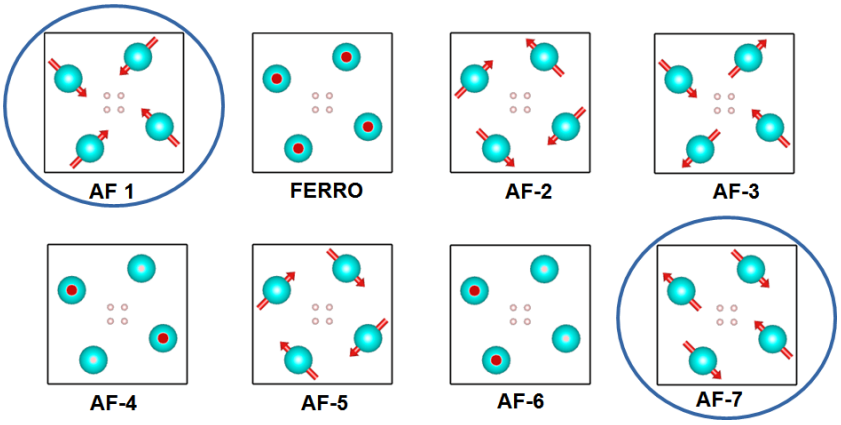

Figure 4.14: AF-1 is the Yb magnetic moment configuration resulting from neutron scattering refinement. This magnetic sublattice is in accord with B_μ values determined at ambient pressure. AF-7 is the unique AF Yb-moments configuration that is able to justify the B_μ high values found at high pressure.

try in a space group implemented in the MAXMAGN programme[119] of the Bilbao Crystallographic Server database [120], 8 irreducible representations (IRs) for the Yb-site 4h ions were found with the magnetic propagation vector k=(0,0,0.5). The 8 possible magnetic ordering from these IRs are shown in Fig. 4.14. The IRs are consistent with those calculated using the induction formula of the Basireps programme[121] in the FullProf Suite of codes.

The dipolar fields were calculated for each of the 4 equivalent muon sites in a 100×100×100 supercell of $Yb_2Pd_2In_{1-x}Sn_x$, with moment size of 1 μ_B , propaga-

tion vector k=(0,0,0.5) and for all the 8 magnetic order in Fig. 4.14. Also, since the moment is only on the Yb ions, the In/Sn concentration has negligible influence on the resulting dipolar sums. The resulting dipolar field at the muon implantation site, is an average of the field at the four symmetry equivalent positions. This is because if the muon is delocalized over the 4 positions, then it is possible to average the muon local field B_μ over the muon wavefunction ϕ_μ such that;

$$\langle B_\mu \rangle = \langle \phi_\mu | \, B \, | \phi_\mu \rangle \approx \sum_{i=1}^{4} B_i$$

We know from neutron scattering [100] that AF-1 is the correct ordering at P=0 for $x(\mathrm{Sn}) = 0.5, 0.6, 0.9$. The agreement between the calculated dipolar contribution and the experimental value at low pressure does confirm that the Fermi contact contribution to the total field probed by the implanted muons is expected to be negligible. From the averaged dipolar field sums, all the AF configurations labeled AF-1 to 6 in Fig. 4.14 induce very low fields at the implantation sites in full agreement with the results obtained at ambient pressure for x=0.6 and 0.8 compounds (see Fig. 4.11a). However when the muon is at the exact high symmetry site with AF 1-6 magnetic configuration, the B_μ averages to zero.

More importantly, the major interest is to explain the measured muon field at P > 10 kbar in Fig. 4.11a for $0.3 \leq x \leq 1$. At this pressure, the measured local field is in the range between 80 mT and 250 mT. The average dipolar sum for the Ferro and AF-7 Yb moment ordering (see Fig. 4.14) is 1041.1 mT and 520 mT respectively. AF-7 moment ordering is a sort of a ferri magnetic ordering. The dipolar field at the AF-7 configuration gives values in good agreement with the measured local field of 80 mT and 250 mT suggesting a possible reordering of Yb magnetic moments at high pressures above ≈10 kbar. Recent (unpublished) results obtained by neutron diffraction at low temperature and synchrotron x-ray diffraction at T=300 K under pressure suggest that no changes in the magnetic and crystalline structure are evident up to 10 kbar. This nicely explains the huge slope change in B_μ at high pressures.

4.3.4 Conclusion

The muon implantation site has been successfully determined in $Yb_2Pd_2In_{1-x}Sn_x$, with the muon delocalized over 4 equivalent positions that are located closed to the center of the tetragonal cell. The results of the calculated muon site and dipolar field calculations suggest a reordering of the Yb magnetic moment in the Sn doped Yb_2Pd_2In under hydrostatic pressure (P) > 10 kbar. The predicted moment reordering explains the observed steep increase in muon local field when large pressure is applied to $Yb_2Pd_2In_{1-x}Sn_x$ for $0.3 \leq x \leq 0.8$.

4.4 Muon induced effects in Sr_2RuO_4

μSR has been widely used and recorded a tremendous amount of success in probing length scales, order parameter, vortex lattice states, coherence length, penetration depth, symmetry breaking and spontaneous fields in superconductors particularly in Sr_2RuO_4[122–125]. However, a very important aspect in measurement with the muon, is to estimate the extent the implanted muon distorts the lattice and then understand what are the effects and roles of these distortions on the measured properties. It is always important to check and understand if the subtle measured physical properties of the system are of the muon and not necessarily an intrinsic property of the sample studied. This is especially needed when such subtle physical attributes of the system are not detected in measurements with other probe methods even though in many cases with μSR due to the properties of the muon and *fine* time resolution window in the experimental technique, properties like small moment magnetism not detected with other methods are possible with μSR. For example the modification of crystal field levels observed in Pyrochlores with μSR is an aftermath of the muon effect.[64] In this section, with DFT methods and the strategy for muon identification discussed in Sec. 4.1, the implantation site of the muon in Sr_2RuO_4 is calculated, while understanding the extent of the lattice distortion due to the muon. I further studied the muon effects on the lattice and on the physical properties of Sr_2RuO_4 by comparing the electronic properties and density of states distribution with and without the muon induced distortion. The aim of studying the muon induced effects effects on Sr_2RuO_4 is to understand if the spontaneous magnetization measured with μSR and not with other scanning probe methods is an aftermath of the muon.

Sr_2RuO_4 is the first known layered perovskite where unconventional superconductivity has been discovered without copper. It's discovery in 1994[126] has motivated a lot of experimental and theoretical study to understand the mechanism that drives superconductivity. Even though Sr_2RuO_4 is isostructural to the cuprates HTS, there is huge difference in its T_c of $0.93K$[126] or 1.45 K and 1.5 K for highly pure sample of Sr_2RuO_4 [123, 127] when compared to T_c approximately 100 K for the HTS cuprates. Thus, the complete understanding of the mechanism that drives superconductivity is crucial and till date, there are still a lot of challenges coupled with discrepancies in different probe methods to allow full understanding of the superconducting mechanism in Sr_2RuO_4. [122, 128]

In the early years subsequent to the discovery of Sr_2RuO_4 as a superconductor, first attempts by theoretical methods to explain the superconducting mechanism includes that the superconducting state results from strong Hund's coupling and ferromagnetic fluctuations that lead to the uncommon pairing of the Ru moments in the spin triplet state[129, 130]. These strong correlations favours Cooper pairs ordering in a p-wave symmetry with a nodeless p-wave gap [131, 132] because

of the instability expected of the weak coupling p-wave superconductivity. Furthermore, these theoretical predictions have been confirmed by experimental techniques where odd-parity pairing has been observed by phase sensitive measurements [133] and NMR Knight Shift measurements[134] that confirm the triplet state pairing of the Cooper pairs.[127, 135–137] However, recent theoretical and experimental studies[138–141] have suggested an entangled spin-orbit effect that cannot be used separately to explain the Cooper pairing in Sr_2RuO_4. The superconducting order parameter in Sr_2RuO_4 are also dependent on the orbital degrees of freedom. This is such that spin-orbit coupling leads to a momentum dependence of the Fermi surface. Also, they have argued that the Hund's splitting depends not only on the effects of the crystal field but also on those of the spin-orbit induced band splitting. They suggested that a new spin-orbital state is needed to explain the superconducting order parameter and not the singlet and triplet terminology.

Furthermore, μSR experiment [123] and high resolution polar Kerr effect [136] have detected onset of spontaneous magnetization in Sr_2RuO_4, which has been interpreted as the existence of time reversal symmetry breaking (TRSB) on entering into the superconducting states. This observed TRSB supports a chiral $(p_x \pm ip_y)$ p-wave of the order parameter. However, these spontaneous superconductivity-related magnetization and spontaneous supercurrents which are evidence of TRSB, have not been observed by other scanning probe methods.[142–144]

TRSB has also been observed with μSR by doping Sr_2RuO_4 with non-magnetic impurities, which also change the T_c [124, 145], the order parameter under application of axial strain greater than 1 gigapascal has an even parity with increased $T_c = 3.4$ K.[146, 147].

μSR has always been used to search for spontaneous internal magnetization in superconductors. With μSR, spontaneous internal field has been measured in UPt_3,[148] UBe_{13} and $ThBe_{13}$[149], but not in the d-wave paired HTS cuprates [150]. Since spontaneous magnetization has been found in some superconductors and not in the HTS cuprates, it is believed [123] that the measured spontaneous magnetization in Sr_2RuO_4 is not a muon induced effect. However, considering that other scanning probe methods do not detect the TRSB, a quantitative understanding of the measured μSR signal and any possible effects of the muon impurity on the signal are crucial to understanding the origin and extent of the TRSB. To this end, the starting point is determining the implantation site of the muon.

4.4.1 Muon implantation site and local distortions: DFT calculation

In order to understand and analyze the muon impurity induced effect in Sr_2RuO_4 sample, DFT calculations have been carried out to first determine the site of im-

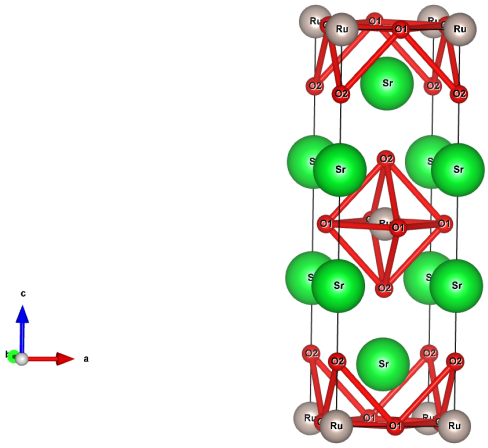

Figure 4.15: The unitcell structure of Sr_2RuO_4. The plot was visualized with *VESTA*.[67]

plantation of the muon and then investigate the muon induced distortions. As already discussed in Sec. 4.1, the positive muons were modelled as a hydrogen impurity with the periodic plane-wave DFT. The GGA was used to treat the exchange correlation functional within the Perdew-Burke Ernzerhof (PBE)[30] formalism. The potential at the core were approximated using the optimized Norm-Conserving Vanderbilt (ONCV)[151] pseudopotential for Ru atoms and ultrasoft [114, 115] pseudopotential for the Sr and O atoms. The pseudopotential choices were made to allow for correct description of the 4d behaviour in Ru and allow convergence of the self-consistent iteration. The cut-off for the plane waves and the charge density used are 70 Ry and 700 Ry respectively.

The calculations were carried out for layered perovskite structured Sr_2RuO_4 with the I4/mmm space group. The structure of Sr_2RuO_4 is such that O_4 atoms form an octahedral at the centre of a cube defined by Sr_2 at the corners while the Ru cation is at the center of the octahedral (see Fig. 4.15). The unit cell has lattice parameters a=b= 3.871 Å and c = 12.702 Å with Sr atoms occupying the 4e Wyckoff positions at (0, 0, 0.3538), Ru atoms with 2a at (0.0, 0.0, 0.0), one of the oxygen atoms (O1) with 4c at (0.0, 0.5, 0.0) and the other (O2) with 4e at (0.0, 0.0, 0.1630) in fractional coordinate units.

The trial starting positions for the muon are grid of uniform positions reduced by Sr_2RuO_4 space group symmetry to 24 inequivalent starting positions. Each of the trial starting muon position was modelled in a 126 atoms 3×3×1 supercell. A 3x3x3 Monkhorst-Pack grid of k-points was used for the Brillouin zone sampling in the reciprocal space. The paramagnetic order was considered for the magnetic ions in the calculations. The atomic relaxations through force and energy minimization were performed with the threshold for the forces and total energy set to 10^{-3}

Ry/a.u and 10^{-4} Ry respectively. During the relaxations, it is assumed that the muon does not alter the supercell volume, which is kept fixed, while all the atoms are allowed to relax.

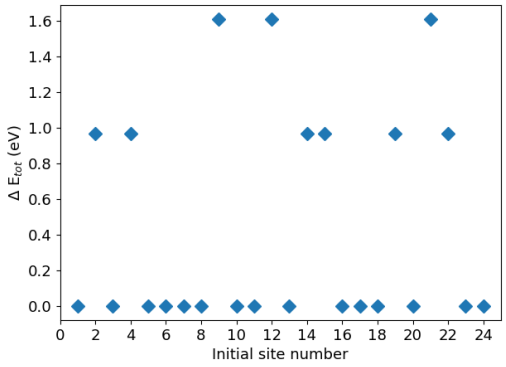

Figure 4.16: Total DFT energy in eV of the 24 trial muon positions after convergence to relaxation thresholds. The reported energy values are re-scaled, with the lowest one chosen as zero.

Table 4.4: Summary of candidate muon stopping sites in Sr_2RuO_4 determined by DFT.

Label	Site Position [a]	$\Delta E(eV)$ [b]
A	(0.225, 0.0, 0.184)	0
B	(0.233, 0.071, 0.5)	0.97
C	(0.0, 0.498, 0.249)	1.61

[a] in coordinates of the unitcell.
[b] DFT total energy difference with respect to site A.

After atomic relaxations, the resulting minima force and energy muon positions were collected and clustered according to their positions and energies. The 24 positions collapse into 3 inequivalent candidate positions when the total energies are considered (see Fig. 4.16). The sites reported in Table 4.4 are representative muon candidate site corresponding to each of the three energy groups. Interestingly, the muon positions in each of the energy related groups are all symmetrically equivalent.

In the candidate muon positions reported in Table 4.4, the total DFT energies dictate that site A is the candidate muon site and site B, C may be safely ignored. The energy difference between A and B (1eV) is a conservative lower limit to the potential well depth for the muon in the A site. Since it is much larger that the

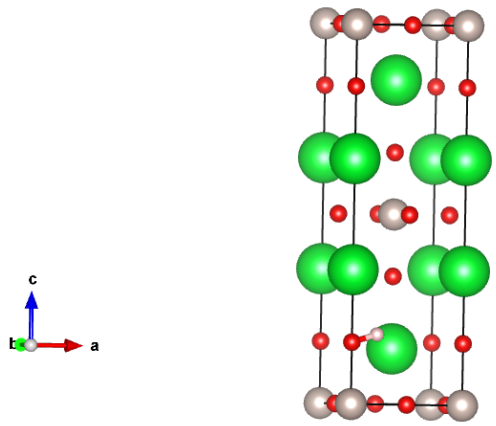

Figure 4.17: The muon site (the light pink sphere) and its bond with oxygen is shown in the undistorted unit cell for clarity.

typical muon zero point energy (0.5 eV), any further calculation of quantum muon correction is irrelevant here.

Site A shown in Fig. 4.17, is identified as the muon implantation site. The muon is clearly bound to oxygen (O2) with bond distance 0.973 Å. This is consistent with known muon sites in oxides including HTS cuprates [55, 152] and pyrochlores [64], where the muon stops close to the oxygen (O) anion, making bonds with O at bond distance of ≈ 1 Å.

With the determination of the muon site, I further investigate the extent of perturbation of the muon *impurity* in the lattice.

4.4.2 Lattice and Density Distortion

The extent of the distortion on the host ions from their equilibrium and its effects on the density of states (DOS) distribution in Sr_2RuO_4 can be extracted from the DFT supercell calculations. Fig. 4.18 shows the displacement of the Sr, Ru and O from their unperturbed position versus their respective distances from the muon. The implanted muon distorts the lattice, introducing a gradient in the potential at the point of implantation, giving rise to the displacement of the host atoms from their equilibrium positions. This displacement vanishes exponentially as the atomic distance gets further away from the site of muon implantation (see Fig. 4.18). The Sr and O1 atoms surrounding the muon are the most perturbed from their equilibrium position with maximum displacement in the range of 0.16 to 0.2 Å. The O2 that forms bond with the muon is displaced by 0.06 Å away from its equilibrium position while the nearest Ru atom to the muon (distance of 2.54 Å) has maximum displacement of 0.038 Å from its equilibrium position.

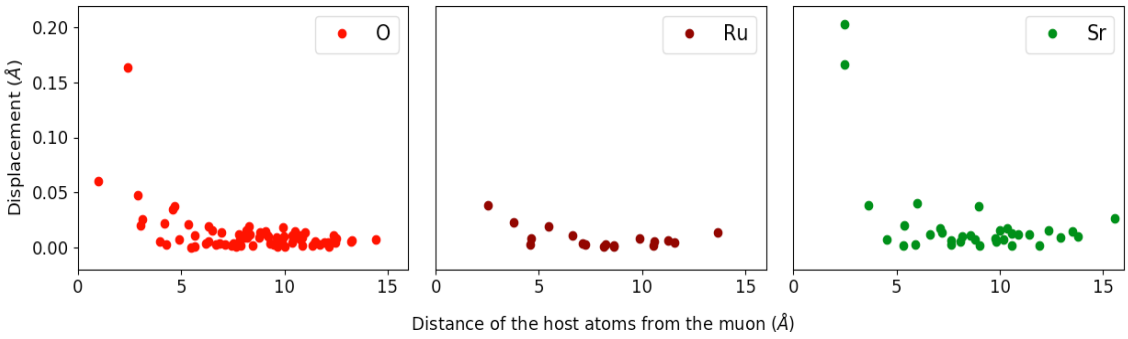

Figure 4.18: DFT determination of the displacement at O, Ru and Sr atoms in the supercell versus their distance from the implanted muon.

From Fig. 4.18 significant distortion from equilibrium positions are observed only for atoms whose distance to the muon implantation position are within 6 Å. The lattice especially neighboring ions to the muon are substantially distorted by the muons.

To further understand the muon effects on Sr_2RuO_4, I further investigate the effect of the lattice distortion on the density of states (DOS). The DOS of Sr_2RuO_4 is that of a metal (similar to results in Ref. [153]) and still remains metallic after the muon implantation Fig 4.19a. To understand the orbital contribution to the DOS, a projection of the DOS to the different atomic orbitals was performed. From the partial density of state PDOS, Fig. 4.19a the contribution very close to the Fermi energy are dominantly of the Ru 4d character pdos similar to LDA results by [154, 155]. Also, with the PDOS, there is a hybridization between the Ru 4d states and O 2p states near the Fermi energy. These contributions are similar and show non-significant changes with the muon implantation.

Since the Ru d states are the dominant states around the Fermi Level, further analysis of the 4d states show that the conduction holes are mostly contributed by the Ru $4d_{zy}$, 4 d_{zx} and $4d_{xy}$ (see Figs. 4.19b and 4.19c), this is consistent to the results obtained using the near-edge x-ray absorption and photoemission spectroscopy. [156] Dotted lines in Fig. 4.19b and Fig. 4.19c are the 4d states contribution calculated with the muon in the sample, the plots are of the Ru atoms closest to the muon (distance of 2.54 Å) and that far from the muon where the displacement is not significant (distance of 8.6 Å) in the supercell respectively. Small changes in the splitting of the states at the Fermi level are observed for the $4d_{zy}$, 4 d_{zx} states of the Ru atom close to the muon Fig. 4.19b and not for that far from the muon Fig. 4.19c. With the summation of the d states contribution of the Ru ions in the supercell, the small state splitting is no longer significant. With the observations from the PDOS with the muon implantation, even though the muon distorts the lattice, these distortions do not alter the DOS.

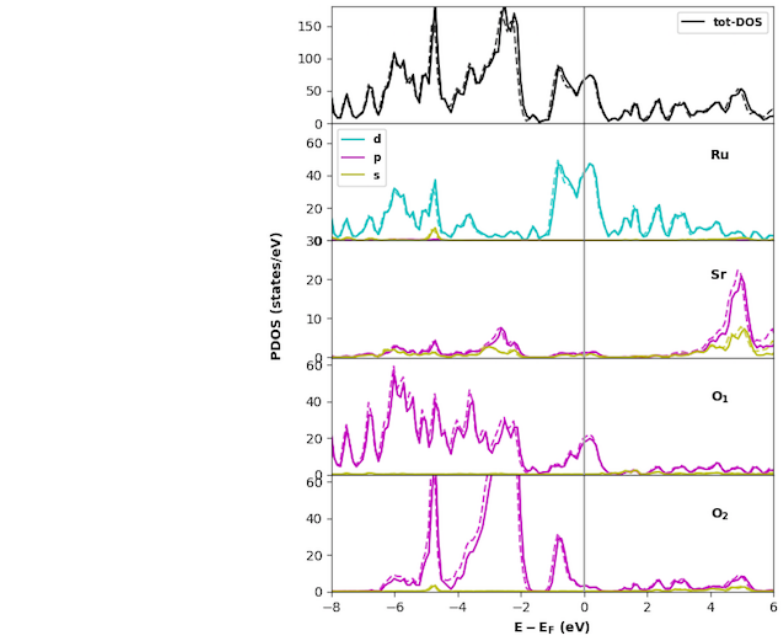

(a)

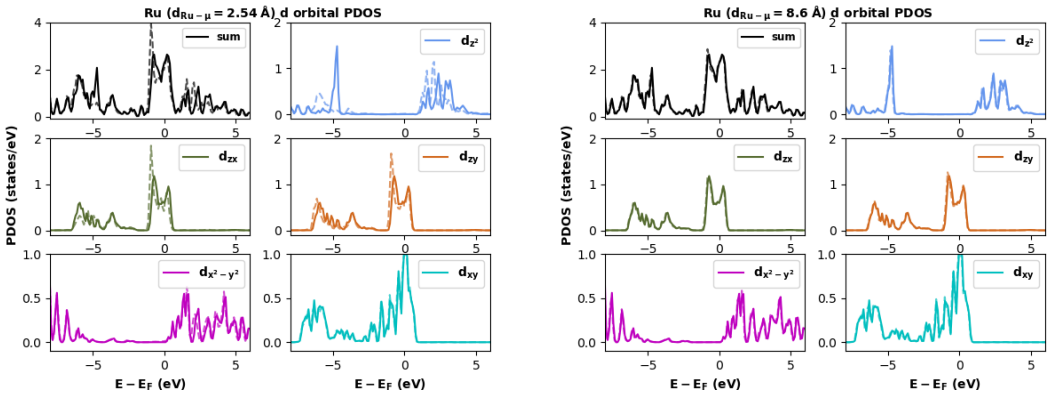

(b) (c)

Figure 4.19: Comparison of the PDOS for the supercells with the muon (solid lines) and those without the muon (**dotted lines**) a) The total and partial projected density of states (PDOS) of Sr_2RuO_4. The **dotted lines** are the PDOS of the supercell with the muon. (b) PDOS of Ru 4d orbital contribution, for Ru atoms and μ distance = 2.54 Å (c) PDOS of Ru 4d orbital contribution with the muon, for Ru and μ distance = 8.6 Å. The Fermi energy has been shifted to 0 eV.

4.4.3 Conclusion and Future work

The muon site has been successfully determined in Sr_2RuO_4, the muon binds to the O2 atom with a bond length of 0.973 Å. The distortion on the lattice and DOS distribution induced by the muon, have been investigated. The distortion in equilibrium position of the host atoms is observed to vanish exponentially from the implantation site of the muon. The study of these distortions, show that significant distortion from equilibrium positions are observed only for atoms whose distance to the muon implantation position are within 6 Å except for Sr. From the projection of the DOS to the different atomic orbitals, the dominant orbital contribution to the DOS close to the Fermi energy are from those of the Ru atoms. However, there was no significant changes in the DOS due to the muon even though significant changes were observed on the lattice in general. This is because considering that the maximum distortion from equilibrium of the dominant contributing Ru atoms is only 0.038 Å, thus the Ru atoms that contributes the most in the electronic properties determination are the least distorted and the distortion is small too. Also, the summation of the contribution of all the atomic orbitals of Ru makes insignificant the small contribution of the distortion of the Ru atoms nearest to the muon. With the above results, the muon distorts its near environment in the lattice but these distortions have no effect on the density distribution of the states.

However, the calculations used to investigate the muon so far, do not consider the effects of electron correlation and spin-orbit coupling. Electron correlation effects and most importantly spin-orbit coupling have been shown to play important roles in the electronic structure of Sr_2RuO_4.[138–141] The incorporation of these effects in DFT studies have allowed to properly reproduce the Fermi surface and its sheet size, leading to a possible counter description of the the ordering mechanism of the Cooper pairs. Also, with spin-orbit coupling further splitting of the band at the Fermi energy has been observed [138]. Thus, the authors in Refs. [138–141] have argued that for understanding the unconventional superconducting state in Sr_2RuO_4 the spin and orbit contribution should not be decoupled.

Therefore, further studies and calculations of the muon distortions and effects in Sr_2RuO_4 incorporating electron correlation and most importantly the spin-orbit coupling are necessary. This will also allow to investigate if the Fermi surfaces and band degeneracy splitting are affected by the implantation of the muon. More general and convincing conclusions on possible muon induced effects in Sr_2RuO_4 will be reached with these calculations.

In summary, at the level of the calculation for the muon in Sr_2RuO_4 presented in this section, the muon was observed to distort the neighbour atoms away from their equilibrium position. However, these distortions decay exponentially and have no appreciable effect on the DOS and electron distribution in Sr_2RuO_4.

5

Muon contact hyperfine field in metals

In this chapter [1], I demonstrate the effectiveness of a DFT-based approach, validated by the comparison with available experimental determinations in the calculation of the muon contact hyperfine field. For this study, five materials are selected by this criterion from the literature, ranging from simple magnetic metals, Fe, Co, Ni, to two additional chiral magnets of current high interest, MnSi and MnGe. The list of metals where the hyperfine coupling is experimentally known is unfortunately scarce, since they require quite accurate and time consuming experiments on single crystals and other methods with huge limitations (See Sec. 2.7). This provides an additional motivation for validating a more general ab-initio method.

In μSR the crucial point that provides *quantitative* access to electronic spin degrees of freedom is the full knowledge of the muon couplings with its surroundings. The often missing key ingredient is the contact hyperfine interaction, notably relevant in metals. These interaction constants between the muon and its atomic surrounding give access to crucial material properties such as the value of the ground state ion magnetic moment in ordered materials and possibly the magnetic structure as well. The qualitative and quantitative knowledge of the different local filed contribution together with the muon implantation site are often necessarily for a complete analysis of available μSR data.

The contributions to the experimental local field, besides the already mentioned dominant dipolar sums, include another trivial term that is shape-dependent (demagnetization) and proportional to the macroscopic sample magnetization. [4] (see Sec. 2.5). In this chapter, the concentration is on the contributions that require a quantum mechanical description of the host electrons in the vicinity of the probe. In a localized spin magnet, they may give rise to direct transferred and supertransferred couplings, depending on whether the wave-function overlap between the muon probe and the magnetic ion is direct or through the polarization of the wave-functions of intervening ligands. In metals, the conduction electrons provide an example of the first kind, giving rise to a contact interaction term, that results

[1] The content of this chapter has been published by my research group at [I. J. Onuorah et al.,Phys. Rev. B 97, 174414 (2018)]

in a spin density at the muon site. The focus is only on the contact hyperfine interaction at the muon.

The theory and source of the hyperfine field at the muon stopping sites are well known and has already been discussed in Section 2.5. In metals, the spin density at the muon site results from the polarization of conduction electrons by the localized d or f shells having unpaired electrons. In the collinear spin approximation, the contact hyperfine field at the muon B_c is(already described in Eq. 2.32);

$$B_c = \frac{2}{3}\mu_0\mu_B\rho_s(\mathbf{r}_\mu) \tag{5.1}$$

where μ_0 is the vacuum permeability, μ_B is the Bohr magneton, and the spin density, ρ_s defined as $(\rho_\uparrow(\mathbf{r}_\mu) - \rho_\downarrow(\mathbf{r}_\mu))$ with $\rho_\uparrow$ and $\rho_\downarrow$ being the density associated to each spinor component at the muon site $\mathbf{r}_\mu$.

This equation was used to evaluate the contact field at the muon with the spin polarization and density obtained from DFT Kohn-Sham wavefunction described in Sec. 3.2.1. The density is of the form;

$$\rho^\sigma(\mathbf{r}_\mu) = \sum_i \langle\psi_i^\sigma|\mathbf{r}_\mu\rangle \langle\mathbf{r}_\mu|\psi_i^\sigma\rangle$$

with superscript σ denoting spin state.

First principle theory of the hyperfine parameters for both heavy and light nuclei in magnetic materials is in principle well understood and has been studied back from the mid 1960's. [19, 20, 42, 157–163] Various approaches were proposed to improve the accuracy of the calculated contact fields, but these investigations, in particular for the muon in metals, were undertaken when computing resources were orders of magnitude less powerful than today. Particularly, due to lack of computing resources, the contact field at the muon was estimated by calculating the unperturbed spin density at the muon while mimicking the effects of the muon on the lattice by a fictitious enhancement factor [19, 164] (See Eq 5.2). Also, the spin density at the muon has been determined by calculating the spin polarized local density of states (LDOS) at the muon interstitial position [161, 162] (See Eq 5.3). These earlier approaches are summarised in the following equations:

$$B_c(\mathbf{r}_\mu) = \frac{2\mu_o}{3}\mu_B\rho_s^{unpt}\eta \tag{5.2}$$

where ρ_s^{unpt} denotes the unperturbed spin polarization at the muon site and η the enhancement factor.

$$B_c(\mathbf{r}_\mu) = \frac{2\mu_o}{3}\mu_B\int^{E_f}\left[\rho^\uparrow(\mathbf{r}_\mu, E) - \rho^\downarrow(\mathbf{r}_\mu, E)\right]dE \tag{5.3}$$

where the local density of states is ;

$$\rho^{\sigma}(\mathbf{r}_{\mu}) = \sum_{i} |\psi_i^{\sigma}(\mathbf{r}_{\mu})|^2 \delta(E - E_i^{\sigma})$$

where ψ_i^{σ} and E represents the eigenfunction and eigenvalue of the system respectively.

The results of these earlier calculations are compared with our calculations in Table 5.2 for the muon in elemental transition metals that form the basis for the validation of the computational approach we propose in this chapter.

More recently valuable theoretical improvements [163, 165–172] have established DFT as the standard for the calculation of NMR shift parameters, most reliably in non magnetic insulators. However, these improved methods were never directly applied to the muon case in metals especially the use of the Projector Augmented-Wave (PAW) method already discussed in Eqs 3.30 and 3.31. The main difference as already noted, is that the location of the nuclei is extremely well known from diffraction, whereas the determination of the muon site is part of the same DFT problem, requiring in addition large supercells to represent the ideally diluted impurity while keeping an accurate description of the bulk sample. Also, the core polarization effects on the spin density that are significant for heavy nuclei, have zero effect on that of the muon with only the s-orbital of no core electronic structure. With the current availability of HPC it is timely to extend these modern methods to muon studies in metallic systems in order to establish their accuracy and applicability.

5.1 Computational details

The pseudopotential and plane-waves (PW) basis approach were used for our calculations.The plane-wave basis is generally used to describe artificially smooth pseudo-wavefunctions thus avoiding the strong oscillations in the core region. In particular, the Projector Augmented-Wave (PAW) method introduced by Blóchl [40–43] allows to approximate the all-electron density using a frozen-core reconstruction starting from the pseudo wavefunction. In the context of the PW basis, the PAW reconstruction method is therefore the method of choice for an accurate evaluation of Eq. 5.1. Since periodic boundary conditions are implied in the description of the bulk system, the effect of the extremely diluted muons in the material must be modeled within the supercell approximation which reduces the artificial interactions between the charged impurities. It must be carefully verified that these artificial interactions of the muon periodic images are negligible on the quantities under study.

For all the calculations in this work, the plane wave cutoffs were always above 100 Ry, granting a convergence on total energy (threshold 10^{-4} Ry) and spin den-

sity, while the exchange correlation functionals were treated within the semi-local Generalized Gradient Approximation (GGA) using the Perdew-Burke-Ernzerhof (PBE) formalism. [30] The calculations were done in the scalar relativistic approach, neglecting spin-orbit coupling. The scalar relativistic approximation is sufficient for the theoretical calculation of the muon contact field since hydrogen (hence the muon) has a small nuclear charge and the contact field is predominantly due to on-site contributions of s-like states surrounding the muon. [163, 173, 174] The Marzari-Vanderbilt [39] smearing function was used.

A uniform Monkhorst-pack [38] mesh was used for the k-points. The convergence of the contact field depends strongly on how dense is the mesh of k-points. A 16×16×16 mesh grid was used for the unit-cell of the transition metals and a 12×12×12 grid for the unit-cell of the B20 compounds. The mesh size were selected following a systematic test to ensure independence on the size used to the spin density and total energies. These grids were down-scaled proportionally for each supercell size.

The first step for all calculations involves the optimization of the structure and the correct reproduction of the electronic and magnetic properties of the pristine material. The next step involves investigating the extent of the lattice distortion around the muon and its influence on the electronic and magnetic properties of the nearest neighbors. The muon was introduced as hydrogen while maintaining a neutral cell considering that in metals, positive charges are effectively screened by the conduction electrons, enforcing charge neutrality of the whole system [61, 62, 65].

The PAW reconstruction and the spin density calculation from the Kohn Sham wavefunction are contained in the PP package of the Quantum ESPRESSO suite of codes. To obtain the spin density at the interstitial center of the muon, the calculation were carried out with the charge density integration grid having a point at the geometrical center of the muon or with re-scaling the atomic positions that the muon position is at the origin while there is a charge grid point at the origin.

Before systematically comparing calculations with experimental values, let us further notice that we expect our results to overestimate the experimental absolute value, in view of the light mass of the muon, which results in relatively large amplitude of zero point vibrations. [2] The muon behaves as a quantum oscillator and the extent of its wave function is completely neglected in the *static* contact field from the DFT approach. The experimental value should be compared to the average over the muon wave function, whose accurate determination will be addressed in the next chapter. For what concerns this chapter, we demonstrate the

[2]The quantum average of the spin density at the muon results in a *reduction* of the point value, since the spin density starts to decay away from that point.

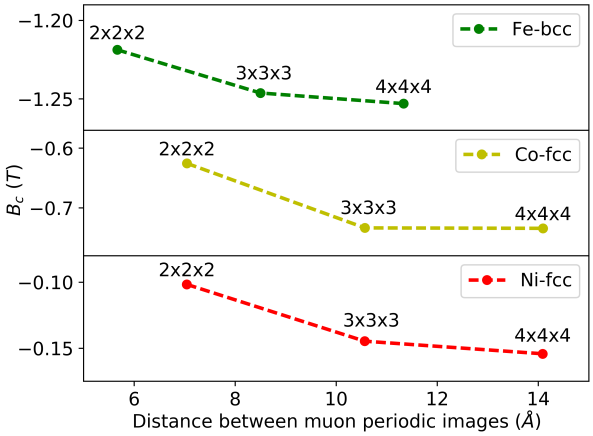

Figure 5.1: Convergence of the muon contact hyperfine field B_c with the distance between muon periodic images for host systems of Fe, Ni and Co. The x,y,z dimension are the supercell sizes with reference to the unit cells.

extent of the accuracy of the DFT based approach to estimate the muon contact hyperfine field.

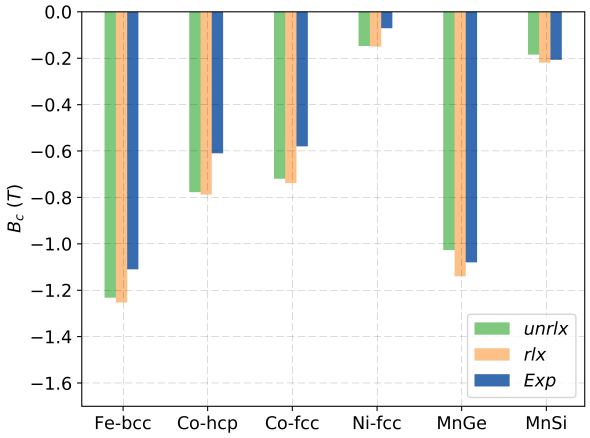

Figure 5.2: Calculated muon contact hyperfine field B_c for unrelaxed ($unrlx$) and relaxed host atoms + muon at fixed cell volume (rlx), compared to the experimental value (Exp).

5.2 Muon effects on the lattice

The appropriate size of the supercell for each of the materials was carefully determined considering convergence of the total DFT energies, distortion of the lattice and magnetic coupling in the vicinity of the muon and in particular the calculated contact hyperfine field, as shown in Fig. 5.1. The plot shows that this quantity converges at the 3×3×3 cell level, however we will compare results on the transition metals obtained with 4×4×4 cells. Following the same systematic tests, a 2×2×2 cell was used for the B20 compounds. Incidentally, in these metals convergence is achieved when the muon periodic replica are above 8.48 Å apart.

Next, we address the issue of whether the relaxation of the host atoms in the supercell including the muon has a significant effect on the quantity of interest. This is obtained comparing muon contact field values B_c with and without atomic relaxation. The results indicate that the relaxation around the muon affects significantly only the positions of the nearest neighbor ions. The distortions are short ranged and small because the positive charge of the muon is screened by the electron cloud in metals, a fact that is directly shown in Fig. 5.3. Furthermore, Fig. 5.2

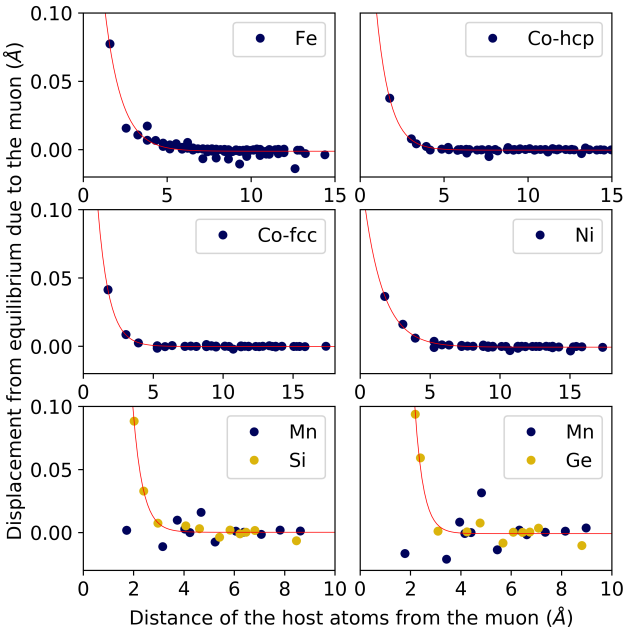

Figure 5.3: Atomic displacement in the presence of the muon in a relaxed supercell, vs. the distance of each atom from the muon. Red lines are guide to the eye showing the exponential decay.

shows that the direct effect of relaxation on the value of B_c is tiny compared to the deviation between experiment and theory at this level of approximation. However, the reported results in this work are those of the relaxed lattice.

The range of the lattice strain introduced by the interstitial muon defect may be directly quantified by comparing the position of each atom in the pristine material with their position in the supercell DFT calculation, after lattice relaxation with the muon. Fig. 5.3 shows the difference of these two quantities versus the distance from the muon site. The top four panel display the result for the 4×4×4 cell of the elemental metals, with a clear exponential decay on a length-scale, $\lambda < 1.25$ Å.

The data for the 2×2×2 cell of the B20 compounds are more scattered, as expected in view of the presence of two different species. Interestingly, Si and Ge show a decaying displacement with $\lambda < 3.0$ Å whereas Mn ions show no systematic deviation, perhaps indicating a much shorter value of λ.

5.3 PAW reconstruction accuracy

Finally, we want to determine the relative accuracy of the pseudo-wavefunction (PS) spin densities compared to those obtained by the PAW Reconstruction (PR) method described in Sec. 5.1. These are reported in the last two columns of Table 5.1 as $\rho_s^{PS}(\mathbf{r}_\mu)$ and $\rho_s^{PR}(\mathbf{r}_\mu)$ respectively and the corresponding contact field is plotted in Fig. 5.4 and compared with the experimental values. The pseudo wavefunctions even though do not include the actual core electron density, give

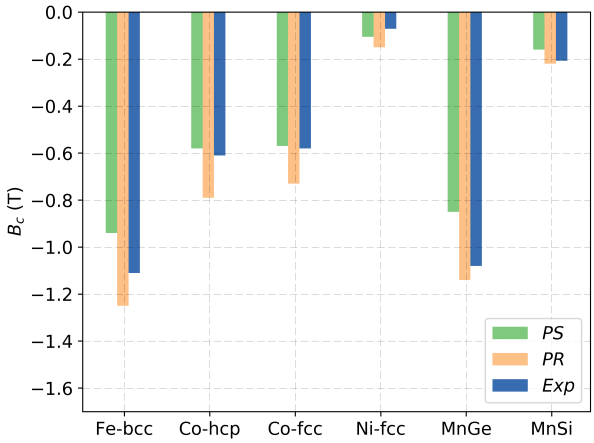

Figure 5.4: Muon contact hyperfine field B_c calculated with the spin densities from the pseudo-wavefunction (PS) and from the all electron reconstruction with the PAW method (PR), compared to the experimental value (Exp).

Table 5.1: Spin only magnetic moment for each magnetic ion (without the muon) for the conventional GGA calculation m_{GGA}, the experimental value m_{exp} and the reduced Stoner theory calculation (see Sec.(5.5)) m_{RST} in units of μ_B; muon sites [57, 58, 161, 175–177] in fractional coordinates; calculated spin density at the muon in atomic units of (a_0^{-3}) resulting from the pseudo-wavefunction ρ_s^{PS} and the PAW reconstructed value ρ_s^{PR}.

Host metals [1]	m_{GGA}	m_{exp} [2]	m_{RST}	Muon site	$\rho_s^{PS}(\mathbf{r}_\mu)$	$\rho_s^{PR}(\mathbf{r}_\mu)$
Fe - bcc	2.17	2.22	-	0.50, 0.25, 0.00	-0.0179	-0.0238
Co - hcp	1.585	1.72	-	0.33, 0.67, 0.25	-0.0111	-0.0150
Co - fcc	1.645	1.59	-	0.50, 0.50, 0.50	-0.0109	-0.0139
Ni - fcc	0.638	0.606	-	0.50, 0.50, 0.50	-0.0020	-0.0028
MnGe	2.014	1.83	1.84	0.552, 0.552, 0.552	-0.0162	-0.0217
MnSi	1.00	0.4	0.401	0.541, 0.541, 0.541	-0.0031	-0.0042

[1] The MnGe and MnSi structure are of $P2_13$ space group (cubic) with the Mn atom at (0.138,0.138,0.138) crystal unit position.
[2] See Refs. [57, 58, 178].

results remarkably close to the experimental values. It should be noted however that this is probably due to an error compensation between the approximated core electronic density and the missing zero point vibration corrections. In addition, the overshooting of all estimations obtained with PR is in agreement with the fact that corrections due to zero point vibrations may lead to a reduction of the absolute value (as mentioned in Sec. 5.1) thus, systematically improving the agreement with the experimental data for all the compounds reported in Fig. 5.4.

5.4 Fe, Co, Ni

We have investigated the accuracy of the calculated magnetic moments and the effects of the muon on them. The experimental total magnetic moments of the transition 3d metals, shown in Table 5.1, are well reproduced within the conventional GGA-DFT. The tabulated magnetic moment were estimated with the Löwdin population analysis. [179] With the muon impurity in the lattice, the moment of the nearest neighbor host magnetic ions are negligibly perturbed. These perturbations contribute to no appreciable change of the calculated contact field. As we will further discuss, the contact field depends strongly on the accuracy of the calculated spin moments.

The first important result obtained is that the calculated spin imbalance at the muon, shown in Table 5.1, is negative for all the considered metals, in agreement

with experiment and with the simple notion that the majority spin electrons are in a direction opposite to the bulk magnetization at the muon. Furthermore, the deviations, reported in Table 5.2, are on average 0.14 T and always within 0.2 T. This may be considered a rather good agreement, compared to results from the earlier works, since the averaging due to the muon's vibration is not included yet.

Admittedly, many of these earlier works [19, 20, 164, 180] estimated the spin density at the muon site by a simple re-scaling of the spin density of the bulk material at the position of the known muon site with an empirical spin enhancement factor that mimics the perturbation induced by the interstitial muon. This is clearly an unpractical ad-hoc solution that impairs the ab-initio method. They thus failed to establish the accuracy of the method over several materials.

In the earlier calculations, the large deviations between calculated and experimental contact field values (on average) were consistently attributed to the lack of muon zero point motion correction. Our more accurate results indicate that the effect of the zero point motion is needed but its extent is much smaller.

5.5 MnGe and MnSi

The muon implantation sites for MnSi and MnGe [57, 58] are reported in Tab. 5.1. Their zero field magnetic structure, actually a spin spiral, was approximated by a collinear ferromagnetic state since in both cases the pitch [57, 58, 181, 181–183] is much longer than the lattice parameter.

The conventional DFT calculated spin only moment, m_{GGA}, deviates significantly from the experimental total magnetic moment for both B20 compounds, and for MnSi in particular. This is a consequence of the poor standard DFT description of spin fluctuations in the magnetic ground state especially for itinerant electron systems. This also affects the calculated spin-density at the muon. For MnSi $m_{GGA} = 1.0\mu_B$, while the experimental value is $m_{exp} = 0.4\mu_B$. Notably, the ratio of these two values matches the ratio of the calculated and experimental contact fields, for the calculated spin density of -0.0107 (a_0^{-3}). This is also the case for MnGe (see Table 5.1), with calculated spin density -0.0251 (a_0^{-3}). Thus, the accuracy of the calculated contact field is heavily influenced by how well the host ground state magnetization is reproduced by DFT. A simple but non ab-initio way to predict experimental contact field values would consist in re-scaling the fields by the ratio m_{exp}/m_{GGA} or constraining the total moment of the bulk material [184] to the known experimental value.

Ab-initio approaches have been discussed in the literature for MnSi. Attempts to obtain the experimental local moment by the reduction of the lattice constant within the local density approximation (LDA) [185] work only for unphysical lattice constant values. Hubbard U correction (DFT+U) to redistribute electrons between

Table 5.2: Calculated static contact hyperfine field at the muon B_c by PAW reconstruction together with results from other works, experimental values B_c^{exp} and deviations $\Delta^{exp} = B_c^{exp} - B_c$.

	B_c [T]			
Host metals	this work	other works	exp	$\Delta^{exp}[T]$
Fe-bcc	-1.25	-0.94 [19]	-1.11 [175]	0.14
,,		-1.01 [188]		
,,		-1.44 [161]		
,,		-1.03 [162]		
Co-hcp	-0.79	-1.34 [19]	-0.61 [176]	0.18
,,		-0.57 [188]		
Co-fcc	-0.73	-0.46 [161]	-0.58 [161]	0.15
Ni-fcc	-0.15	-0.69 [19]	-0.071 [177]	0.08
,,		-0.059 [188]		
,,		-0.13 [161]		
,,		-0.31 [20]		
,,		-0.059[159]		
MnGe	-1.14	-	-1.08 [58]	0.06
MnSi	-0.22	-	-0.207 [57]	0.013

the majority and minority channels [186, 187] acknowledge unphysical results in the pressure dependence of the magnetic moment (and we checked that the spin density at the muon departs from experiment).

A different approach was proposed by Ortenzi [189] who implemented a reduced Stoner theory (RST) modification to the exchange-correlation functionals. This approach involves the reduction of the ab-initio Stoner parameter in the conventional spin polarized DFT, by a spin-scaling factor (ssxc) in the exchange correlation potential. As already discussed in section 3.4, for spin polarized calculations, the dependent of the total DFT energy functional on the spinor component is realized on the exchange correlation part (See Eq. 3.22). Since the exchange correlation potential is a functional of the total charge and magnetization (see Sec. 3.4), the scaling is such that the total energy remains unchanged while the magnetization is scaled. For the purpose of scaling the magnetization, the exchange correlation potential part with the magnetization Eq. 3.25 is now of the form:

$$\tilde{B}_{xc}(\mathbf{r}) = cB_{xc}(\mathbf{r}) \tag{5.4}$$

where c represents the spin scaling factor of the exchange correlation potential (ssxc)

With this approach, the energy gain due to spin polarization within the conventional Stoner interaction criterion is reduced. This reduction was shown [189] to have a correspondence to the Moriya's self-consistent renormalization (SCR) theory. [190] The SCR theory is known to describe successfully the ground state properties of weak itinerant ferromagnet, and in particular that of MnSi. [191, 192]

This method is variational and it adjusts the magnitude of the spin polarisation for all standard functionals. We re-implemented it in the Quantum Espresso code, and obtained $m_{RST} \approx m_{exp}$ with ssxc values of 0.83 and 0.95 respectively for MnSi and MnGe, as in Table 5.1. The band structure remains negligibly changed, although band are shifted in energy accordingly to the reduced Stoner parameter. Our results for the contact field, in good agreement with experiments, were obtained with spin densities calculated from this approach and are summarized in Table 5.2.

5.6 Conclusion

We have reviewed and validated a systematic approach to the calculation of the muon's static contact hyperfine field in metals. We have successfully established the accuracy of the estimation of the muon contact field in metallic compounds with DFT. The pseudopotential DFT approach within the PAW formalism is good even for itinerant magnets, notoriously difficult systems.

The results may be affected by poor DFT reproduction of the magnetic moment which is common for these systems. The RST method allows a variational approach that may well reproduce the experimental results (both the magnetic moment and spin density) without forcing unphysical values of the other lattice quantities.

DFT calculation of contact hyperfine fields is a viable assistance to μSR data analysis. Its standard implementation may well replace expensive, time consuming and often not readily available single crystal measurements in the future.

However, the final results even though at this level of approximation are consistent with experimental values, they are obtained for an infinite muon mass and do not account for its finite zero point vibrations. The full treatment of the effects of the muon's zero point vibration will be considered and discussed in the next chapter.

6

Muon quantum motion effects and hyperfine fields in metals

The muon by reason of its very light mass ($\approx 1/9^{th}$ of the proton mass) undergoes a large zero-point motion when implanted in the host compound. The spread of the muon wavefunction can be of the order of 1 Bohr radius. In most cases this effect is non-negligible in atomistic simulations involving the description of muon states at rest in compounds. When treating the muon as a positive interstitial impurity using *ab initio* electronic structure methods [20, 56, 62, 65] within the Born-Oppenheimer approximation (see Sec. 3.1) where the nuclei and the electrons are treated separately, muon mass induced effects are neglected. The muon behaves as a quantum oscillator and it is always important to include the extent and effect of its wave function spreading in calculations. The neglect of the quantum ground state effects of the muon in DFT calculations has two major consequences: it yields inaccurate values of the contact hyperfine field and can also lead to the trapping of the muon in different interstitial local minima during force relaxations [66]. In this chapter, I describe an approach to treat the muon zero-point motion. The effects of these quantum motion are included in *post* DFT calculations on the muon properties considered, which include the total DFT energy for stability of muon localization site and in particular, the influence of this inclusion on the calculation of the contact hyperfine field. For what concerns the latter, the effects of the muon motion are included by averaging over the extent of the muon wave function spreading.

Determining the muon wave function in each chemical environment entails mapping the muon potential and solving the Schrodinger equation that describes the muon interaction. However, mapping the potential felt by the muon is not trivial and to a first approximation the muon potential has been taken to be harmonic [62, 193] such that the muon quantum description involves studying its vibrational modes. However, from ab-initio total energy calculations, the muon potential is known to be very anharmonic.[20, 56, 193, 194]

In this chapter, I describe a stochastic self-consistent harmonic approximation (SSCHA) that allows to include the effects of anharmonicity in the muon potential

starting from the harmonic approximation following the approach by I. Errea et al. [195, 196]. This approach has been very successful in treating hydrogen for calculating thermal expansion and superconducting[197] properties. With this approach I demonstrate that huge anharmonicity renormalizes the harmonic muon vibrational modes, as expected of the muon due to its light mass. Also, with the anharmonicity renormalized muon harmonic vibrations, I included the quantum corrections and effect of the muon mass on the calculated static muon contact hyperfine field in metallic systems discussed in the previous chapter.

6.1 Double Born-Oppenheimer approximation

As discussed earlier in Sec. 3.1, the Born-Oppenheimer(BO) approximation allows to separate the motion of the electrons and the nuclei in view of their large mass difference, such that one can describe the Hamiltonian for the nuclei with an effective potential surface that describes the interaction with the electrons. Here, for the quantum treatment of a single muon *impurity* in the compound, the Double Born-Oppenheimer approximation (DBO) [56, 193, 198] is used, such that the motion of the electron is separated from that of the muon and host nuclei, and further the motion of the muon is separated from that of the nuclei. The separation of the motion of the different particles is justified since the muon is 200 times heavier than an electron, typically 400 times lighter than a transition metal nucleus and 143 times lighter than oxygen (care must be taken when considering e.g. hydrogen, only 9 times heavier than a muon). In the many body problem described in Chapter 3.1 and Eq. 3.2 there are no coordinates describing explicitly the muon mass motion, since the charged muon is treated as a charged hydrogen impurity within the electronic problem. However, I re-write the total Hamiltonian in Eq. 3.2 including the muon kinetic energy as;

$$H_{tot} = T_e + T_\mu + T_N + V(\mathbf{r}_e, \mathbf{r}_\mu, \mathbf{R}_N) \tag{6.1}$$

with subscript μ describing the muon related quantities while e and N describe those of the electron and nuclei respectively. The Schrödinger equation is;

$$H_{tot} \left|\Psi_{tot}\right\rangle = E_{tot} \left|\Psi_{tot}\right\rangle \tag{6.2}$$

With the DBO, the BO wavefunction in Eq. 3.3 can be re-written as a product wavefunction of the electrons, the muon and the nuclei in the form;

$$\left|\Psi_{tot}\right\rangle = \left|\psi_e\right\rangle \left|\phi_\mu\right\rangle \left|\Phi_N\right\rangle \tag{6.3}$$

The Hamiltonian for the electronic problem already discussed in Eq. 3.4 can be re-written to specifically point out the presence of the muon position operator

as;

$$H_e = T_e + V(\mathbf{r}_e; \mathbf{r}_\mu, \mathbf{R}_N) \tag{6.4}$$

Similar to the BO approximation, only the position operators of the muon and the nuclei enter in the eigenvalue problem of the electrons. The solution of the electronic problem gives the BO potential energy surface, $V(\mathbf{r}_\mu, \mathbf{R}_N)$ dependent on the muon and the nuclei position operators. Hence, the ground state Hamiltonian H_μ for the muon can be written as:

$$H_\mu = T_\mu + V(\mathbf{r}_\mu; \mathbf{R}_N) \tag{6.5}$$

where the muon kinetic energy T_μ is defined as

$$T_\mu = \sum_{\lambda=1}^{3} \frac{p_\lambda^2}{2m_\mu}$$

with p the momentum operator along the Cartesian component indexes, λ while m_μ is the muon mass.

The solution of the Schrödinger equation of the muon Hamiltonian Eq. 6.5 is not trivial, since the absence of the muon motion leads to the de-localization of the muon in energy minima positions over large volumes of the shallow total DBO potential energy surface $V(\mathbf{r}_\mu; \mathbf{R}_N)$ resulting from the solution of the electronic problem. However, the DBO approximation is advantageous since it allows to consider separately only the degrees of freedom relating to the muon, thus understanding the true muon motion behaviour. It also saves a lot of computational effort, time and resources as will be described in the next section.

6.2 Stochastic self-consistent harmonic approximation (SSCHA) for muons

Before entering into the details of SSCHA let me first illustrate an important consequence of the DBO approximation on this method when applied to the muon. In solving the electronic problem Eq 6.4, the muon is treated as a hydrogen impurity, such that within the periodic lattice approach in the DFT calculation, sufficiently large supercell must be used to avoid the artificial interaction with the muon's periodic images. With the increase in the size of the cell, the number of irreducible modes and minimization components required for the SSCHA method grows. To reduce drastically the computational resources and time required with the periodic supercell in the SSCHA, the DBO approach is invoked to treat the muon quantum nature while limiting the degrees of freedom to only those relating to the muon. In the SSCHA, restricting the vibrational modes to only those relating to the muon

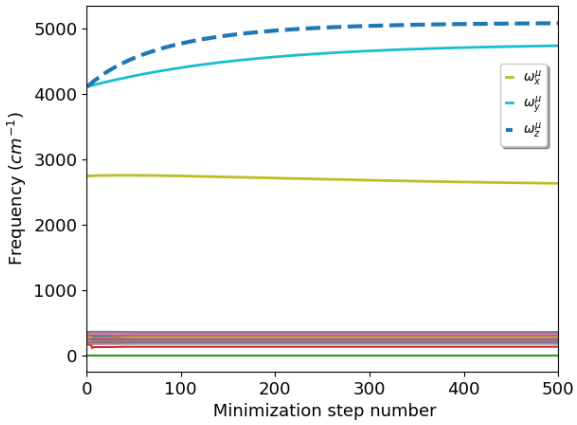

Figure 6.1: Evolution of the muon frequency (ω^μ) and those of Fe (nearly static low frequency lines in red-like colours) during SSCHA minimization for muon in tetrahedral site of Fe-bcc. The figure depicts the expected strong anharmonicity effects on the muon frequencies and nearly non-existent anharmonicity effects on those of Fe, due to the large mass difference of the muon and Fe nuclei. The muon is $\approx$ 490 times lighter.

is justified since the effect of anharmonicity in the vibrations of heavier nuclei including those of the 3d elements are largely negligible compared to those of the muon (see Fig 6.1). In the following description of the SSCHA, the host nuclei vibrations are kept fixed, such that only the muon vibrations and anharmonicity on its vibration modes are considered.

To continue with the formal description of the SSCHA for the muon, the muon Hamiltonian H_μ is simply written as H and the DBO potential energy surface $V(\mathbf{r}_\mu; \mathbf{R}_N)$ can basically be described as $V(\mathbf{r}_\mu)$, since the interest is on a potential for the muon influenced only by changes in the muon coordinates. In the formalism for the SSCHA, the exact analytical form of the muon potential $V(\mathbf{r}_\mu)$ is not known.

The zero point energy of the exact muon Hamiltonian H is given as:

$$E_H = \langle \phi_H | H | \phi_H \rangle \tag{6.6}$$

where the density matrix is $\rho_H = \sum A |\phi_H\rangle \langle \phi_H|$ and $\sum A = 1$ and $|\phi_H\rangle$ is the muon ground state wavefunction.

Calculating E_H is far from trivial since the form of the muon potential (Eq. 6.5) is not known. However, it is possible to establish a quantum variational principle for the muon ground state energy E_H, by replacing the exact muon wavefunction $|\phi_H\rangle$ with the wavefunction $|\phi_{\widetilde{H}}\rangle$ of a trial muon Hamiltonian $\widetilde{H} = T_\mu + \widetilde{V}(\mathbf{r}_\mu)$.

This is such that one can define an energy functional of the trial Hamiltonian as;

$$\widetilde{E}_H[\widetilde{H}] = \langle \phi_{\widetilde{H}} | H | \phi_{\widetilde{H}} \rangle \tag{6.7}$$

The variational form of the muon ground state energy can be written as:

$$E_H \leq \widetilde{E}_H[\widetilde{H}] \tag{6.8}$$

such the equality holds when the potentials are the same.

by adding and subtracting Eq. 6.10 to Eq. 6.7, $\widetilde{E}_H[\widetilde{H}]$ can be written in the form;

$$\widetilde{E}_H[\widetilde{H}] = E_{\widetilde{H}} + \left\langle \phi_{\widetilde{H}} \middle| (V - \widetilde{V}) \middle| \phi_{\widetilde{H}} \right\rangle \tag{6.9}$$

while the energy resulting from the analytic trial Hamiltonian $\widetilde{H}$ can be written as;

$$E_{\widetilde{H}} = \left\langle \phi_{\widetilde{H}} \middle| \widetilde{H} \middle| \phi_{\widetilde{H}} \right\rangle \tag{6.10}$$

The above definitions allow to formulate a variational principle following the Gibbs-Bogoliubov inequality theorem [199] at zero temperature, similar to the Rayleigh-Ritz inequality[200].

The probability density $\rho_{\widetilde{H}}$ is defined as;

$$\rho(\mathbf{r}_\mu)_{\widetilde{H}} = \langle \mathbf{r}_\mu | \rho_{\widetilde{H}} | \mathbf{r}_\mu \rangle = \left| \phi_{\widetilde{H}}(\mathbf{r}_\mu) \right|^2 \tag{6.11}$$

Provided the probability density for the system to be in the muon position $\mathbf{r}_\mu$ can be calculated, an observable A dependent only on $\mathbf{r}_\mu$ can be averaged statistically within the form of the corresponding Hamiltonian $\widetilde{H}$ as;

$$\langle A \rangle_{\widetilde{H}} = \int d\mathbf{r}_\mu A(\mathbf{r}_\mu) \rho(\mathbf{r}_\mu)_{\widetilde{H}} \tag{6.12}$$

Then the muon energy in Eq. 6.9 can be evaluated as;

$$\widetilde{E}_H[\widetilde{H}] = E_{\widetilde{H}} + \int d\mathbf{r}_\mu \rho_{\widetilde{H}}(\mathbf{r}_\mu)(V(\mathbf{r}_\mu) - \widetilde{V}(\mathbf{r}_\mu)) \tag{6.13}$$

With the above form of $\widetilde{E}_H[\widetilde{H}]$, the muon energy can be evaluated at each step during the minimization and one can directly see that the equality in the form of the variation in Eq. 6.8 holds if $V = \widetilde{V}$. Hence, with the variational principle, the ground state potential $V(\mathbf{r}_\mu)$ of the muon is determined if the potential $\widetilde{V}(\mathbf{r}_\mu)$ that minimizes $\widetilde{E}_H[\widetilde{H}]$ is found.

6.2.1 Initial harmonic potential

The starting trial potential for the muon in the variation is the harmonic potential. This allows to study the vibrational modes of the muon and also feasible to allow the renormalization of these vibrational modes by anharmonicity. The resulting potential is therefore an *effective* harmonic potential producing a ground state muon wave function that approximates well that of the true anharmonic potential. With this choice we exploit the fact that the ground state wave function is trivial to write. Another justification for this choice of potential is that, with the harmonic potential, it is easier and straightforward to describe the probability density of the muon in the potential and express it in terms of the muon position, phonon frequencies and the polarization vector. Thus, as the minimum potential is found, the resulting muon vibrational modes and in turn the ground state energy are those renormalized by anharmonicity.

The initial muon harmonic Hamiltonian is of the form;

$$\widetilde{H} = \sum_{\lambda=1}^{3} \frac{p_\lambda^2}{2m_\mu} + \frac{1}{2}\sum_{\lambda\nu}^{3} K^{\lambda\nu}(r_\mu - r_\mu^{eq})^\lambda (r_\mu - r_\mu^{eq})^\nu \tag{6.14}$$

where λ and ν are Cartesian component indexes, $\mathbf{r}_\mu^{eq}$ is the muon equilibrium position, m_μ is the mass of the muon and $K^{\lambda\nu}$ is the muon 3×3 force constant matrix. The dynamical matrix $K^{\lambda\nu}/m_\mu$ can be constructed and diagonalized as;

$$\sum_{\nu=1}^{3} \frac{K^{\lambda\nu}}{m_\mu} \epsilon_{i\widetilde{H}}^{\nu} = \omega_{i\widetilde{H}}^2 \epsilon_{i\widetilde{H}}^{\lambda} \tag{6.15}$$

where i is the index of each of the orthogonal modes, $\epsilon_{i\widetilde{H}}^{\nu}$ is the polarization vector and $\omega_{i\widetilde{H}}$ is the muon vibration frequency corresponding to the trial Hamiltonian $\widetilde{H}$ for each mode.

It is straightforward to demonstrate the solution of the Schrödinger equation with the muon Hamiltonian of Eq 6.14 and the probability density of the harmonic oscillator at the muon position $\mathbf{r}_\mu$ can then be written as:

$$\rho(\mathbf{r}_\mu)_{\widetilde{H}} = \left(\frac{1}{\pi^3 \prod_{i=1}^{3} \sigma_{i\widetilde{H}}^2} \right)^{\frac{1}{2}} exp\left(-\sum_{\lambda\nu i}^{3} \frac{\epsilon_{i\widetilde{H}}^{\lambda} \epsilon_{i\widetilde{H}}^{\nu}}{\sigma_{i\widetilde{H}}^2} (r_\mu - r_\mu^{eq})^\lambda (r_\mu - r_\mu^{eq})^\nu \right) \tag{6.16}$$

where $\sigma_{i\widetilde{H}}$ is the normal length for each of the mode i is given as:

$$\sigma_{i\widetilde{H}} = \sqrt{\frac{\hbar}{m_\mu \omega_{i\widetilde{H}}}} \tag{6.17}$$

If the probability density is defined, with the quantum statistical averaging already defined in Eq. 6.12, the ground state energy of the muon's initial harmonic Hamiltonian can be calculated as;

$$E_{\widetilde{H}} = \sum_{i=1}^{3} \frac{1}{2} \hbar \omega_{i\widetilde{H}} \tag{6.18}$$

6.2.2 Energy minimization and stochastic implementation

From the variational principle already discussed above, the ground state muon energy is achieved by a conjugate gradient (CG) minimization algorithm [201] when;

$$E_H = \min_K \widetilde{E}_H[\widetilde{H}] \tag{6.19}$$

where the force constant matrix K is directly proportional to the muon frequency (see Eq. 6.15), that the muon frequency that minimizes the energy is the muon ground state frequency renormalized by anharmonicity.

If the *equilibrium* implantation site of the muon $\mathbf{r}_\mu^{eq}$ is known and also remain fixed by symmetry, for example muons that occupy symmetrical octahedral and tetrahedral interstitial positions, minimizing $\widetilde{E}_H[\widetilde{H}]$ with respect to the trial potential $\widetilde{V}$ is similar to minimizing with respect to the force constant matrix $K^{\lambda\nu}$. Hence, the muon energy is minimized with respect to the force constant matrix. For the muon in a high symmetry position, the force constant matrix is a 3 x 3 Hermitian matrix, and the only non-zero elements are the diagonal elements of the matrix. If the equilibrium position of the muon is not precisely known and perhaps not at a high symmetry position, the the muon energy can also be minimized with respect to the muon position, such that the $\mathbf{r}_\mu$ and $K^{\lambda\nu}$ that minimizes $\widetilde{E}_H[\widetilde{H}]$ are those of the ground state [196]. Minimization with respect to $\mathbf{r}_\mu$ is beyond the scope of this work, since the area of consideration for this work is on materials where there is sufficient knowledge of the equilibrium muon implantation site.

A very important quantity required for the CG minimization is the gradient of the energy $\nabla_K \widetilde{E}_H[\widetilde{H}]$ with respect to the force constant K. The gradient can be obtained by the chain rule as partial derivatives with respect to the mode length σ_i and polarization vector ϵ_i (see Eqs. 6.15 and 6.17) :

$$\nabla_K \widetilde{E}_H[\widetilde{H}] = \sum_i \frac{\partial \widetilde{E}_H[\widetilde{H}]}{\partial \sigma_{i\widetilde{H}}} \nabla_K \sigma_{i\widetilde{H}} + \sum_{i\lambda} \frac{\partial \widetilde{E}_H[\widetilde{H}]}{\epsilon^\lambda_{i\widetilde{H}}} \nabla_K \epsilon^\lambda_{i\widetilde{H}} \tag{6.20}$$

with the analytic form written as [196]:

$$\nabla_K \widetilde{E}_H[\widetilde{H}] = -\sum_{i\lambda\nu} \sqrt{\frac{m_\mu}{2}} \left(\epsilon^{\lambda}_{i\widetilde{H}} \nabla_K \sigma_{i\widetilde{H}} + \nabla_K \epsilon^{\lambda}_{i\widetilde{H}}\right) \epsilon^{\nu}_{i\widetilde{H}} \times \int d\mathbf{r}_\mu [f^\lambda(\mathbf{r}_\mu) - f^\lambda_{\widetilde{H}}(\mathbf{r}_\mu)](r_\mu - r^{eq}_\mu)^\nu \rho_{\widetilde{H}}(\mathbf{r}_\mu) \tag{6.21}$$

where $f^\lambda(\mathbf{r}_\mu)$ is the muon force component in the direction of the Cartesian indexes λ for all muon positions $\mathbf{r}_\mu$ and $f^\lambda_{\widetilde{H}}(\mathbf{r}_\mu)$ are the forces obtained with the $\widetilde{V}$ potential.

In the minimization of the initial harmonic Hamiltonian, the symmetry of the system is preserved. It is assumed that the *anharmonic* ground state Hamiltonian of the muon has the same symmetry as the harmonic one, such that the anharmonic Hamiltonian obeys and performs operations with the symmetry of the harmonic ones.[196]

In principle, solutions to higher order (order > 3) terms in the anharmonic coefficients are computationally expensive and complicated to calculate. [202–204] Also, they are overly computationally heavy when a large cell *supercell* is considered. Instead, the approach to include anharmonicity effects involves evaluating the integral in Eq. 6.12 *stochastically* by statistically averaging over a number of ionic configurations chosen by importance sampling technique[205] and reweighting technique if required. The advantage of this approach is that it makes use of the known analytic form of $\rho_{\widetilde{H}}(\mathbf{r}_\mu)$.

From importance sampling, for an operator A that depends on the atomic position, its quantum statistical average can be calculated by averaging the operator over sufficiently large number of configurations, N_c. Thus, the statistical average Eq. 6.12 is performed stochastically over N_c random configuration in the form:

$$\int d\mathbf{r}_\mu A(\mathbf{r}_\mu)\rho(\mathbf{r}_\mu)_{\widetilde{H}_0} \simeq \frac{1}{N_c}\sum_{n=1}^{N_c} A(\mathbf{r}^n_\mu) \equiv \langle A \rangle_{\widetilde{H}_0} \tag{6.22}$$

The N_c random muon configurations are generated by making use of random numbers $\{\xi_{in}\}_{n=1,\ldots,N_c}$ created with the Gaussian distribution of $\rho_{\widetilde{H}}(\mathbf{r}_\mu)$ and rescaled by the corresponding normal length modes $\sigma_{i\widetilde{H}}\xi_{in}$ and polarization vector $\epsilon^{\lambda}_{i\widetilde{H}}$. As already discussed, the host nuclei are kept fixed and the random muon position configurations are then generated with the following distribution;

$$(r^n_\mu)^\lambda = (r^{eq}_\mu)^\lambda + \sum_{i=1}^{3} \frac{1}{\sqrt{2}} \epsilon^{\lambda}_{i\widetilde{H}} \sigma_{i\widetilde{H}} \xi_{in} \tag{6.23}$$

For each of the N_c configuration, the forces on the muon $\mathbf{f}(\mathbf{r}_\mu)$ and the BO energy $\widetilde{V}$ due to the muon displacement are calculated, these are used for the stochastic statistical averaging while evaluating the gradient (See Eqs. 6.21 and 6.22).

The forces and energy are calculated outside the SSCHA with any of the *ab initio* methods including DFT[27] and Hartree-Fock[24–26] methods.

Calculation of the forces and energy for the N_c configuration accounts for the computationally expensive part in the SSCHA minimization cycle. After the first step in the CG minimization, these expensive force and energy calculations are circumvented by a reweighing procedure at each step for $j > 0$ in the minimization cycle, considering that hundreds of step are required before the minimum is found. The reweighing procedure involves multiplying the importance sampled integral Eq. 6.22 at each step j by a factor $\wp(\mathbf{r}_\mu^n)$ defined as:

$$\wp(\mathbf{r}_\mu^n) = \frac{\rho_{\widetilde{H}_j}(\mathbf{r}_\mu^n)}{\rho_{\widetilde{H}_o}(\mathbf{r}_\mu^n)} \tag{6.24}$$

such that for each step j in the CG minimization, the muon energy $\widetilde{E}_H(\widetilde{H})$ and the energy gradient $\nabla_K \widetilde{E}_H(\widetilde{H})$ are averaged statistically by importance sampling and reweighing techniques as:

$$\int d\mathbf{r}_\mu A(\mathbf{r}_\mu)\rho(\mathbf{r}_\mu)_{\widetilde{H}_j} \simeq \frac{1}{N_c}\sum_{n=1}^{N_c} A(\mathbf{r}_\mu^n)\wp(\mathbf{r}_\mu^n) \equiv \langle A\rangle_{\widetilde{H}_j} \tag{6.25}$$

If $j = 0$, $\wp(\mathbf{r}_\mu^n) = 1$. Eq. 6.25 has *real* effects only for $j > 0$. The operator A represents the quantity being evaluated, which is either the muon energy $\widetilde{E}_H(\widetilde{H})$ or the energy gradient $\nabla_K \widetilde{E}_H(\widetilde{H})$.

The use of the stochastic approach allows to evaluate the stochastic error on the quantities of interest. The error also gives information on the sufficiency of the number of configuration N_c used in the calculation. The choice of N_c should be such that the numerical *noise* is almost non-existent *i.e* the statistical error vanishes. For Eq. 6.25 the statistical error $\Delta\langle A\rangle_{\widetilde{H}_j}$ is ;

$$\Delta\langle A\rangle_{\widetilde{H}_j} = -\frac{1}{\sqrt{N_c}}\sqrt{s^2} \tag{6.26}$$

where the variance s^2 can be written as;

$$s^2 = \frac{1}{N_c - 1}\sum_{n=1}^{N_c}\left(A(\mathbf{r}_\mu^n) - \langle A\rangle_{N_c}\right)^2 \tag{6.27}$$

6.2.3 Self-consistent cycle

In the minimization process there are two stopping criteria that must be satisfied to achieve the minimum muon energy.

a.) In the first criterion the minimization is aborted without finding the minimum. It involves the failure of the reweighing procedure for the forces and BO energy needed for the stochastic averaging at each minimization step j. In this criteria a threshold, τ_1 is set such that for the minimization to continue;

$$\left| 1 - \left\langle \frac{\rho_{\widetilde{H}_j}}{\rho_{\widetilde{H}_o}} \right\rangle \right| < \tau_1 \tag{6.28}$$

This condition ensures that the reweighed forces and energies of N_c muon configuration at the first minimization step used in stochastic averaging of $\widetilde{E}_H[\widetilde{H}_k]$ and $\nabla_K \widetilde{E}_H[\widetilde{H}_k]$ are sufficient to accurately calculate them. Small values of τ_1 between 0.2 to 0.3 were used to enforce that $\left\langle \frac{\rho_{\widetilde{H}_j}}{\rho_{\widetilde{H}_o}} \right\rangle$ does not significantly deviate from 1. When the condition (Eq. 6.28) is not obeyed, that is the value on the left-hand side is above the threshold τ_1 , the minimization is stopped indicating that the number of random configuration, N_c used for the stochastic averaging is not sufficient. At this point one restarts the minimization, while regenerating a larger number of random configuration preferably using the potential (dynamical matrices) before the previous minimization step $j-1$ that failed owing to the above stopping criteria. This allows to speed-up the minimization and reach convergence in fewer iterations.

b.) The second criterion indicates the end of the minimization, such that the potential(dynamical matrix) that minimizes the muon ground state energy has been found. The minimization should in principle continue until the gradient of the free energy vanishes. Here, a threshold τ_2 is set for the gradient of the muon energy $\nabla_K \widetilde{E}_H[\widetilde{H}]$ such that;

$$\left| \nabla_K \widetilde{E}_H[\widetilde{H}_j] \right| \leq \tau_2 \tag{6.29}$$

where the value of τ_2 should be close to zero and also preserve numerical stability. In this work values of the order 10^{-4} in Hartree atomic units were used.

When the minimum has been found i.e the condition in Eq. 6.19 is obeyed, the resulting dynamical matrix and thus muon frequency has been renormalized by anharmonicity. The resulting frequency is an *effective* vibrational frequency ω_i^{eff} that the muon ground state energy E_H can be written as:

$$E_H = \sum_{i=1}^{3} \frac{1}{2} \hbar \omega_i^{eff} \tag{6.30}$$

A flowchart that describes the minimization cycle of the SSCHA method is presented in Fig. 6.2. The SSCHA results in renormalizing the muon harmonic vibrational modes by anharmonicity. Basically, this is achieved by minimizing the harmonic potential by a CG minimization technique with respect to the vibrational

frequencies, such that by stochastic statistical averaging of the minimization gradient with random forces acting on the muon in the compound,the anharmonicity of the muon potential is incorporated in the minimization.

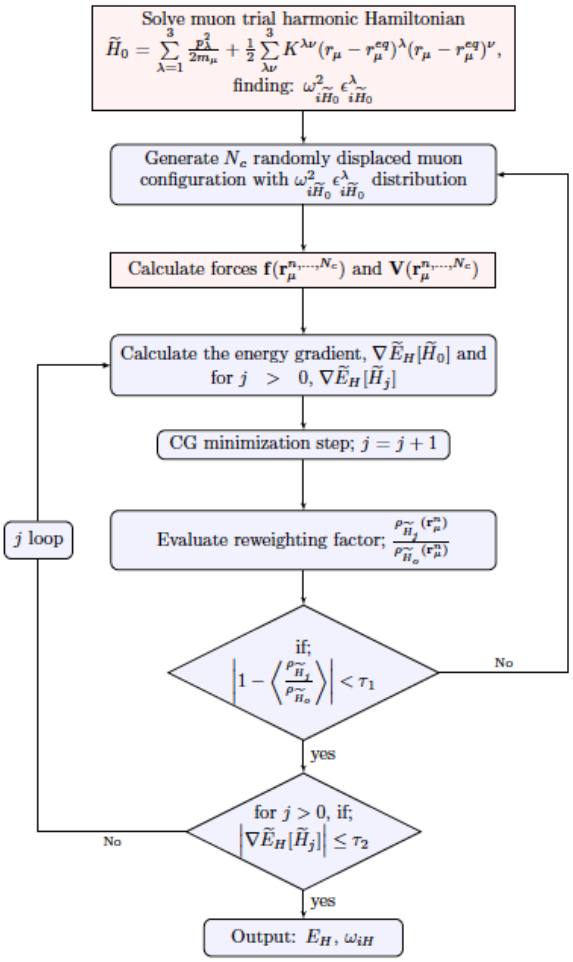

Figure 6.2: Flowchart describing the cycle for the stochastic self-consistent harmonic approximation for evaluating the muon zero point vibration. The charts on *sky blue* are only the part of the method contained in the SSCHA code. The solution of the initial trial harmonic Hamiltonian and the force calculation (chart in *pink*) are carried out outside the code by other *ab initio* methods and constitute the time consuming part of SSCHA with more computational resource requirements.

6.3 Effective muon frequencies

With the SSCHA described above, the zero point energy of the muon is calculated for same set of metallic systems (Fe, Co, Ni, MnSi, MnGe) for which the static muon contact hyperfine field was calculated in the previous chapter (Chapter 5). The already calculated *static* hyperfine fields do not include the effect of the muon zero point motion which is principally realized by averaging over the spreading of the muon wavefunction. In this section, the SSCHA approach is used to describe the zero point motion of the muon and form of the muon wavefunction in each of these magnetic materials.

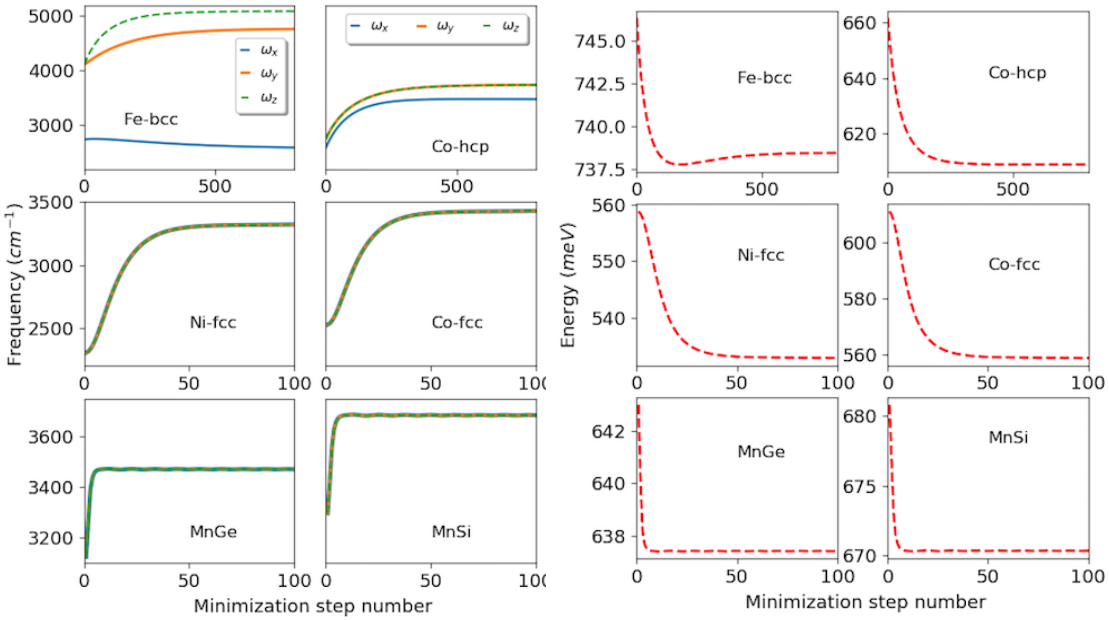

Figure 6.3: (a) Evolution of the muon frequency during the SSCHA minimization (b) Evolution of muon energy as in Eq. 6.13 during the SSCHA minimization. In both figures the starting point for the minimization step number = 0 is that of the initial trial harmonic Hamiltonian

The muon dynamical matrix of the trial starting harmonic Hamiltonian were calculated by the finite difference method [206, 207]. With the finite difference approach, it is easier to consider only the muon modes and also the resulting muon dynamical matrix compares well with those calculated by the linear response approach[208, 209] provided the displacement is along same direction. Only the frequency mode corresponding to the muon has been considered since, strong anharmonicity effects are observed only for the muons and the frequency of the host

Table 6.1: Anharmonic renormalized effective muon harmonic frequencies ω_i for different mode direction i, the corresponding muon energy E_0 and the muon energy with a *pure* harmonic approximation $\widetilde{E}_0$.

Host metals	ω_x (cm^{-1})	ω_y (cm^{-1})	ω_z (cm^{-1})	E_0(eV)	$\widetilde{E}_0$ (eV)
Fe - bcc [a]	2572.58	4769.08	5088.37	0.77	0.68
Fe - bcc [b]	2011.64	2011.64	6358.46	0.64	- [c]
Co - hcp	3741.10	3741.10	3476.24	0.68	0.53
Co - fcc	3424.16	3424.16	3424.16	0.64	0.49
Ni - fcc	3317.78	3317.78	3317.78	0.62	0.44
MnGe	3470.29	3470.29	3470.29	0.65	0.58
MnSi	3685.25	3685.25	3685.25	0.69	0.61

[a] Here muon is at the tetrahedral site
[b] Here muon is at the octahedral site
[c] The muon is not stable at the octahedral site within the harmonic regime.

nuclei remains negligibly unchanged by anharmonicity (see Fig. 6.1 for muons in Fe). SSCHA minimization with only the muon modes simplifies the whole process considering that a suitably large cell has been used in the calculation to incorporate the convergence of the muon *impurity* induced effects.

For the minimization and the stochastic averaging (see Eq 6.22) implemented within the SSCHA, to ensure that the muon energy gradient vanishes, hundreds of random configurations where generated for the muon while keeping the host atoms fixed. For these configurations, the Hellmann-Feynman forces[210] and energy were calculated with DFT[1] as contained in the Quantum ESPRESSO suite of code [46]. The evolution of the muon frequencies in these materials during the SSCHA minimization Fig. 6.3a, show that the muon frequencies are strongly renormalized by anharmonicity. The stochastic implementation ensures that the effect of the muon vibrations, the effect of the chemical environment around the muon and anharmonic contributions to the forces acting on the muon are all incorporated in the muon's ground state minimum.

The muon zero point energy for the different materials were calculated from Eq. 6.30 and shown in Fig. 6.30 with the anharmonicity renormalized frequency used as an effective frequency ω_μ^{eff} in the harmonic regime. The effect of the anharmonicity in this effective approximation is a change in the spreading of the

[1]The DFT computational details for a muon in a supercell of Fe, Ni, Co, MnGe and MnSi are the same as described in Sec. 5.1 of the previous chapter except for the supercell size of the elemental metals used in the force calculation. A $2 \times 2 \times 2$ cell was used for Fe and $3 \times 3 \times 3$ cell for Ni and Co.

muon's wavefunction. The calculated zero point vibrations with the anharmonicity renormalized frequency along the direction of mode displacement are reported in Table 6.1 and compared to the harmonic ones.

6.3.1 Tetrahedral and octahedral muon site in Fe

Conflicting experimental and theoretical reports attribute the Fe muon site to either the tetrahedral (T) or to the octahedral (O) site. From the point of view of the total DFT energy, the T site is 0.184 eV lower that the O site. This would indicate that the T site is the stable one, although the small difference doesn't exclude that both may be populated.

Phonon calculations using density functional perturbation theory provide further insight on the stability of the two candidate sites: unphysical *negative* frequencies generally signal an instability. This is the case for the muon at the O site, as opposed to those of the T site, always positive. The harmonic approximation then appears to indicate instability of the muon at the O site.

However, the anharmonic effects, fully captured by the SSCHA method, yield positive frequencies also for the O site, indicating the instability as an artifact of the harmonic approximation. The calculated SSCHA values are reported in Table 6.1 for all studied metals and in particular for the two muon candidate sites in Fe. All of them are positive. Therefore both sites for the muon appear to be stable when anharmonicity in the muon vibration is fully taken into account. This is an important result of the SSCHA treatment.

Coming back to the problem of which candidate site is occupied in Fe, since both T and O turn out to be stable with SSCHA, the only subtle difference between them is the total energy of the DFT calculation, that favours the T site, but is not large enough to guarantee that the O site should be excluded.

6.4 Quantum corrections on muon contact hyperfine field

The light muon mass effect is included in the contact field by considering the extent of the spread of its wavefunction in the host metal, such that the magnitude of the muon-motion-averaged contact field is smaller than the static contact field at the muon geometrical interstitial center. This explains the systematic overestimation of the calculated static contact hyperfine field (see Table. 6.2 and Fig 6.5)

The quantum effects of the muon vibration were calculated by averaging with the effective harmonic muon wavefunction the static contact hyperfine field of the muon randomly displaced along the muon frequency mode direction within the normal length σ_i Eq. 6.17 (see Eq. 6.23). The muon averaging is given as; [62]

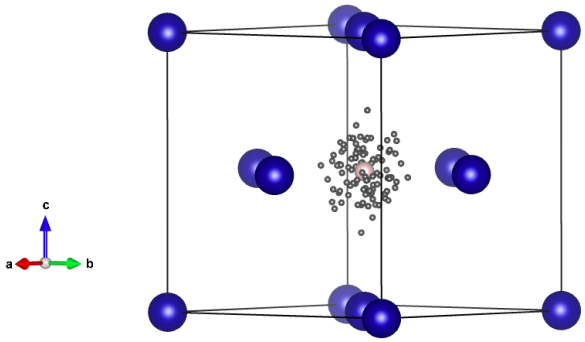

Figure 6.4: 100 random position generated using Eq. 6.23 for the muon at octahedral site in Co-fcc unit cell. The geometrical octahedral center is depicted by the pink sphere, while the small dark spheres represents the different muon positions where the muon static contact hyperfine field $B_c(\mathbf{r}_\mu)$ where also calculated for averaging the effects of the muon motion.

$$\langle B_c \rangle = \frac{\int r_\mu^2 d\mathbf{r}_\mu \left|\phi(\mathbf{r}_\mu)\right|^2 B_c(\mathbf{r}_\mu)}{\int r_\mu^2 d\mathbf{r}_\mu \left|\phi(\mathbf{r}_\mu)\right|^2} \tag{6.31}$$

The probability density $\left|\phi(\mathbf{r}_\mu)\right|^2$ for a quantum oscillator describing the muon is defined in Eq. 6.16, with the muon wavefunction spreading already renormalized by anharmonicity. To ensure a three dimensional averaging of $\mathbf{B}_c(\mathbf{r}_\mu)$, the integration was weighted by r_μ^2. However, it is important to note that even though the points used for the averaging are random as shown in Fig. 6.4, the averaging method is sufficient for such random configurations. Sufficient number of configurations were sampled considering the extent of the wavefunction spreading for each of the compound considered.

$B_c(\mathbf{r}_\mu)$ is the static contact field calculated at the muon position $\mathbf{r}_\mu$. The integral in Eq 6.31 was achieved for each of the metals by averaging over $B_c(\mathbf{r}_\mu)$ calculated on a number (hundreds) of muon configuration randomly displaced off the muon equilibrium position $\mathbf{r}_\mu^{eq}$ (see Fig. 6.4). The various muon configurations were sampled following the description in Eq. 6.23. These random muon configuration are the same configurations used for the muon total energy minimization within the SSCHA method. Since the positions are displaced while considering the muon modes, the maximum displacement of any of the random muon position is within the vibration amplitude of the muon. The amplitude of vibration is of the order of 1 Bohr radius.

The calculated *static* $B_c(\mathbf{r}_\mu)$ and *averaged* $\langle B_c \rangle$ contact field are listed and compared to the experimental value in Table 6.2 and Fig. 6.5. From the results, the averaged contact fields are in better agreement with the experimentally ob-

Table 6.2: Calculated static contact hyperfine field at the muon $B_c(\mathbf{r}_\mu)$, B_c averaged over the spreading of the muon wavefunction $\langle B_c \rangle$ and experimental values B_c^{exp}

Host metals	$B_c(\mathbf{r}_\mu)$ [T]	$\langle B_c \rangle$ [T]	Exp
Fe-bcc	-1.25	-1.09	-1.11 [175]
Co-hcp	-0.79	-0.64	-0.61 [176]
Co-fcc	-0.73	-0.69	-0.58 [161]
Ni-fcc	-0.15	-0.14	-0.071 [177]
MnGe	-1.14	- 1.02	-1.08 [58]
MnSi	-0.22	- 0.19	-0.207 [57]

Here muon is at the tetrahedral site

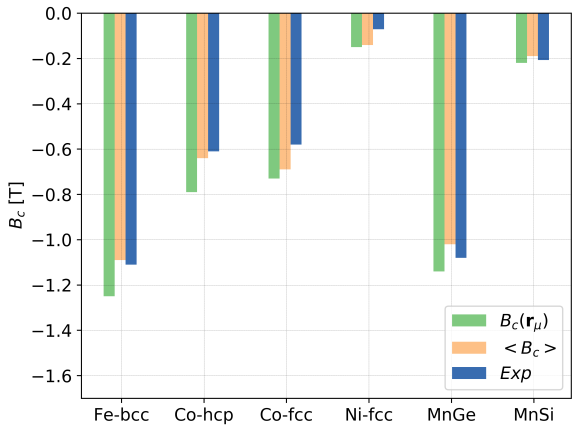

Figure 6.5: Static contact hyperfine field $B_c(\mathbf{r}_\mu)$ at the muon implantation position $\mathbf{r}_\mu$, the muon contact field averaged over the muon wavefunction spreading, $\langle B_c \rangle$ and experimentally observed contact field Exp

served values than those of the static contact field. This indicates the influence of the muon wavefunction spreading on its interaction with the electrons in the host compound. However, even though the muon has a large zero-point vibration energy, the effect of the muon motion when averaged on the contact field is not large. In earlier calculations[20, 161, 162], the large deviation of the spin densities and in turn the contact field were explained with the absence of the large muon zero-point motion effects. We however point out that this is not the case, even though we don't rule out entirely the effects of the zero point vibration, large portion of the deviation on their results is due to an incomplete representation of the density of the system by the electronic structure theory method they used.

6.5 Conclusion

The absence of the muon motion effects in DFT calculations for muons is a major challenge that has limited the accuracy in the prediction of calculated muon properties including the hyperfine fields and its site of implantation in the lattice. The stochastic self consistent harmonic approximation described in this chapter allowed an improvement with respect to the harmonic approximation already used for treating of the muon quantum effects. Indeed the anharmonic contributions to the muon potential is incorporated by considering the anharmonicity in the forces acting on the muon in the lattice instead of the cumbersome outright calculation of the higher order anharmonic coefficients. In principle, the code runs in minutes on personal computers, however huge computational resources goes into the computation of total-energy and forces of the large number of ionic configuration used in the muon total energy calculation. The reweighing technique approach to avoid the force calculation for each minimization step has been discussed.

The method has been used to describe the muon potential and zero-point motion energy in the elemental metals Fe, Co, Ni and the material of current interest of MnSi and MnGe. The effects of the muon zero-point motion was incorporated in the calculation of the muon contact hyperfine field in these materials by averaging over the spreading of the muon wavefunction. The SSCHA method for the muons, show strong anharmonic renormalization of the harmonic muon potential in orders of 0.08 - 0.18 eV for the materials considered in this chapter. The stochastic implementation ensures that the effect of the muon vibrations and the effect of the chemical environment around the muon are all incorporated in the muon's ground state minimum. The calculated zero-point energy of the muon, even though large constitutes small relaxations in the averaging of the calculated contact field. Nevertheless, the calculated hyperfine fields including the effects of the muon wavefunction spreading compares better with experimentally observed values than the static hyperfine fields.

7

Hydrogen defect states and muon hyperfine coupling in MnO and NiO

This chapter includes discussion on DFT+U studies of the hydrogen defect sites and their effects on the electrical conductivity properties of transition metal monooxides(TMMO) of MnO and NiO. Also, this chapter includes the studies of the muon implantation site in these materials and confirmation of the spin moment alignment direction in the antiferromagnetically (AF) ordered samples by dipolar field calculations.

MnO and NiO are wide band gap insulators of the unfilled 3d manifold, whose electronic and optical properties have been widely studied because of the interesting properties they possess and possible application in optical computing due to their large optical response. [211] Interest in these materials is also motivated because of the failure of the conventional band theory within DFT to correctly describe the insulating band behaviour. Correct description of electron correlation is not well represented within the conventional DFT. The band width of the 3d electrons is smaller than the Coulomb energy U acting among electrons, giving rise to the correlation between the electrons and accounting for the band gap opening at the Fermi energy. In order to retrieve correctly these features within DFT, strong electron correlation must be treated by incorporating the Hubbard U corrections, as described in Sec. 3.3. The standard correlated systems were the DFT+U approach has been benchmarked are mostly those of the TMMO including NiO and MnO [36, 37, 212, 213]. This approach has also been implemented in the calculation of the optical spectra and dielectric function of MnO, NiO, CoO, and FeO. [214] Thus, calculation details including the values of U used for calculations presented in this chapter were adopted from previous studies [213].

In early years the transport properties of TMMO were widely studied to establish their insulating behaviour. The influence of vacancies and interstitial defects on their transport and optical properties were also highlighted. Neutron diffraction measurements and theoretical studies show that these vacancy and interstitial defects in TMMO exist mostly in clusters rather than isolated in the lattice except for NiO. [211, 215–221] The defects were reported to have induced the rerrange-

ment of the magnetic moment and oxidation states of the cations in the vicinity of the defects in the magnetic TMMO due to the perturbation of the magnetic exchange interaction/superexchange of the neighbour cation sites as observed in FeO. [215] Cation vacancies give rise to p-type conduction, [219] and modify other thermodynamic properties [222]. Modifications are reported also by neutral oxygen vacancies in TM dioxides. [223] Further surface studies on the TMMO and possible applications in solar energy has also been studied by DFT+U [224] together with defect effects in the surfaces of these oxides.[225] Also surface studies on Fe_2O_3, Cr_2O_3, V_2O_3 has been reported [226, 227]. Point defects including mostly the vacancy defects and self interstitial defects have been studied in NiO and MnO. However, the defect properties on the band gap of light mass interstitials like hydrogen have not been reported.

In sample growth and preparation, hydrogen can be incorporated unintentionally from sample interaction with the environment, hence the need to understand the effects of hydrogen defects. Also, another motivation for the study of the light impurity defect in NiO and MnO includes: the various reports of the emergence of hydrogen induced donor and acceptor states in the band gap, and modification of the $3d$ and $2p$ bands by the hydrogen defects. Hydrogen defect is important for its influence on transport properties in a wide range of semiconductors and insulators: hydrogen induces acceptor level (0/-) states in Si, GaAs, ZnSe, ZnTe and ZnS [8, 228, 229], donor level (+/0) states in CdTe, CdS, CdSe and ZnO [54, 230–232] and amphoteric defect levels in Y_2O_3 and Lu_2O_3 [52, 233–235]. Hydrogen in ZnO forms a shallow donor state, a fact demonstrated by the observed muon radical state. Instead, in the semiconducting oxide TiO_2,[236] the effect of hydrogen defect is to change the band edges at the Fermi level.

Measurements and characterization of hydrogen defects in samples are not trivial since they require high sensitivity. However, since the muon can be regarded as a pseudo isotope of hydrogen, μSR is used to study hydrogen defects in various semiconducting and insulating materials. The muon can exist in insulators as a diamagnetic muon that is chemically bound to one of the host atoms in particular the anions e.g oxygen and as a paramagnetic muonium atom, i.e when it is bound to an electron to form muonium (μ^+e^-). [8, 237] A non-exhaustive list of materials where μSR has been used to characterize hydrogen defects include; Si, where muonium forms a bond at the centre between two Si atoms with intermediate properties on electron binding energy and hyperfine interaction [8, 228], ZnO and cadmium chalcogenides (eg. CdS) [232] where they form shallow bound donor states and are sources of n-type conductivity [54, 230, 231]. Also, muonium has been observed in magnetic MnF_2 ([1] and references there in), TiO_2 [238], Lu_2O_3 [235]. Muons most often form diamagnetic states in inorganic insulators. Muonium radicals are usually found in organic unsaturated compounds (they form breaking double

and triple bonds). They are much less frequent in inorganic materials and can be found for instance in quite a number of insulators. The use of muonium as hydrogen proxy for the study of conducting behaviour in semiconductors has been reviewed in Ref. [8].

In this chapter, using DFT+U, I study both the neutral and charged hydrogen defect sites and their effects on the band gap of MnO and NiO, together with the stability of these defect states by considering the formation energies. Also, I further discuss the muon implantation site in these materials together with the magnetic moment alignment direction by dipolar summation and comparison with the already reported μSR measured muon precession frequency in MnO [22] and NiO [239].

7.1 Structural and computational details

The hydrogen defects in MnO and NiO were studied using plane-wave DFT+U with the GGA approximation for the exchange correlation functional, while the PAW formalism was used for the pseudopotentials. U values of 5.25 eV and 5.77 eV for the 3*d* Mn and Ni ions respectively, were adopted following Ref. [213]. These values of U have been demonstrated to reproduce well the electronic structure and insulating character of MnO and NiO. In this case, I will show that the use of the DFT+U is necessary for the correct identification of the muon site in the structural relaxations.

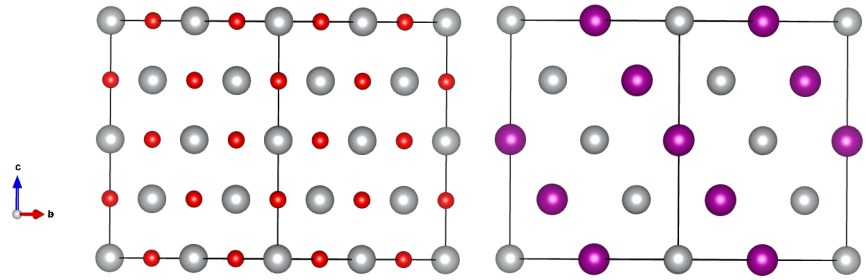

Figure 7.1: All plots are along the *b* axis (a) 2×2×2 supercell structure of MnO. Red spheres are the oxygen atom while the ash spheres represents Mn atoms. The structure of NiO is same with Ni occupying the Mn positions (b) Supercell showing the AF ordering of the Mn ions (same for Ni in NiO). For clarity the O atoms are not shown. The AF order consists of ferromagnetic sheets along the (111) direction, with opposite moment alignment of the nearest neighbour sheets (shown in different sphere colours). Figures were plotted with *VESTA*.[67]

The paramagnetic phase of MnO and NiO are of the rocksalt structure [240, 241] with the Fm3m crystal symmetry, where each atom has six nearest neighbour forming an octahedron. At the ground state, both compounds are ordered antiferromagnetically, where magnetic moments (see Fig. 7.1b) are ferromagnetic within 111 planes, lie within that plane and are aligned in opposite direction in adjacent planes. [240–242] To accomodate the magnetic structure and defects in the lattice, a 2×2×2, 64 atom supercell with lattice parameters of 8.8630 Å and 8.3408 Å [241] were used for MnO and NiO respectively.

The electronic structure and stability of the magnetic structure in MnO have been studied theoretically in Ref. [243] where the AF ordering as shown in Fig. 7.1b was confirmed to be the most stable in agreement with experimental results.[240] The magnetic structures of TMMO have been observed with neutron diffraction measurements to be slightly distorted by magnetostriction from the perfect cubic structure with an elongation of the cell along the edge of the (111) direction into a rhombohedral structure [240]. This distortion has also been observed in DFT calculations. [244] These slight distortions were neglected in the calculations with the cell volume kept fixed, assuming that they have negligible effect on the electronic and magnetic properties. Also, it was assumed that the hydrogen interstitial defects do not alter the magnetic ordering of the TMMO systems. This was later confirmed by the resulting total magnetization from the structural relaxations with the impurity. In the calculations, the AF order described above was used within a collinear spin formalism.

A 4×4×4 Monkhorst-pack grid was used for the Brillouin zone sampling of the 2×2×2 supercell. For the structural optimization and relaxations, the energy and forces were relaxed till threshold of 10^{-4} Ry and 10^{-3} Ry/a.u respectively.

7.2 Hydrogen sites and band gap defect levels

In order to study the effects of point hydrogen defect on the band behaviour of MnO and NiO, all the possible charged states of hydrogen have been considered: the positively charged (H^+), neutral (H^0), and the negatively charged (H^-) states. The allowed hydrogen charged states in the considered TMMO can be understood by studying the site of localization and stability of the resulting sites. With DFT+U, force and energy relaxations of the MnO and NiO supercell containing the different charged hydrogen state impurity were performed. The initial trial positions are those from the uniform grid that spans the whole cell, while for H^+ and H^- impurity, the supercells were kept positively and negatively charged respectively.

The structural relaxations result in several local minima energy sites for each of the hydrogen charged states. By clustering the resulting H sites considering

	A - H^+ [a]	B - H^+	C - H^+	2A - H^0	2B - H^0	3A - H^-
MnO	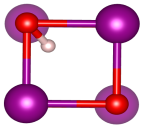 0.0 eV	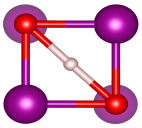 0.22 eV	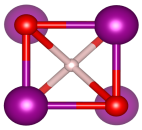 1.53 eV	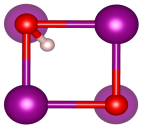 14.44 eV	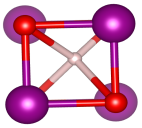 14.54 eV	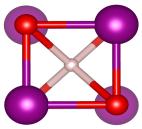 27.77 eV
NiO	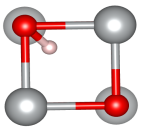 0.0 eV	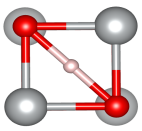 0.21 eV	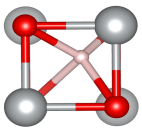 1.0 eV	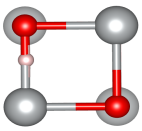 12.57 eV	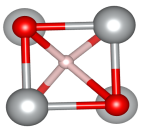 14.05 eV	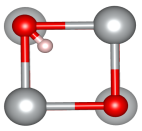 27.14 eV

[a] A represents the site label, while H^+ indicates the charged state of the hydrogen impurity

Figure 7.2: Localiztion sites of the hydrogen impurity for different charged states H^+, H^0 and H^- shown with bonds to their near neighbour host atoms. A, B, C represents site labels for each charged state. The hydrogen atoms are represented with the pink spheres, oxygen the red spheres and Mn the violet and Ni the ash spheres. The energy in eV are the DFT total energy with respect to the structure with the lowest energy for MnO and NiO. Effects of the ionic distortion in the vicinity of the H impurity are not shown in the images. Figures were plotted with *VESTA*.[67]

the positions and total DFT energies, 3 different energy minima positions were found for H^+, 2 for H^0 and 1 for H^- in both MnO and NiO. Fig. 7.2 shows the resulting hydrogen sites with the bonds they make with neighbour ions together with their different DFT energies in eV relative to the site with the lowest energy for each sample. Large differences in DFT energy among the positive and negative or positive and neutral defect is due to the differences in the number of electrons. However the energy differences reported is just a way of showing the DFT energies.

As shown in Fig. 7.2, there are different types of bond formation which include: an oxygen-hydrogen (O-H) bond, an oxygen-hydrogen-oxygen (O-H-O) bond and a Ni-H-O bond. Also, a body center interstitial position was recovered in both MnO and NiO. For the H^0 impurity, the minimum energy site is the site with the O-H^0 bond in MnO, while the Ni-H^0-O is the lowest for NiO. In both MnO and NiO the O-H site are the lowest energy sites for the positively charged states with O-H bond length between 0.96 and 0.98 Å. The resulting localization site for the H^- in NiO has an O-H bond of 0.7 Å, this is surprisingly small.

The study of the charged hydrogen impurity localization sites shows that correct description of the ground state band structure and gap opening are essential. The conventional DFT treats the insulating TMMO as metals because of incorrect

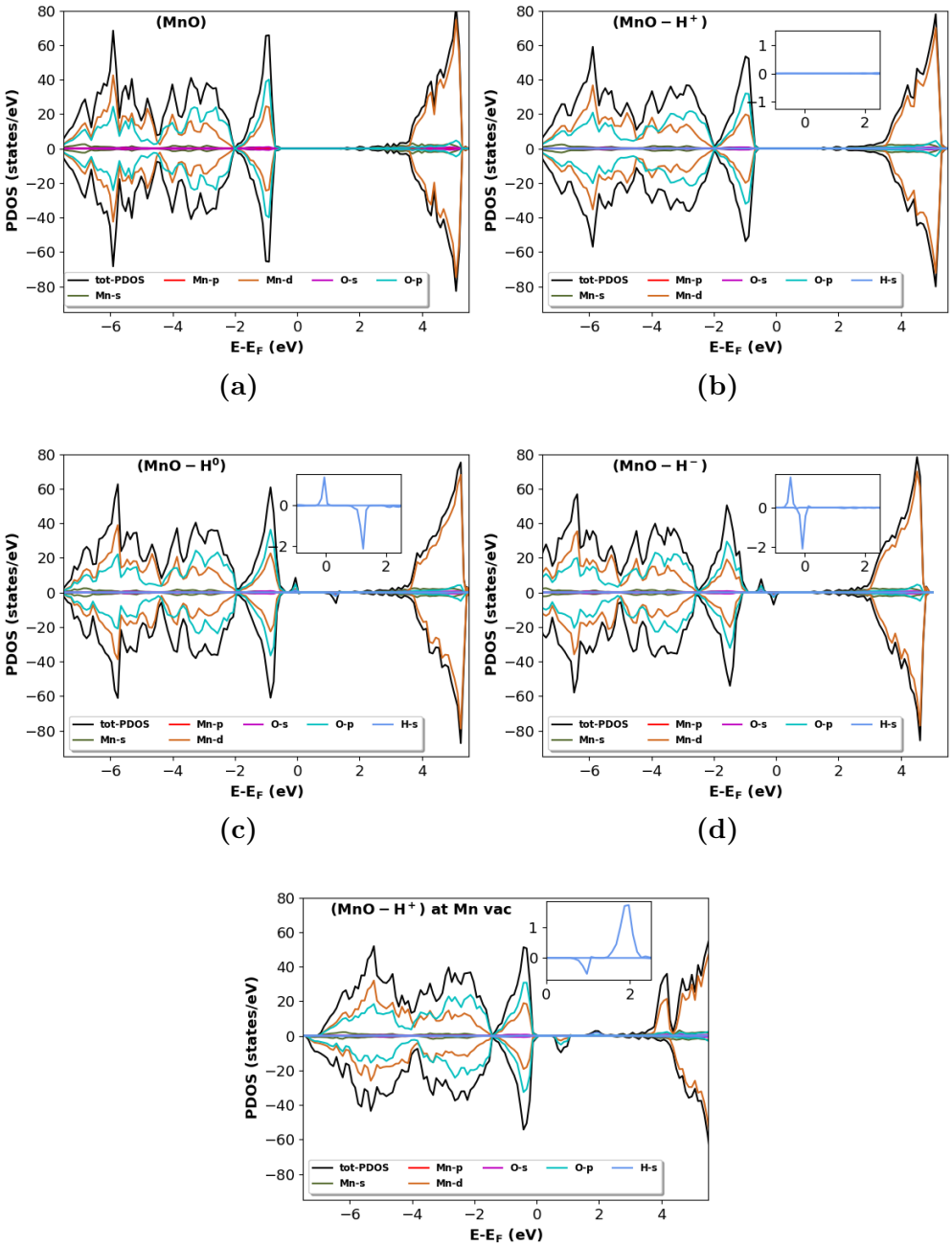

Figure 7.3: The projected density of states (PDOS) on each of the atomic orbital of (a) MnO (b) MnO with H^+ impurity (c) MnO with H^0 impurity (d) MnO with H^- impurity (e) MnO with H^+ impurity at Mn vacancy site. The Fermi energy has been scaled to 0 eV. The insets are of the projection on the hydrogen orbital, showing its behaviour in the vicinity of the band gap.

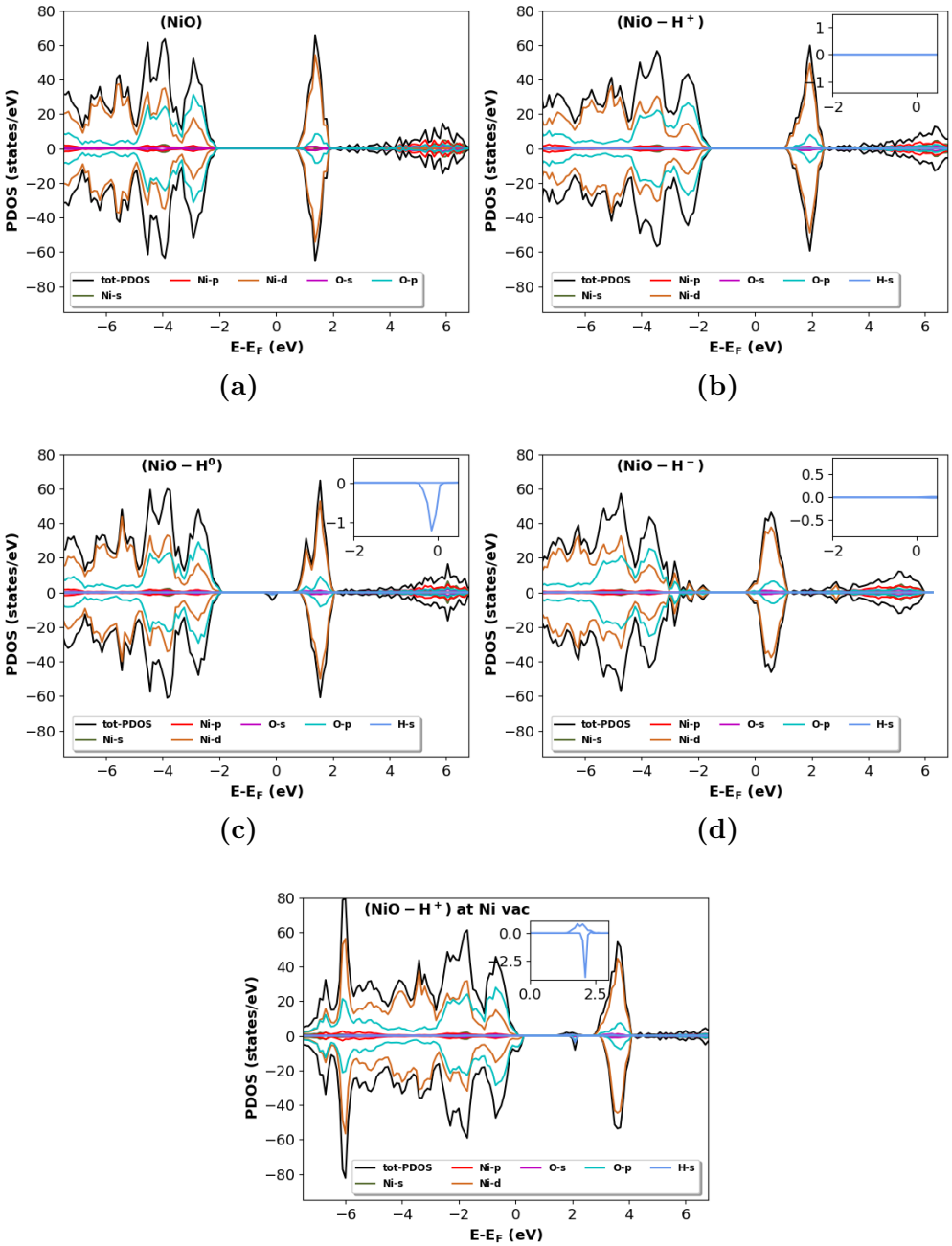

Figure 7.4: The projected density of states (PDOS) on each of the atomic orbital of (a) NiO (b) NiO with H^+ impurity (c) NiO with H^0 impurity (d) NiO with H^- impurity (e) NiO with H^+ impurity at Mn vacancy site. The Fermi energy has been scaled to 0 eV. The insets are of the projection on the hydrogen orbital, showing its behaviour in the vicinity of the band gap.

description of electron correlation. Thus, most of the local minima sites shown in Fig. 7.2 were not found with the standard DFT. For example the O-H-O site was not found as a minimum energy site and also the O-H site was uncovered with bond lengths of 0.5 Å, very small to allow localization of the O and H atoms considering the atomic radius.

Furthermore, since earlier studies on TMMO have reported possibilities of cation vacancy complexes, calculations for the charged hydrogen interstitial at a Mn^{2+} or Ni^{2+} vacancy site were performed. Even though, these impurities introduce the defect levels in the band gap (See Fig. 7.3e and 7.4e), they have large formation energies when compared to other void interstitial hydrogen states. Hence, the emphasis in this study is on the interstitial hydrogen states.

Figs. 7.3 and 7.4 show the plot of the projected density of states (PDOS) for each of the atomic orbitals in MnO and NiO for the lowest energy structure for each of the charged states. The gaps (Figs. 7.3c and 7.3d) obtained by DFT+U in MnO and NiO are consistent with previous studies [243, 245, 246] and the insets zooms in the gap region to highlight possible hydrogen related in-gap states.The neutral and negatively charged hydrogen defects introduce localized defect levels in the band gap for MnO (Figs. 7.3c and 7.3d). This is also the case for the H^+ impurity at an Mn vacancy site, Fig. 7.3e. However, for NiO the effect of the negatively charge hydrogen defect is to shift closer to the Fermi level the valence band maximum (VBM) and conduction band minimum (CBM) (see Fig. 7.4d) while the neutral charged and H^+ at Ni vacancy site introduce defect levels at the band gap (see Figs. 7.4c and 7.4e). The observed emergence of hydrogen states in the band gap is expected to provide mechanism for enhancing electrical conductivity and optical properties of the wide band gap insulators, MnO and NiO.

7.3 Stability of defect states

The stability of the hydrogen defect states is studied by calculating the formation energies and understanding the behaviour in the band gap. The formation energy E_{fm} for each of the defect states in the supercell is evaluated using the relation [247];

$$E_{fm} = E(H^q) - E(bulk) - \frac{1}{2}E(H_2) + q(E_F + E_{VBM}) \tag{7.1}$$

where $E(H^q)$ and $E(bulk)$ are the DFT total energy of the supercell with the hydrogen q charged defect and bulk supercell respectively. $E(H_2)$ is the energy of hydrogen molecule at T= 0 [248], this is used as the reference energy for hydrogen. E_f is the Fermi energy referenced to the valence band maximum (VBM). The

electrostatic correction on the formation energy due to the use of compensating charge to avoid the divergence of the systems electrostatic energy when a charged supercell is considered, is neglected. The supercell used was considered to be large enough, such that this correction vanishes and can be neglected.

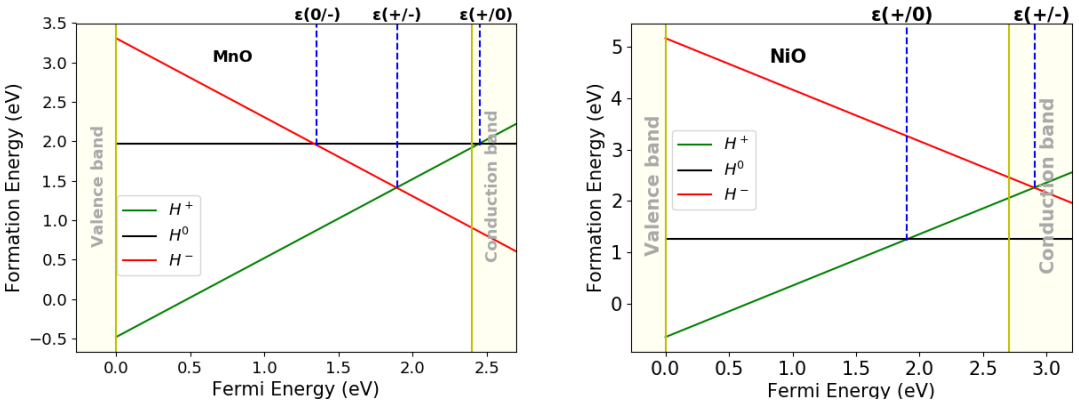

Figure 7.5: Formation energy of different charged states vs Fermi Energy referenced to the VBM for (a) MnO and (b) NiO.

Fig. 7.5 shows the plot of the formation energy and the behaviour of the defect states within the band gap, in the vicinity of the Fermi level. The plot allows to understand the stability of the different defect charged states. For each of the charged defect state of MnO and NiO, the lowest energy defect structure (see Fig. 7.2) was consdered for the plot in Fig. 7.5. In the same figure, the transition levels $\epsilon(0/-)$, $\epsilon(+/-)$ and $\epsilon(+/0)$ represent the point in the band gap where the formation energies of two different hydrogen charged states are equal. The position of these transition levels in the formation energy plot are important for describing the hydrogen defect behaviour. [247, 249, 250]

For MnO (Fig. 7.5a), the transition level, $\epsilon(+/-)$ between negative and positive charged defect is at 1.9 eV within the Fermi energy, such that below 1.9 eV and closer to the VBM the H^+ is the preferred stable hydrogen defect while the H^- is preferred above 1.9 eV. This indicates that hydrogen in MnO is amphoteric, i.e accommodates both the positive and negative charged states. This behaviour is common among many semiconductors and insulators including GaN. [247, 249, 250] Notice that the neutral state is never predicted as the most stable, in agreement with experiment, and that the negatively charged state is expected only in heavily n-doped MnO.

The behaviour of hydrogen is quite different for NiO. From Fig. 7.5b, the transition level $\epsilon(+/-)$ occurs inside the conduction band above the CBM, such that

within the band gap, the H^+ defect always has the lowest formation energy than H^-. This suggests that for NiO, the electron donor defect state H^+ of hydrogen is preferred and hydrogen in NiO acts like a shallow donor. This behaviour is similar to that of ZnO and InN. [247, 249, 250]

7.4 μSR and calculated muon dipolar coupling

To account for the zero temperature muon precession frequency of 155 MHz in MnO and 61.3 MHz in NiO from the positive ZF-μSR measurements already reported in Refs. [22] and [239] respectively, the muon implantation sites in both compounds were studied. Both materials are antiferromagnets, so that the observed ZF frequency is directly proportional to the muon local field ($\nu = \frac{\gamma B_\mu}{2\pi}$ Sec. 2.4.3). Since the muon is treated as an analogue of hydrogen in DFT calculations, the possible muon stopping sites were considered to be the same as the minima energy sites of only the positively charged states (H^+) of hydrogen discussed above and shown in Fig. 7.2 with labels A, B and C for both MnO and NiO.

The A site requires an additional discussion. There are four sites A, that are crystallographically equivalent and bond with an oxygen atom. The distance among any pair of sites is only 1.1 Å. In the following we assume that the muon in site A is tunneling among these four replica sites and the field measured by μSR is the average of the four. This could be checked by lengthy calculations of the total DFT energy profile around oxygen, a task beyond the present scope.

The contact field has been calculated for both materials and its contribution to the muon precession frequency is in the range -12 MHz to 6 MHz, negligible in comparison with the experimental local field at the muon, in view of the remaining numerical and experimental uncertainties. Therefore from now on we neglect it and consider only dipolar sums.

The dipolar contribution to the local field at the muon is calculated for the different DFT energy minima sites. The absolute value of the Mn and Ni moment used for the dipolar field calculations are 4.58 μ_B and 1.9 μ_B respectively. [241] More recent measurements from powder diffraction report a large value of 5.65 μ_B [251] for MnO, not commenting on the discrepancy. The older paper agrees better with DFT+U calculations (this is significant in 3D insulators, unlike in magnetic metals and in low dimensional system, where DFT systematically overestimates the moment size). For this reason we adopt the values reported in Ref. [241].

The AF magnetic orders already described in Sec. 7.1 were adopted for both MnO and NiO. The magnetic moment has been reported [252] to be aligned in the $[11\overline{2}]$ and its equivalent directions for MnO. I performed dipolar calculations for the

moment aligned in different directions within the (111) family of directions [240], in order to check the actual alignment by comparing the results with the μSR data. The moments are aligned parallel and anti-parallel to each of the directions.

Table 7.1: Calculated dipolar contributions to the frequency ν_{dip} in MHz for the magnetic moment aligned in different direction of the muon at site A, B and C in MnO and NiO. ν_{μ}^{exp} is the ZF-μSR measured value.

		ν_{dip} [a]				
	Site	[111]	[$\bar{1}$10]	[112]	[11$\bar{2}$]	ν_{μ}^{exp} [a]
MnO	A [b]	302.89	215.52	271.77	186.52	155.5 [22]
	B [b]	243.51	319.50	319.77	227.87	
	C	370.29	185.15	354.52	185.14	
NiO	A [b]	156.929	109.67	140.73	93.64	61.3 [239]
	B [b]	121.195	159.03	159.16	113.41	
	C	184.30	92.15	176.45	92.15	

[a] Units in MHz.
[b] Calculated ν_{dip} at this site are averaged over muon assumed to hop between equivalent sites

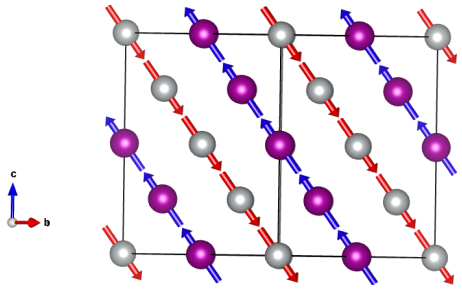

Figure 7.6: Supercell showing the (11$\bar{2}$) axis of the magnetic moment on the cations.

Table 7.1 shows the result of dipolar sums for the three candidate sites and a few significant directions of the moment, compared with the measured values, for both materials.

The smallest value for site A is with the moment along [11$\bar{2}$], the known experimental direction for MnO. A very similar result is obtained for site C in the same conditions, although site C reproduces the same minimum value also for moments along [$\bar{1}$10].

I conclude that site A is the stable site in both material because DFT+U calculations show (Fig. 7.2) that its total energy is 1.5 (1.0) eV lower for MnO

(NiO), a significant difference. Therefore, DFT assisted μSR results confirm the known alignment of the moment in MnO and demonstrate that the same alignment along $[11\bar{2}]$ holds true for NiO. Fig. 7.6 shows the representation of the magnetic moment aligned in the $(11\bar{2})$ direction for MnO or NiO supercell.

In the remaining part of this section I give further details on the site analysis, beside these main conclusions.

If the tunneling model were not assumed for site A, this site would produce four rather high frequencies in the muon spectrum, in contrast with experimental observation. Since site A is strongly supported by quite accurate DFT energy calculations we assume the tunneling model without further checks. The tunneling model yields an overestimation by 20% in MnO and by 50% in NiO. This could be partly corrected by a contact contribution.

At site B, the muon forms an $O-\mu-O$ bond. For site B, the equivalent sites are a bit farther apart with distances in the range of 1.57 Å for MnO and 1.47 Å for NiO. In this configuration, similar to that of the F-μ-F center in fluorides [62], the muon may diffuse at higher temperatures, but is highly unlikely to tunnel at low temperatures.

At site C, the muon is at the body center position. The muon field is same for the crystallographic equivalent positions of this site. No quantum tunneling can be envisaged for this site.

Furthermore, no evidence of the muon hopping from one site to another has been reported yet for the ground state measurement of these materials. Also hopping and barrier calculations for these site has not been considered yet.

Finally, earlier work suggested different assignments. The C site was indicated in Ref. [22] on the basis of paramagnetic shift measurements [21]. This is perhaps borderline to our discussion. The same site was assumed by comparison with dipolar field distribution calculations [253] and this would agree with the analysis presented here, but the DFT total energy is quite a strong argument for site A with tunneling.

7.5 Conclusion

With DFT+U, hydrogen defects and muon sites in MnO and NiO have been discussed. The effects of electron correlation are observed to be crucial for site localization. Thus reproducing the band gap and insulating behaviour is crucial for defect studies in these wide band gap insulating materials. The localization site of the neutral, positively and negatively charged hydrogen defect states has been investigated for MnO and NiO. The neutral and negatively charged hydrogen states introduce in gap defect states in the wide band gap for MnO. For NiO, it is the neutral state that introduces in gap defect states at the band gap while

the negatively charged impurity modifies and bring closer the VBM and CBM. Also, the less stable positively charged hydrogen defect at the cation (Mn^{2+} or Ni^{2+}) vacancy position introduces in-gap defect states in the band gap. These observed defect levels are expected to be of relevance in the emergence of interesting electrical, optical and thermodynamic properties. Further study of the formation energies suggests that hydrogen exists as amphoteric defect in MnO and as a shallow donor in NiO.

The possible muon implantation sites in MnO and NiO have been determined and by dipolar simulations and comparison with the measured precession frequency, the magnetic moments were confirmed to align in the $[11\overline{2}]$ direction for MnO and NiO.

8

Summary and Conclusion

In this thesis, I have discussed the computational approach within density functional electronic theory method for the determination of the muon implantation site and its Fermi-contact hyperfine coupling. In μSR, the muon implantation site is important because in some cases it allows for completeness in the analysis of experimental data. Also the knowledge of the muon implantation site and the effects of the muon in the sample, made available by the computational methods, allow to explain some of the observed phenomenon from μSR measurements. The muon implantation site(s) has been successfully determined in a range of selected magnetic and superconducting materials, especially those of current interest due to the intriguing properties they exhibit, especially when subjected to temperature, pressure and chemical doping variations. Furthermore, the muon site calculation approaches discussed in this thesis allowed to understand and explain the effect and the extent of perturbation introduced in the sample by the implanted muon. This is also important to ascertain how intrinsic are the measured properties in these materials.

Particularly, the muon implantation sites have been calculated in $NaFe_{1-x}Ni_xAs$, where by μSR measurements the coexistence of magnetism and superconductivity has been observed. Three muon implantation sites were found both in the parent compound and in Ni doped samples by DFT calculations and using further stability analysis calculations. The calculated sites are consistent with the three muon precession frequencies observed in ZF-μSR measurements. By dipolar calculations at the muon sites and comparing with the measured frequencies, the magnetic moment size was determined. This was found to be consistent with the value obtained by other experimental methods including neutron scattering and Mössbauer.

The muon implantation site has been calculated in $Yb_2Pd_2In_{1-x}Sn_x$. μSR measurements and results for this compound under hydrostatic pressure were also presented. In $Yb_2Pd_2In_{1-x}Sn_x$, with μSR measurements, a steep change in the local field at the muon has been observed by doping with Sn and by applying hydrostatic pressure above 10 kbar. The calculated muon site together with dipolar field calculations allowed to explain the origin of the pressure induced changes. The

origin of the steep change in the measured muon local field is due to a possible reordering of the Yb moments thus a transition from the AF magnetic order.

Also in Sr_2RuO_4, the muon implantation site has been determined and the extent of the perturbation due to the muon in the sample and subsequent effects of the perturbation on the density of states have been discussed. Sr_2RuO_4 is a non-copper layered superconductor, where in the mechanism that drives superconductivity, time reversal symmetry breaking has been observed by spontaneous magnetization measured with μSR. However this particular effect has not been observed by other scanning probe methods. The study of the perturbation of the muon shows no appreciable change in the density of state distribution even though the muon distorts the neighbour host ions from their equilibrium positions. Our calculations so far suggest that the implanted muon does not influence the intrinsic properties of this material. However, further studies are required especially the inclusion of the spin-orbit couplings since it has been shown to be important for the correct description of the Fermi surface of Sr_2RuO_4. Although this is expected not to influence the muon localization site, it is important to understand the effect of the muon together with those of spin-orbit interaction in Sr_2RuO_4.

Also, to understand the coupling of the muon with the host electrons, we have described an approach that makes use of the core reconstruction with the projector augmented wave method to successfully calculate the muon Fermi-contact hyperfine interactions. These calculations were performed on metals, first with a benchmark of the approach on the elemental transition metals of Fe, Co and Ni and further on MnSi and MnGe, two samples of current interest for the study and possible observance of Skyrmion physics.

The calculations involving the muon within the available theoretical approximation is far from trivial considering that the light mass of the muon and its subsequent high amplitude zero point vibrations at the implantation site. The treatment of the muon as a point defect within the conventional DFT approach does not take into account the effect of the muon zero point vibration. To account for these vibrations, the self-consistent stochastic harmonic approximation (SSCHA) has been described. With the SSCHA approach the effect of the muon mass was successfully included in the calculation of the contact hyperfine field in metals. This also allowed to discuss the preferred octahedral or tetrahedral implantation site of the muon in Fe. With the inclusion of the quantum effect of the muon, there is better agreement between the calculated Fermi contact hyperfine field and the experimental results.

Finally, hydrogen defect sites and muon coupling parameters where studied in the antiferromagnetically ordered transition metal mono-oxide (TMMO) of MnO and NiO. Both the neutral and charged hydrogen defects where considered. The minima energy localization sites of these defects were determined. The hydrogen

defects where observed to introduce defects levels in the band gap which are important for enhancing electrical conductivity and optical properties of the TMMO. Further study of the stability of the defects revealed that hydrogen can exist as an amphoteric defect in MnO and as a shallow donor in NiO. With the established defects localization site, the muon dipolar coupling were calculated of which with comparison with the already measured zero temperature muon fields, the magnetic moments were confirmed to align in the $(11\overline{2})$ direction.

Bibliography

[1] A. Schenck and F. GYGAX, "Magnetic materials studied by muon spin rotation," in *Handbook of Magnetic Materials*, Vol. 9, edited by K.H.J.Buschow (Elsevier Science B.V., Netherlands, 1995) pp. 60–284.

[2] Y. J. Uemura, "μSR relaxation functions in magnetic materials," in *MUON SCIENCE - Muons in Physics, Chemistry and Materials*, edited by S. L. Lee, S. H. Kilcoyne, R. Cywinski, and P. Osborne (SUSSP Publications and Institute of Physics Publishing, Scotland & USA, 1999) p. 85.

[3] S. J. Blundell, "Spin-polarized muons in condensed matter physics," Contemporary Physics **40**, 175–192 (1999).

[4] A. Yaouanc and P. Dalmas de Réotier, *Muon Spin Rotation Relaxation and Resonance: Applications to Condensed Matter* (Oxford University Press, Oxford, 2011).

[5] S. H. Neddermeyer and C. D. Anderson, "Note on the nature of cosmic-ray particles," Phys. Rev. **51**, 884–886 (1937).

[6] T. D. Lee and C. N. Yang, "Question of parity conservation in weak interactions," Phys. Rev. **104**, 254–258 (1956).

[7] R. L. Garwin, L. M. Lederman, and M. Weinrich, "Observations of the failure of conservation of parity and charge conjugation in meson decays: the magnetic moment of the free muon," Phys. Rev. **105**, 1415–1417 (1957).

[8] S. F. J. Cox, "Muonium as a model for interstitial hydrogen in the semiconducting and semimetallic elements," Reports on Progress in Physics **72**, 116501 (2009).

[9] P. W. Percival, B. Addison-Jones, J.-C. Brodovitch, F. Ji, P. J. Horoyski, M. L. Thewalt, and T. R. Anthony, "13C hyperfine coupling constants in MuC60," Chemical Physics Letters **245**, 90 – 94 (1995).

[10] M. J. Graf, J. Lago, A. Lascialfari, A. Amato, C. Baines, S. R. Giblin, J. S. Lord, A. M. Tkachuk, and B. Barbara, "Muon spin rotation studies of spin dynamics at avoided level crossings in $LiY_{0.998}Ho_{0.002}F_4$," Phys. Rev. Lett. **99**, 267203 (2007).

[11] B. E. Schultz, K. H. Chow, B. Hitti, R. F. Kiefl, R. L. Lichti, and S. F. J. Cox, "Local structure of isolated positively charged muonium as an analog for the hydrogen ion in p-type GaAs," Phys. Rev. Lett. **95**, 086404 (2005).

[12] R. F. Kiefl, M. Celio, T. L. Estle, G. M. Luke, S. R. Kreitzman, J. H. Brewer, D. R. Noakes, E. J. Ansaldo, and K. Nishiyama, "Determination of the electronic structure of anomalous muonium in GaAs from nuclear hyperfine interactions," Phys. Rev. Lett. **58**, 1780–1783 (1987).

[13] R. Kubo and T. Toyabe, "Magnetic resonance and relaxation," in *Magnetic Resonance and relaxation:*, edited by R. Blinc (North-holland, Amsterdam, 1967) p. 810.

[14] F. L. Pratt, "Field dependence of μSR signals in a polycrystalline magnet," Journal of Physics: Condensed Matter **19**, 456207 (2007).

[15] A.Abragam, *The principles of nuclear magnetism* (Oxford University press, Amen House, London, 1961) see chapter VI.

[16] H. A. Lorentz, "The theory of electrons and its applications to the phenomena of light and radiant heat," in *A Course of Lectures Delivered in Columbia University*, edited by R. Blinc (Columbia University Press, New York, 1909) p. 133.

[17] P. Bonfà, I. J. Onuorah, and R. De Renzi, "Introduction and a quick look at MUESR, the magnetic structure and muon embedding site refinement suite," in *Proceedings of the 14th International Conference on Muon Spin Rotation, Relaxation and Resonance (μSR2017)*, JPS Conf. Proc., Vol. 21 (The Physical Society of Japan, 2018) p. 011052.

[18] A. Schenck, "Static magnetic properties of metallic systems," in *MUON SCIENCE - Muons in Physics, Chemistry and Materials*, edited by S. L. Lee, S. H. Kilcoyne, R. Cywinski, and P. Osborne (SUSSP Publications and Institute of Physics Publishing, Scotland I& USA, 1999) pp. 39–84.

[19] P. Jena, "Electronic structure of hydrogen-like impurities in nearly-free-electron metals," Hyperfine interactions **6**, 5–14 (1979).

[20] M. M. J.Rath, P.Jena, and C. Wang, "Effect of zero point motion on the hyperfine field at an interstitial positive muon site in ferromagnetic Ni," Solid State Communications **31**, 1003–1007 (1979).

[21] Y. J. Uemura, J. Imazato, N. Nishida, R. S. Hayano, M. Takigawa, and T. Yamazaki, "Paramagnetic shift of μ^+ in MnO and its time dependence," Hyperfine Interactions **8**, 725–728 (1981).

[22] Y. J. Uemura, T. Yamazaki, Y. Kitaoka, M. Takigawa, and H. Yasuoka, "Positive muon spin precession in magnetic oxides MnO and V_2O_3 local fields and phase transition," Hyperfine Interactions **17**, 339–343 (1984).

[23] M. Born and R. Oppenheimer, "Zur quantentheorie der molekeln," Annalen der Physik **84**, 457–484 (1927).

[24] V. Fock, "Näherungsmethode zur Lösung des quantenmechanischen Mehrkörperproblems," Zeitschrift für Physik **61**, 126–148 (1930).

[25] D. R. Hartree, "The calculation of atomic structures," Reports on Progress in Physics **11**, 113 (1947).

[26] J. C. Slater, "A Simplification of the Hartree-Fock Method," Phys. Rev. **81**, 385–390 (1951).

[27] W. Kohn and L. J. Sham, "Self-consistent equations including exchange and correlation effects," Phys. Rev. **140**, A1133–A1138 (1965).

[28] J. P. Perdew and A. Zunger, "Self-interaction correction to density-functional approximations for many-electron systems," Phys. Rev. B **23**, 5048–5079 (1981).

[29] J. P. Perdew and Y. Wang, "Accurate and simple analytic representation of the electron-gas correlation energy," Phys. Rev. B **45**, 13244–13249 (1992).

[30] J. P. Perdew, K. Burke, and M. Ernzerhof, "Generalized gradient approximation made simple," Phys. Rev. Lett. **77**, 3865–3868 (1996).

[31] C. Lee, W. Yang, and R. G. Parr, "Development of the colle-salvetti correlation-energy formula into a functional of the electron density," Phys. Rev. B **37**, 785–789 (1988).

[32] A. D. Becke, "Density-functional exchange-energy approximation with correct asymptotic behavior," Phys. Rev. A **38**, 3098–3100 (1988).

[33] V. I. Anisimov, J. Zaanen, and O. K. Andersen, "Band theory and mott insulators: Hubbard U instead of stoner I," Phys. Rev. B **44**, 943–954 (1991).

[34] A. I. Liechtenstein, V. I. Anisimov, and J. Zaanen, "Density-functional theory and strong interactions: Orbital ordering in Mott-Hubbard insulators," Phys. Rev. B **52**, R5467–R5470 (1995).

[35] V. I. Anisimov, F. Aryasetiawan, and A. I. Lichtenstein, "First-principles calculations of the electronic structure and spectra of strongly correlated systems: the LDA + U method," Journal of Physics: Condensed Matter **9**, 767 (1997).

[36] M. Cococcioni and S. de Gironcoli, "Linear response approach to the calculation of the effective interaction parameters in the LDA + U method," Phys. Rev. B **71**, 035105 (2005).

[37] H. J. Kulik, M. Cococcioni, D. A. Scherlis, and N. Marzari, "Density Functional Theory in Transition-Metal Chemistry: A Self-Consistent Hubbard U Approach," Phys. Rev. Lett. **97**, 103001 (2006).

[38] H. J. Monkhorst and J. D. Pack, "Special points for brillouin-zone integrations," Phys. Rev. B **13**, 5188–5192 (1976).

[39] N. Marzari, D. Vanderbilt, A. De Vita, and M. C. Payne, "Thermal contraction and disordering of the Al(110) surface," Phys. Rev. Lett. **82**, 3296–3299 (1999).

[40] C. G. Van de Walle, P. J. H. Dentener, Y. Bar-Yam, and S. T. Pantelides, "Theory of hydrogen diffusion and reactions in crystalline silicon," Phys. Rev. B **39**, 10791–10808 (1989).

[41] C. G. Van de Walle, "Structural identification of hydrogen and muonium centers in silicon: First-principles calculations of hyperfine parameters," Phys. Rev. Lett. **64**, 669–672 (1990).

[42] C. G. Van de Walle and P. Blóchl, "First-principles calculations of hyperfine parameters," Phys. Rev. B **47**, 4244–4255 (1993).

[43] P. E. Blöchl, "Projector augmented-wave method," Phys. Rev. B **50**, 17953–17979 (1994).

[44] J. M. Rondinelli, B. Deng, and L. D. Marks, "Enhancing structure relaxations for first-principles codes: An approximate hessian approach," Computational Materials Science **40**, 345 – 353 (2007).

[45] R. P. Feynman, "Forces in molecules," Phys. Rev. **56**, 340–343 (1939).

[46] P. Giannozzi, S. Baroni, N. Bonini, M. Calandra, R. Car, C. Cavazzoni, D. Ceresoli, G. L. Chiarotti, M. Cococcioni, I. Dabo, A. Dal Corso, S. de Gironcoli, S. Fabris, G. Fratesi, R. Gebauer, U. Gerstmann, C. Gougoussis, A. Kokalj, M. Lazzeri, L. Martin-Samos, N. Marzari, F. Mauri, R. Mazzarello, S. Paolini, A. Pasquarello, L. Paulatto, C. Sbraccia,

S. Scandolo, G. Sclauzero, A. P. Seitsonen, A. Smogunov, P. Umari, and R. M. Wentzcovitch, "QUANTUM ESPRESSO: a modular and open-source software project for quantum simulations of materials," Journal of Physics: Condensed Matter **21**, 395502 (19pp) (2009).

[47] R. De Renzi, P. Bonfá, M. Mazzani, S. Sanna, G. Prando, P. Carretta, R. Khasanov, A. Amato, H. Luetkens, M. Bendele, F. Bernardini, S. Massidda, A. Palenzona, M. Tropeano, and M. Vignolo, "Effect of external pressure on the magnetic properties of LnFeAsO (Ln = La, Ce, Pr, Sm)," Superconductor Science and Technology **25**, 084009 (2012).

[48] G. Prando, P. Bonfà, G. Profeta, R. Khasanov, F. Bernardini, M. Mazzani, E. M. Brüning, A. Pal, V. P. S. Awana, H.-J. Grafe, B. Büchner, R. De Renzi, P. Carretta, and S. Sanna, "Common effect of chemical and external pressures on the magnetic properties of RCoPO (R = La, Pr)," Phys. Rev. B **87**, 064401 (2013).

[49] H. Maeter, H. Luetkens, Y. G. Pashkevich, A. Kwadrin, R. Khasanov, A. Amato, A. A. Gusev, K. V. Lamonova, D. A. Chervinskii, R. Klingeler, C. Hess, G. Behr, B. Büchner, and H.-H. Klauss, "Interplay of rare earth and iron magnetism in RFeAsO (R = La, Ce, Pr, and Sm): Muon-spin relaxation study and symmetry analysis," Phys. Rev. B **80**, 094524 (2009).

[50] M. Bendele, A. Ichsanow, Y. Pashkevich, L. Keller, T. Strässle, A. Gusev, E. Pomjakushina, K. Conder, R. Khasanov, and H. Keller, "Coexistence of superconductivity and magnetism in $FeSe_{1-x}$ under pressure," Phys. Rev. B **85**, 064517 (2012).

[51] J. Sugiyama, H. Nozaki, I. Umegaki, M. Harada, Y. Higuchi, K. Miwa, E. J. Ansaldo, J. H. Brewer, M. Imai, C. Michioka, K. Yoshimura, and M. Månsson, "Variation of magnetic ground state of $Sr_{1-x}Ca_xCo_2P_2$ determined with μ^+SR," Phys. Rev. B **91**, 144423 (2015).

[52] E. L. Silva, A. G. Marinopoulos, R. C. Vilão, R. B. L. Vieira, H. V. Alberto, J. Piroto Duarte, and J. M. Gil, "Hydrogen impurity in yttria: Ab initio and μSR perspectives," Phys. Rev. B **85**, 165211 (2012).

[53] R. C. Vilão, A. G. Marinopoulos, R. B. L. Vieira, A. Weidinger, H. V. Alberto, J. P. Duarte, J. M. Gil, J. S. Lord, and S. F. J. Cox, "Hydrogen impurity in paratellurite α-TeO_2: Muon-spin rotation and *ab initio* studies," Phys. Rev. B **84**, 045201 (2011).

[54] C. G. Van de Walle, "Hydrogen as a cause of doping in zinc oxide," Phys. Rev. Lett. **85**, 1012–1015 (2000).

[55] H. Suter, E. Stoll, and P. Meier, "Muon sites and hyperfine fields in La_2CuO_4," Physica B: Condensed Matter **326**, 329 – 332 (2003).

[56] P. Bonfà, F. Sartori, and R. De Renzi, "Efficient and reliable strategy for identifying muon sites based on the double adiabatic approximation," The Journal of Physical Chemistry C **119**, 4278–4285 (2015).

[57] A. Amato, P. Dalmas de Réotier, D. Andreica, A. Yaouanc, A. Suter, G. Lapertot, I. M. Pop, E. Morenzoni, P. Bonfà, F. Bernardini, and R. De Renzi, "Understanding the μSR spectra of MnSi without magnetic polarons," Phys. Rev. B **89**, 184425 (2014).

[58] N. Martin, M. Deutsch, F. Bert, D. Andreica, A. Amato, P. Bonfà, R. De Renzi, U. K. Rößler, P. Bonville, L. N. Fomicheva, A. V. Tsvyashchenko, and I. Mirebeau, "Magnetic ground state and spin fluctuations in MnGe chiral magnet as studied by muon spin rotation," Phys. Rev. B **93**, 174405 (2016).

[59] R. Khasanov, A. Amato, P. Bonfà, Z. Guguchia, H. Luetkens, E. Morenzoni, R. De Renzi, and N. D. Zhigadlo, "High-pressure magnetic state of MnP probed by means of muon-spin rotation," Phys. Rev. B **93**, 180509 (2016).

[60] F. K. K. Kirschner, R. D. Johnson, F. Lang, D. D. Khalyavin, P. Manuel, T. Lancaster, D. Prabhakaran, and S. J. Blundell, "Spin Jahn-Teller antiferromagnetism in $CoTi_2O_5$," ArXiv e-prints (2018).

[61] F.Bernardini, P.Bonfà, S. Massidda, and R. De Renzi, "Ab initio strategy for muon site assignment in wide band gap fluorides," Phys. Rev. B **87**, 115148 (2013).

[62] J. S. Möller, D. Ceresoli, T. Lancaster, N. Marzari, and S. J. Blundell, "Quantum states of muons in fluorides," Phys. Rev. B **87**, 121108 (2013).

[63] J. H. Brewer and R. Cywinski, "μSR: an introduction," in *MUON SCIENCE - Muons in Physics, Chemistry and Materials*, edited by S. L. Lee, S. H. Kilcoyne, R. Cywinski, and P. Osborne (SUSSP Publications and Institute of Physics Publishing, Scotland & USA, 1999) pp. 1–10.

[64] F. R. Foronda, F. Lang, J. S. Möller, T. Lancaster, A. T. Boothroyd, F. L. Pratt, S. R. Giblin, D. Prabhakaran, and S. J. Blundell, "Anisotropic Local Modification of Crystal Field Levels in Pr-Based Pyrochlores: A Muon-Induced Effect Modeled Using Density Functional Theory," Phys. Rev. Lett. **114**, 017602 (2015).

[65] J. S. Möller, P. Bonfà, D. Ceresoli, F. Bernardini, S. J. Blundell, T. Lancaster, R. De Renzi, N. Marzari, I. Watanabe, S. Sulaiman, and M. I. Mohamed-Ibrahim, "Playing quantum hide-and-seek with the muon: localizing muon stopping sites," Physica Scripta **88**, 068510 (2013).

[66] P. Bonfà and R. De Renzi, "Toward the computational prediction of muon sites and interaction parameters," J. Phys. Soc. Jpn **85**, 091014 (2016).

[67] K. Momma and F. Izumi, "*VESTA*: a three-dimensional visualization system for electronic and structural analysis," Journal of Applied Crystallography **41**, 653–658 (2008).

[68] G. R. Stewart, "Superconductivity in iron compounds," Rev. Mod. Phys. **83**, 1589–1652 (2011).

[69] D. J. Scalapino, "A common thread: The pairing interaction for unconventional superconductors," Rev. Mod. Phys. **84**, 1383–1417 (2012).

[70] P. Dai, "Antiferromagnetic order and spin dynamics in iron-based superconductors," Rev. Mod. Phys. **87**, 855–896 (2015).

[71] Y. J. Uemura, "Superconductivity: Commonalities in phase and mode." Nature materials **8 4**, 253–5 (2009).

[72] S. Nandi, M. G. Kim, A. Kreyssig, R. M. Fernandes, D. K. Pratt, A. Thaler, N. Ni, S. L. Bud'ko, P. C. Canfield, J. Schmalian, R. J. McQueeney, and A. I. Goldman, "Anomalous suppression of the orthorhombic lattice distortion in superconducting $Ba(Fe_{1-x}Co_x)_2As_2$ single crystals," Phys. Rev. Lett. **104**, 057006 (2010).

[73] E. P. Rosenthal, E. F. Andrade, C. J. Arguello, R. M. Fernandes, L. Y. Xing, X. C. Wang, C. Q. Jin, A. J. Millis, and A. N. Pasupathy, "Visualization of electron nematicity and unidirectional antiferroic fluctuations at high temperatures in NaFeAs," Nature Physics **10**, 225–232 (2014).

[74] M. Yi, D. Lu, J.-H. Chu, J. G. Analytis, A. P. Sorini, A. F. Kemper, B. Moritz, S.-K. Mo, R. G. Moore, M. Hashimoto, W.-S. Lee, Z. Hussain, T. P. Devereaux, I. R. Fisher, and Z.-X. Shen, "Symmetry-breaking orbital anisotropy observed for detwinned $Ba(Fe_{1-x}Co_x)_2As_2$ above the spin density wave transition," Proceedings of the National Academy of Sciences **108**, 6878–6883 (2011).

[75] R. M. Fernandes, A. V. Chubukov, and J. Schmalian, "What drives nematic order in iron-based superconductors?" Nature Physics **10**, 97–104 (2014).

[76] W. Wang, Y. Song, C. Cao, L. Yu, H. Leland, T. Wei, C. Songxue, Y. Klauss, Rong, N. Andriy, and D. Pengcheng, "Intertwined superconducting and nematic orders in $NaFe_{1-x}Ni_xAs$ without antiferromagnetic order," Bull. Am. Phys. Soc. **62**, R39.00010 (2017).

[77] S. Li, C. de la Cruz, Q. Huang, G. F. Chen, T.-L. Xia, J. L. Luo, N. L. Wang, and P. Dai, "Structural and magnetic phase transitions in $Na_{1-\delta}FeAs$," Phys. Rev. B **80**, 020504 (2009).

[78] T. Goltz, V. Zinth, D. Johrendt, H. Rosner, G. Pascua, H. Luetkens, P. Materne, and H.-H. Klauss, "Microscopic coexistence of magnetism and superconductivity in charge-compensated $Ba_{1-x}K_x(Fe_{1-y}Co_y)_2As_2$," Phys. Rev. B **89**, 144511 (2014).

[79] D. W. Tam, Y. Song, H. Man, S. C. Cheung, Z. Yin, X. Lu, W. Wang, B. A. Frandsen, L. Liu, Z. Gong, T. U. Ito, Y. Cai, M. N. Wilson, S. Guo, K. Koshiishi, W. Tian, B. Hitti, A. Ivanov, Y. Zhao, J. W. Lynn, G. M. Luke, T. Berlijn, T. A. Maier, Y. J. Uemura, and P. Dai, "Uniaxial pressure effect on the magnetic ordered moment and transition temperatures in $BaFe_{2-x}T_xAs_2$ ($T = \mathrm{Co}, \mathrm{Ni}$)," Phys. Rev. B **95**, 060505 (2017).

[80] E. Wiesenmayer, H. Luetkens, G. Pascua, R. Khasanov, A. Amato, H. Potts, B. Banusch, H.-H. Klauss, and D. Johrendt, "Microscopic coexistence of superconductivity and magnetism in $Ba_{1-x}K_xFe_2As_2$," Phys. Rev. Lett. **107**, 237001 (2011).

[81] J. D. Wright, T. Lancaster, I. Franke, A. J. Steele, J. S. Möller, M. J. Pitcher, A. J. Corkett, D. R. Parker, D. G. Free, F. L. Pratt, P. J. Baker, S. J. Clarke, and S. J. Blundell, "Gradual destruction of magnetism in the superconducting family $NaFe_{1-x}Co_xAs$," Phys. Rev. B **85**, 054503 (2012).

[82] S. C. Cheung, Z. Guguchia, B. A. Frandsen, Z. Gong, K. Yamakawa, D. E. Almeida, I. J. Onuorah, P. Bonfá, E. Miranda, W. Wang, D. W. Tam, Y. Song, C. Cao, Y. Cai, A. M. Hallas, M. N. Wilson, T. J. S. Munsie, G. Luke, B. Chen, G. Dai, C. Jin, S. Guo, F. Ning, R. M. Fernandes, R. De Renzi, P. Dai, and Y. J. Uemura, "Disentangling superconducting and magnetic orders in $NaFe_{1-x}Ni_xAs$ using muon spin rotation," Phys. Rev. B **97**, 224508 (2018).

[83] Z. Guguchia, R. Khasanov, Z. Bukowski, F. von Rohr, M. Medarde, P. K. Biswas, H. Luetkens, A. Amato, and E. Morenzoni, "Probing the pairing symmetry in the over-doped Fe-based superconductor $Ba_{0.35}Rb_{0.65}Fe_2As_2$ as a function of hydrostatic pressure," Phys. Rev. B **93**, 094513 (2016).

[84] T. Goko, C. J. Arguello, A. Hamann, T. Wolf, M. Lee, D. Reznik, A. Maisuradze, R. Khasanov, E. Morenzoni, and Y. J. Uemura, "Restoration of quantum critical behavior by disorder in pressure-tuned (Mn,Fe)Si," npj Quantum Materials **2**, 44 (2017).

[85] Y. Song, Z. Yamani, C. Cao, Y. Li, C. Zhang, J. S. Chen, Q. Huang, H. Wu, J. Tao, Y. Zhu, W. Tian, S. Chi, H. Cao, Y.-B. Huang, M. Dantz, T. Schmitt, R. Yu, A. H. Nevidomskyy, E. Morosan, Q. Si, and P. Dai, "A Mott insulator continuously connected to iron pnictide superconductors," Nature Communications **7**, 13879 (2016).

[86] D. R. Parker, M. J. Pitcher, P. J. Baker, I. Franke, T. Lancaster, S. J. Blundell, and S. J. Clarke, "Structure, antiferromagnetism and superconductivity of the layered iron arsenide NaFeAs," Chem. Commun. , 2189–2191 (2009).

[87] G. Tan, Y. Song, C. Zhang, L. Lin, Z. Xu, T. Hou, W. Tian, H. Cao, S. Li, S. Feng, and P. Dai, "Electron doping evolution of structural and antiferromagnetic phase transitions in $NaFe_{1-x}Co_xAs$ iron pnictides," Phys. Rev. B **94**, 014509 (2016).

[88] I. Presniakov, I. Morozov, A. Sobolev, M. Roslova, A. Boltalin, V. Son, O. Volkova, A. Vasiliev, S. Wurmehl, and B. Büchner, "Local structure and hyperfine interactions of 57 Fe in NaFeAs studied by mössbauer spectroscopy," Journal of Physics: Condensed Matter **25**, 346003 (2013).

[89] B. P. P. Mallett, Y. G. Pashkevich, A. Gusev, T. Wolf, and C. Bernhard, "Muon spin rotation study of the magnetic structure in the tetragonal antiferromagnetic state of weakly underdoped $Ba_{1-x}K_xFe_2As_2$," EPL (Europhysics Letters) **111**, 57001 (2015).

[90] Q. Huang, Y. Qiu, W. Bao, M. A. Green, J. W. Lynn, Y. C. Gasparovic, T. Wu, G. Wu, and X. H. Chen, "Neutron-diffraction measurements of magnetic order and a structural transition in the parent $BaFe_2As_2$ compound of feas-based high-temperature superconductors," Phys. Rev. Lett. **101**, 257003 (2008).

[91] M. Rotter, M. Tegel, D. Johrendt, I. Schellenberg, W. Hermes, and R. Pöttgen, "Spin-density-wave anomaly at 140 k in the ternary iron arsenide $BaFe_2As_2$," Phys. Rev. B **78**, 020503 (2008).

[92] N. Qureshi, Y. Drees, J. Werner, S. Wurmehl, C. Hess, R. Klingeler, B. Büchner, M. T. Fernández-Díaz, and M. Braden, "Crystal and magnetic structure of the oxypnictide superconductor $LaFeAsO_{1-x}F_x$: A neutron-diffraction study," Phys. Rev. B **82**, 184521 (2010).

[93] M. A. McGuire, R. P. Hermann, A. S. Sefat, B. C. Sales, R. Jin, D. Mandrus, F. Grandjean, and G. J. Long, "Influence of the rare-earth element on the effects of the structural and magnetic phase transitions in CeFeAsO, PrFeAsO and NdFeAsO," New Journal of Physics **11**, 025011 (2009).

[94] K. Kothapalli, A. E. Böhmer, W. T. Jayasekara, B. G. Ueland, P. Das, A. Sapkota, V. Taufour, Y. Xiao, E. Alp, S. L. Bud'Ko, P. C. Canfield, A. Kreyssig, and A. I. Goldman, "Strong cooperative coupling of pressure-induced magnetic order and nematicity in FeSe," Nature Communications **7**, 12728 (2016).

[95] M. D. Lumsden and A. D. Christianson, "Magnetism in Fe-based superconductors," Journal of Physics: Condensed Matter **22**, 203203 (2010).

[96] E. Bauer, G. Hilscher, H. Michor, C. Paul, Y. Aoki, H. Sato, M. Giovannini, and A. Saccone, "Evolution of ground state properties in novel $Yb_2Pd_2In_{1-x}Sn_x$," Journal of Magnetism and Magnetic Materials **272-276**, 237 – 238 (2004), proceedings of the International Conference on Magnetism (ICM 2003).

[97] E. Bauer, G. Hilscher, H. Michor, C. Paul, Y. Aoki, H. Sato, D. T. Adroja, J.-G. Park, P. Bonville, C. Godart, J. Sereni, M. Giovannini, and A. Saccone, "The magnetic instability of Yb_2Pd_2(In,Sn) in a non-fermi liquid environment," Journal of Physics: Condensed Matter **17**, S999 (2005).

[98] E. Bauer, H. Michor, T. Muramastsu, T. Kanemasa, T. Kagayama, K. shimizu, Y. Aoki, H. sato, and M. Giovannini, "Occurrence of two quantum critical points in $Yb_2Pd_2In_{1-x}Sn_x$ or, Yb systems do not behave mirror-like to Ce compounds," Journal of Optoelectronics and advanced materials **10**, 1633–1638 (2008).

[99] T. Muramatsu, T. Kanemasa, T. Kagayama, K. Shimizu, Y. Aoki, H. Sato, M. Giovannini, P. Bonville, V. Zlatic, I. Aviani, R. Khasanov, C. Rusu, A. Amato, K. Mydeen, M. Nicklas, H. Michor, and E. Bauer, "Reentrant quantum criticality in Yb_2Pd_2Sn," Phys. Rev. B **83**, 180404 (2011).

[100] E. Bauer, R. T. Khan, M. Giovannini, and C. Ritter, "Appearance of long range magnetic order in a nonmagnetic periphery: Yb_2Pd_2(In,Sn)," physica status solidi (b) **247**, 717–719 (2010).

[101] B. H. Bernhard, B. Coqblin, and C. Lacroix, "Frustration in the kondo lattice model: Local versus extended singlet phases," Phys. Rev. B **83**, 214427 (2011).

[102] G. R. Stewart, "Non-fermi-liquid behavior in d- and f-electron metals," Rev. Mod. Phys. **73**, 797–855 (2001).

[103] H. v. Löhneysen, A. Rosch, M. Vojta, and P. Wölfle, "Fermi-liquid instabilities at magnetic quantum phase transitions," Rev. Mod. Phys. **79**, 1015–1075 (2007).

[104] Q. Si and F. Steglich, "Heavy fermions and quantum phase transitions," Science **329**, 1161–1166 (2010).

[105] O. Trovarelli, C. Geibel, S. Mederle, C. Langhammer, F. M. Grosche, P. Gegenwart, M. Lang, G. Sparn, and F. Steglich, "$YbRh_2Si_2$: Pronounced non-fermi-liquid effects above a low-lying magnetic phase transition," Phys. Rev. Lett. **85**, 626–629 (2000).

[106] J. Plessel, M. M. Abd-Elmeguid, J. P. Sanchez, G. Knebel, C. Geibel, O. Trovarelli, and F. Steglich, "Unusual behavior of the low-moment magnetic ground state of $YbRh_2Si_2$ under high pressure," Phys. Rev. B **67**, 180403 (2003).

[107] K. H. J. Buschow, "Intermetallic compounds of rare-earth and $3d$ transition metals," Reports on Progress in Physics **40**, 1179 (1977).

[108] D. Haskel, Y. B. Lee, B. N. Harmon, Z. Islam, J. C. Lang, G. Srajer, Y. Mudryk, K. A. Gschneidner, and V. K. Pecharsky, "Role of ge in bridging ferromagnetism in the giant magnetocaloric $Gd_5(Ge_{1-x}Si_x)_4$ alloys," Phys. Rev. Lett. **98**, 247205 (2007).

[109] T. Takabatake, E. Matsuoka, S. Narazu, K. Hayashi, S. Morimoto, T. Sasakawa, K. Umeo, and M. Sera, "Roles of spin fluctuations and rattling in magnetic and thermoelectric properties of AT_4Sb_12(A=Ca, Sr, Ba, La; T=Fe, Ru, Os)," Physica B: Condensed Matter **383**, 93 – 102 (2006).

[110] B. C. Sales, D. Mandrus, and R. K. Williams, "Filled skutterudite antimonides: A new class of thermoelectric materials," Science **272**, 1325–1328 (1996).

[111] R. Khasanov, Z. Guguchia, A. Maisuradze, D. Andreica, M. Elender, A. Raselli, Z. Shermadini, T. Goko, F. Knecht, E. Morenzoni, and A. Amato, "High pressure research using muons at the Paul Scherrer Institute," High Pressure Research **36**, 140–166 (2016).

[112] Z. Shermadini, R. Khasanov, M. Elender, G. Simutis, Z. Guguchia, K. Kamenev, and A. Amato, "A low-background piston–cylinder-type hybrid high pressure cell for muon-spin rotation/relaxation experiments," High Pressure Research **37**, 449–464 (2017).

[113] A. D. Corso, "Pseudopotentials periodic table: From H to Pu," Computational Materials Science **95**, 337 – 350 (2014).

[114] D. Vanderbilt, "Soft self-consistent pseudopotentials in a generalized eigenvalue formalism," Phys. Rev. B **41**, 7892–7895 (1990).

[115] K. F. Garrity, J. W. Bennett, K. M. Rabe, and D. Vanderbilt, "Pseudopotentials for high-throughput DFT calculations," Computational Materials Science **81**, 446 – 452 (2014).

[116] E. Kucukbenli, M. Monni, B. I. Adetunji, X. Ge, G. A. Adebayo, N. Marzari, S. de Gironcoli, and A. Dal Corso, "Projector augmented-wave and all-electron calculations across the periodic table: a comparison of structural and energetic properties," ArXiv e-prints (2014).

[117] K. Lejaeghere, G. Bihlmayer, T. Björkman, P. Blaha, S. Blügel, V. Blum, D. Caliste, I. E. Castelli, S. J. Clark, A. Dal Corso, S. de Gironcoli, T. Deutsch, J. K. Dewhurst, I. Di Marco, C. Draxl, M. Dułak, O. Eriksson, J. A. Flores-Livas, K. F. Garrity, L. Genovese, P. Giannozzi, M. Giantomassi, S. Goedecker, X. Gonze, O. Grånäs, E. K. U. Gross, A. Gulans, F. Gygi, D. R. Hamann, P. J. Hasnip, N. A. W. Holzwarth, D. Iuşan, D. B. Jochym, F. Jollet, D. Jones, G. Kresse, K. Koepernik, E. Küçükbenli, Y. O. Kvashnin, I. L. M. Locht, S. Lubeck, M. Marsman, N. Marzari, U. Nitzsche, L. Nordström, T. Ozaki, L. Paulatto, C. J. Pickard, W. Poelmans, M. I. J. Probert, K. Refson, M. Richter, G.-M. Rignanese, S. Saha, M. Scheffler, M. Schlipf, K. Schwarz, S. Sharma, F. Tavazza, P. Thunström, A. Tkatchenko, M. Torrent, D. Vanderbilt, M. J. van Setten, V. Van Speybroeck, J. M. Wills, J. R. Yates, G.-X. Zhang, and S. Cottenier, "Reproducibility in density functional theory calculations of solids," Science **351** (2016), 10.1126/science.aad3000.

[118] V. KOPTSIK, "Generalized symmetry in crystal physics," in *Crystal Symmetries*, International Series in Modern Applied Mathematics and Computer Science, edited by I. HARGITTAI and B. VAINSHTEIN (Pergamon, Amsterdam, 1988) pp. 407 – 424.

[119] J. Perez-Mato, S. Gallego, E. Tasci, L. Elcoro, G. de la Flor, and M. Aroyo, "Symmetry-based computational tools for magnetic crystallography," Annual Review of Materials Research **45**, 217–248 (2015).

[120] Bilbao-Crystallogr.-Serv., "MAXMAGN:maximal magnetic space groups for a given propagation vector and resulting magnetic structural models," (2014).

[121] E. Hovestreydt, M. Aroyo, S. Sattler, and H. Wondratschek, " KAREP - a program for calculating irreducible space-group representations," Journal of Applied Crystallography **25**, 544 (1992).

[122] C. M. Aegerter, S. H. Lloyd, C. Ager, S. L. Lee, S. Romer, H. Keller, and E. M. Forgan, "Evidence for a square vortex lattice in Sr_2RuO_4 from muon-spin-rotation measurements," Journal of Physics: Condensed Matter **10**, 7445 (1998).

[123] G. M. Luke, Y. Fudamoto, K. M. Kojima, M. I. Larkin, J. Merrin, B. Nachumi, Y. J. Uemura, Y. Maeno, Z. Q. Mao, Y. Mori, H. Nakamura, and M. Sigrist, "Time-reversal symmetry-breaking superconductivity in Sr_2RuO_4," Nature **394**, 558–561 (1998).

[124] G. Luke, Y. Fudamoto, K. Kojima, M. Larkin, B. Nachumi, Y. Uemura, J. Sonier, Y. Maeno, Z. Mao, Y. Mori, and D. Agterberg, "Unconventional superconductivity in Sr_2RuO_4," Physica B: Condensed Matter **289-290**, 373 – 376 (2000).

[125] S. J. Ray, A. S. Gibbs, S. J. Bending, P. J. Curran, E. Babaev, C. Baines, A. P. Mackenzie, and S. L. Lee, "Muon-spin rotation measurements of the vortex state in Sr_2RuO_4: Type-1.5 superconductivity, vortex clustering, and a crossover from a triangular to a square vortex lattice," Phys. Rev. B **89**, 094504 (2014).

[126] Y. Maeno, H. Hashimoto, K. Yoshida, S. Nishizaki, T. Fujita, J. G. Bednorz, and F. Lichtenberg, "Superconductivity in a layered perovskite without copper," Nature **372**, 532 (1994).

[127] A. P. Mackenzie and Y. Maeno, "The superconductivity of Sr_2RuO_4 and the physics of spin-triplet pairing," Rev. Mod. Phys. **75**, 657–712 (2003).

[128] A. P. Mackenzie, T. Scaffidi, C. W. Hicks, and Y. Maeno, "Even odder after twenty-three years: the superconducting order parameter puzzle of Sr_2RuO_4," npj Quantum Materials **2**, 40 (2017).

[129] T. M. Rice and M. Sigrist, "Sr_2RuO_4 : an electronic analogue of 3He?" Journal of Physics: Condensed Matter **7**, L643 (1995).

[130] I. I. Mazin and D. J. Singh, "Ferromagnetic spin fluctuation induced superconductivity in Sr_2RuO_4," Phys. Rev. Lett. **79**, 733–736 (1997).

[131] K. Deguchi, Z. Q. Mao, and Y. Maeno, "Determination of the superconducting gap structure in all bands of the spin-triplet superconductor Sr_2RuO_4," Journal of the Physical Society of Japan **73**, 1313–1321 (2004).

[132] K. Deguchi, Z. Q. Mao, H. Yaguchi, and Y. Maeno, "Gap structure of the spin-triplet superconductor Sr_2RuO_4 determined from the field-orientation dependence of the specific heat," Phys. Rev. Lett. **92**, 047002 (2004).

[133] K. D. Nelson, Z. Q. Mao, Y. Maeno, and Y. Liu, "Odd-parity superconductivity in Sr_2RuO_4," Science **306**, 1151–1154 (2004).

[134] K. Ishida, Y. K. H. Mukuda, K. Asayama, Z. Q. Mao, Y. Mori, and Y. Maeno, "Superconductivity in a layered perovskite without copper," Nature **396**, 658–660 (1998).

[135] A. P. Mackenzie, R. K. W. Haselwimmer, A. W. Tyler, G. G. Lonzarich, Y. Mori, S. Nishizaki, and Y. Maeno, "Extremely strong dependence of superconductivity on disorder in Sr_2RuO_4," Phys. Rev. Lett. **80**, 161–164 (1998).

[136] J. Xia, Y. Maeno, P. T. Beyersdorf, M. M. Fejer, and A. Kapitulnik, "High resolution polar kerr effect measurements of Sr_2RuO_4: Evidence for broken time-reversal symmetry in the superconducting state," Phys. Rev. Lett. **97**, 167002 (2006).

[137] S. Raghu, A. Kapitulnik, and S. A. Kivelson, "Hidden quasi-one-dimensional superconductivity in Sr_2RuO_4," Phys. Rev. Lett. **105**, 136401 (2010).

[138] E. Pavarini and I. I. Mazin, "First-principles study of spin-orbit effects and nmr in Sr_2RuO_4," Phys. Rev. B **74**, 035115 (2006).

[139] M. W. Haverkort, I. S. Elfimov, L. H. Tjeng, G. A. Sawatzky, and A. Damascelli, "Strong spin-orbit coupling effects on the fermi surface of Sr_2RuO_4 and Sr_2RhO_4," Phys. Rev. Lett. **101**, 026406 (2008).

[140] C. N. Veenstra, Z.-H. Zhu, M. Raichle, B. M. Ludbrook, A. Nicolaou, B. Slomski, G. Landolt, S. Kittaka, Y. Maeno, J. H. Dil, I. S. Elfimov, M. W. Haverkort, and A. Damascelli, "Spin-orbital entanglement and the breakdown of singlets and triplets in Sr_2RuO_4 revealed by spin- and angle-resolved photoemission spectroscopy," Phys. Rev. Lett. **112**, 127002 (2014).

[141] G. Zhang, E. Gorelov, E. Sarvestani, and E. Pavarini, "Fermi surface of Sr_2RuO_4: Spin-orbit and anisotropic coulomb interaction effects," Phys. Rev. Lett. **116**, 106402 (2016).

[142] J. R. Kirtley, C. Kallin, C. W. Hicks, E.-A. Kim, Y. Liu, K. A. Moler, Y. Maeno, and K. D. Nelson, "Upper limit on spontaneous supercurrents in Sr_2RuO_4," Phys. Rev. B **76**, 014526 (2007).

[143] C. W. Hicks, J. R. Kirtley, T. M. Lippman, N. C. Koshnick, M. E. Huber, Y. Maeno, W. M. Yuhasz, M. B. Maple, and K. A. Moler, "Limits on superconductivity-related magnetization in Sr_2RuO_4 and $PrOs_4Sb_{12}$ from scanning squid microscopy," Phys. Rev. B **81**, 214501 (2010).

[144] P. J. Curran, V. V. Khotkevych, S. J. Bending, A. S. Gibbs, S. L. Lee, and A. P. Mackenzie, "Vortex imaging and vortex lattice transitions in superconducting Sr_2RuO_4 single crystals," Phys. Rev. B **84**, 104507 (2011).

[145] K. Miyake and O. Narikiyo, "Model for unconventional superconductivity of Sr_2RuO_4: Effect of impurity scattering on time-reversal breaking triplet pairing with a tiny gap," Phys. Rev. Lett. **83**, 1423–1426 (1999).

[146] A. Steppke, L. Zhao, M. E. Barber, T. Scaffidi, F. Jerzembeck, H. Rosner, A. S. Gibbs, Y. Maeno, S. H. Simon, A. P. Mackenzie, and C. W. Hicks, "Strong peak in T_c of Sr_2RuO_4 under uniaxial pressure," Science **355** (2017), 10.1126/science.aaf9398.

[147] C. W. Hicks, D. O. Brodsky, E. A. Yelland, A. S. Gibbs, J. A. N. Bruin, M. E. Barber, S. D. Edkins, K. Nishimura, S. Yonezawa, Y. Maeno, and A. P. Mackenzie, "Strong increase of tc of Sr_2RuO_4 under both tensile and compressive strain," Science **344**, 283–285 (2014).

[148] G. M. Luke, A. Keren, L. P. Le, W. D. Wu, Y. J. Uemura, D. A. Bonn, L. Taillefer, and J. D. Garrett, "Muon spin relaxation in UPt_3," Phys. Rev. Lett. **71**, 1466–1469 (1993).

[149] R. H. Heffner, J. L. Smith, J. O. Willis, P. Birrer, C. Baines, F. N. Gygax, B. Hitti, E. Lippelt, H. R. Ott, A. Schenck, E. A. Knetsch, J. A. Mydosh, and D. E. MacLaughlin, "New phase diagram for (U,Th) Be13: A muon-spin-resonance and Hc1 Study," in *Ten Years of Superconductivity: 1980–1990*, edited by H. R. Ott (Springer Netherlands, Dordrecht, 1993) pp. 168–171.

[150] R. F. Kiefl, J. H. Brewer, I. Affleck, J. F. Carolan, P. Dosanjh, W. N. Hardy, T. Hsu, R. Kadono, J. R. Kempton, S. R. Kreitzman, Q. Li, A. H. O'Reilly, T. M. Riseman, P. Schleger, P. C. E. Stamp, H. Zhou, L. P. Le, G. M. Luke, B. Sternlieb, Y. J. Uemura, H. R. Hart, and K. W. Lay, "Search for anomalous internal magnetic fields in high-T_c superconductors as evidence for broken time-reversal symmetry," Phys. Rev. Lett. **64**, 2082–2085 (1990).

[151] D. R. Hamann, "Optimized norm-conserving vanderbilt pseudopotentials," Phys. Rev. B **88**, 085117 (2013).

[152] V. G. Storchak, J. H. Brewer, D. G. Eshchenko, P. W. Mengyan, O. E. Parfenov, A. M. Tokmachev, P. Dosanjh, and S. N. Barilo, "Local magnetic order in La_2CuO_4 seen via μ^+SR spectroscopy," Journal of Physics: Conference Series **551**, 012024 (2014).

[153] X.-P. Hao, H.-L. Cui, Z.-L. Lv, and G.-F. Ji, "Electronic and elastic properties of Sr_2RuO_4 with pressure effects by first principles calculation," Physica B: Condensed Matter **441**, 62 – 67 (2014).

[154] T. Oguchi, "Electronic band structure of the superconductor Sr_2RuO_4," Phys. Rev. B **51**, 1385–1388 (1995).

[155] D. J. Singh, "Relationship of Sr_2RuO_4 to the superconducting layered cuprates," Phys. Rev. B **52**, 1358–1361 (1995).

[156] M. Schmidt, T. R. Cummins, M. Bürk, D. H. Lu, N. Nücker, S. Schuppler, and F. Lichtenberg, "Nature of the electronic states in the layered perovskite noncuprate superconductor Sr_2RuO_4," Phys. Rev. B **53**, R14761–R14764 (1996).

[157] E. Daniel and J. Friedel, "Sur la polarisation de spin des electrons de conductibilite dans les metaux ferromagnetiques," J. Phys. Chem. Solids **24**, 1601 (1963).

[158] P. F. Meier, "Electron densities at charged impurities in metals," Helv. Phys. Acta **48** (1975).

[159] B. D. Patterson and J. Keller, "A cluster calculation of the muon hyperfine field in nickel," Hyperfine Interactions **6**, 73–76 (1979).

[160] S. Estreicher, A. Denison, and P. Meier, "Effects of zero-point motion on the hyperfine field at the muon," Hyperfine Interactions **8**, 601–604 (1981).

[161] B. Lindgren and D. E. Ellis, "Hyperfine fields and electronic structure of hydrogen impurities in transition metals," Phys. Rev. B **26**, 636–647 (1982).

[162] K. Terakura, H. Akaia, M. Akai, and J. Kanamori, "The hyperfine field of the positive muons in the ferromagnetic transition metals," in *Electronic Structure and properties of Hydrogen in Metals*, edited by P. J. C.B. Satterthwaite (Plenum Predd, New York, 1983) pp. 413–424.

[163] S. Blügel, H. Akai, R. Zeller, and P. H. Dederichs, "Hyperfine fields of 3*d* and 4*d* impurities in nickel," Phys. Rev. B **35**, 3271–3283 (1987).

[164] P. Jena and M. Manninem, "Theory of impurity hyperfine field systematics in ferromagnetic hosts," Hyperfine Interactions **9**, 405–408 (1981).

[165] F. Mauri, B. G. Pfrommer, and S. G. Louie, "Ab initio theory of NMR chemical shifts in solids and liquids," Phys. Rev. Lett. **77**, 5300–5303 (1996).

[166] C. J. Pickard and F. Mauri, "All-electron magnetic response with pseudopotentials: NMR chemical shifts," Phys. Rev. B **63**, 245101 (2001).

[167] M. d'Avezac, N. Marzari, and F. Mauri, "Spin and orbital magnetic response in metals: Susceptibility and NMR shifts," Phys. Rev. B **76**, 165122-165134 (2007).

[168] R. Laskowski and P. Blaha, "NMR Shielding in Metals Using the Augmented Plane Wave Method," J. Phys. Chem. C **119**, 19390–19396 (2015).

[169] M. Nusair, L. Wilk, and S. H. Vosko, "A comparison of spin-density functional calculations for the knight shift in Mg," Journal of Physics F: Metal Physics **11**, 1683 (1981).

[170] E. Pavarini and I. I. Mazin, "NMR relaxation rates and knight shifts in mgb_2," Phys. Rev. B **64**, 140504 (2001).

[171] O. V. Yazyev, Ivano, H. L. Tavernelli, and U. Röthlisberger, "Core spin-polarization correction in pseudopotential-based electronic structure calculations," Phys. Rev. B **71**, 115110 (2005).

[172] M. S. Bahramy, M. H. F. Sluiter, and Y. Kawazoe, "Pseudopotential hyperfine calculations through perturbative core-level polarization," Phys. Rev. B **76**, 035124 (2007).

[173] G. Breit, "Possible effects of nuclear spin on x-ray terms," Phys. Rev. **35**, 1447–1451 (1930).

[174] M. Battocletti, H. Ebert, and H. Akai, "Influence of gradient corrections to the local-density-approximation on the calculation of hyperfine fields in ferromagnetic Fe, Co, and Ni," Phys. Rev. B **53**, 9776–9783 (1996).

[175] N. Nishida, R. S. Hayano, K. Nagamine, T. Yamazaki, J. H. Bewer, D. M. Garner, D. Fleming, T. Takeuchi, and Y. Ishikawa, "Hyperfine field and diffusion of μ^+ in Fe single crystals," Solid State communications **22**, 235–239 (1977).

[176] H. Graf, W. Kündig, B. D. Patterson, W. Reichart, P. Roggwiller, M. Camani, F. N. Gygax, W. Rüegg, A. Schenck, H. Schilling, and P. F. Meier, "Local magnetic field at a positive muon in ferromagnetic cobalt," Phys. Rev. Lett. **37**, 1644–1647 (1976).

[177] H. Graf, E. Holzschuh, E. Recknagel, A. Weidinger, and T. Wichert, "Diffusion of positive muons in Nickel and Iron," Hyperfine Interactions **6**, 245–249 (1979).

[178] C. Kittel, *Introduction to Solid State Physics*, 7th ed. (John Wiley and Sons, Inc, United States of America, 1996).

[179] D. Sanchez-Portal, E. Artacho, and J. M. Solerab, "Projection of plane-wave calculations into atomic orbitals," Solid State Communications **95**, 685–690 (1995).

[180] S. Estreicher and P. F. Meier, "Hyperfine fields at impurities in ferromagnetic metals," Phys. Rev. B **25**, 297–310 (1982).

[181] M. Deutsch, O. L. Makarova, T. C. Hansen, M. T. Fernandez-Diaz, V. A. Sidorov, A. V. Tsvyashchenko, L. N. Fomicheva, F. Porcher, S. Petit, K. Koepernik, U. K. Rößler, and I. Mirebeau, "Two-step pressure-induced collapse of magnetic order in the MnGe chiral magnet," Phys. Rev. B **89**, 180407 (2014).

[182] Y. Ishikawa, K. Tajima, D. Bloch, and M. Roth, "Helical spin structure in manganese silicide MnSi," Solid State Communications **19**, 525–528 (1976).

[183] O. L. Makarova, A. V. Tsvyashchenko, G. Andre, F. Porcher, L. N. Fomicheva, N. Rey, and I. Mirebeau, "Neutron diffraction study of the chiral magnet MnGe," Phys. Rev. B **85**, 205205 (2012).

[184] T. Jeong and W. E. Pickett, "Implications of the b20 crystal structure for the magnetoelectronic structure of MnSi," Phys. Rev. B **70**, 075114 (2004).

[185] F. Carbone, M. Zangrando, A. Brinkman, A. Nicolaou, F. Bondino, E. Magnano, A. A. Nugroho, F. Parmigiani, T. Jarlborg, and D. van der Marel, "Electronic structure of MnSi: The role of electron-electron interactions," Phys. Rev. B **73**, 085114 (2006).

[186] R. Collyer and D. Browne, "Correlations and the magnetic moment of MnSi," Physica B: Condensed Matter **403**, 1420 – 1422 (2008).

[187] K. V. Shanavas and S. Satpathy, "Electronic structure and the origin of the dzyaloshinskii-moriya interaction in MnSi," Phys. Rev. B **93**, 195101 (2016).

[188] J. Keller, "Cluster method to study the electronic strucutre of condensed matter," Hyperfine Interactions **6**, 15–23 (1979).

[189] L. Ortenzi, I. I. Mazin, P. Blaha, and L. Boeri, "Accounting for spin fluctuations beyond local spin density approximation in the density functional theory," Phys. Rev. B **86**, 064437 (2012).

[190] T. Moriya and A. Kawabata, "Effect of spin fluctuations on itinerant electron ferromagnetism," J. Phys. Soc. Jpn. **34**, 639–651 (1973).

[191] T. Moriya and Y. Takahashi, "Itinerant electron magnetism," Annual Review of Materials Science **14**, 1–25 (1984).

[192] T. Moriya, *Spin Fluctuations in Itinerant Electron Magnetism* (Springer-Verlag Berlin Heidelberg, New York, 1985).

[193] A. R. Porter, M. D. Towler, and R. J. Needs, "Muonium as a hydrogen analogue in silicon and germanium: Quantum effects and hyperfine parameters," Phys. Rev. B **60**, 13534–13546 (1999).

[194] M. J. Stott and P. Kubica, "New approach to the positron distribution in metals and alloys," Phys. Rev. B **11**, 1–10 (1975).

[195] I. Errea, M. Calandra, and F. Mauri, "First-principles theory of anharmonicity and the inverse isotope effect in superconducting palladium-hydride compounds," Phys. Rev. Lett. **111**, 177002 (2013).

[196] I. Errea, M. Calandra, and F. Mauri, "Anharmonic free energies and phonon dispersions from the stochastic self-consistent harmonic approximation: Application to platinum and palladium hydrides," Phys. Rev. B **89**, 064302 (2014).

[197] I. Errea, M. Calandra, C. J. Pickard, J. Nelson, R. J. Needs, Y. Li, H. Liu, Y. Zhang, Y. Ma, and F. Mauri, "High-pressure hydrogen sulfide from first principles: A strongly anharmonic phonon-mediated superconductor," Phys. Rev. Lett. **114**, 157004 (2015).

[198] A. V. Soudackov and S. Hammes-Schiffer, "Removal of the double adiabatic approximation for proton-coupled electron transfer reactions in solution," Chemical Physics Letters **299**, 503 – 510 (1999).

[199] A. Isihara, "The Gibbs-Bogoliubov inequality dagger," Journal of Physics A: General Physics **1**, 539 (1968).

[200] J. K. L. MacDonald, "Successive Approximations by the Rayleigh-Ritz Variation Method," Phys. Rev. **43**, 830–833 (1933).

[201] M. R. Hestenes and E. Stiefel, "Methods of conjugate gradients for solving linear systems," Journal of research of the National Bureau of Standards **49**, 409–436 (1952).

[202] G. Lang, K. Karch, M. Schmitt, P. Pavone, A. P. Mayer, R. K. Wehner, and D. Strauch, "Anharmonic line shift and linewidth of the raman mode in covalent semiconductors," Phys. Rev. B **59**, 6182–6188 (1999).

[203] B. Rousseau and A. Bergara, "Giant anharmonicity suppresses superconductivity in AlH_3 under pressure," Phys. Rev. B **82**, 104504 (2010).

[204] I. Errea, B. Rousseau, and A. Bergara, "Anharmonic stabilization of the high-pressure simple cubic phase of calcium," Phys. Rev. Lett. **106**, 165501 (2011).

[205] H. Kahn, "Random Sampling (Monte Carlo) Techniques in Neutron Attenuation Problems. I," Nucleonics (U.S.) **6** (1950).

[206] G. Kresse, J. Furthmüller, and J. Hafner, "Ab initio force constant approach to phonon dispersion relations of diamond and graphite," EPL (Europhysics Letters) **32**, 729 (1995).

[207] K. Parlinski, Z. Q. Li, and Y. Kawazoe, "First-principles determination of the soft mode in cubic ZrO_2," Phys. Rev. Lett. **78**, 4063–4066 (1997).

[208] S. Y. Savrasov, D. Y. Savrasov, and O. K. Andersen, "Linear-response calculations of electron-phonon interactions," Phys. Rev. Lett. **72**, 372–375 (1994).

[209] S. Baroni, S. de Gironcoli, A. Dal Corso, and P. Giannozzi, "Phonons and related crystal properties from density-functional perturbation theory," Rev. Mod. Phys. **73**, 515–562 (2001).

[210] P. Pulay, "Ab initio calculation of force constants and equilibrium geometries in polyatomic molecules," Molecular Physics **17**, 197–204 (1969).

[211] M. Ando, K. Kadono, M. Haruta, T. Sakaguchi, and M. Miya, "Large third-order optical nonlinearities in transition-metal oxides," nature **374**, 625–627 (1995).

[212] H. J. Kulik and N. Marzari, "Systematic study of first-row transition-metal diatomic molecules: A self-consistent DFT+U approach," The Journal of Chemical Physics **133**, 114103 (2010), https://doi.org/10.1063/1.3489110 .

[213] A. Floris, S. de Gironcoli, E. K. U. Gross, and M. Cococcioni, "Vibrational properties of MnO and NiO from DFT + U-based density functional perturbation theory," Phys. Rev. B **84**, 161102 (2011).

[214] C. Rodl and F. Bechstedt, "Optical and energy-loss spectra of the antiferromagnetic transition metal oxides MnO, FeO, CoO, and NiO including quasiparticle and excitonic effects," Phys. Rev. B **86**, 235122 (2012).

[215] W. L. Roth, "Defects in the crystal and magnetic structures of ferrous oxide," Acta Crystallographica **13**, 140–149 (1960).

[216] Manenc, J., "Existence d'une surstructure dans le protoxyde de fer," J. Phys. France **24**, 447–450 (1963).

[217] P. G. Dickens, R. Heckingbottom, and J. W. Linnett, "Calculation of the heats of formation of point defects in some transition metal oxides," Trans. Faraday Soc. **64**, 1489–1498 (1968).

[218] F. Koch and J. B. Cohen, "The defect structure of $Fe_{1-x}O$," Acta Crystallographica Section B **25**, 275–287 (1968).

[219] C. R. A. Catlow, W. C. Mackrodt, M. J. Norgett, and A. M. Stoneham, "The basic atomic processes of corrosion i. electronic conduction in MnO, CoO and NiO," The Philosophical Magazine: A Journal of Theoretical Experimental and Applied Physics **35**, 177–187 (1977).

[220] R. M. Hazen and R. Jeanloz, "Wüstite ($Fe_{1-x}O$): A review of its defect structure and physical properties," Reviews of Geophysics **22**, 37–46 (1984).

[221] R. W. GRIMES, A. B. ANDERSON, and A. H. HEUER, "Defect clusters in nonstoichiometric 3d transition-metal monoxides," Journal of the American Ceramic Society **69**, 619–623 (1986).

[222] CATLOW, C. R. A., FENDER, B., and MUXWORTHY, D. G., "Defect interactions and order-disorder in transition metal oxides," J. Phys. Colloques **38** (1977), 10.1051/jphyscol:1977713.

[223] M. V. Ganduglia-Pirovano, A. Hofmann, and J. Sauer, "Oxygen vacancies in transition metal and rare earth oxides: Current state of understanding and remaining challenges," Surface Science Reports **62**, 219 – 270 (2007).

[224] M. C. Toroker, D. K. Kanan, N. Alidoust, L. Y. Isseroff, P. Liao, and E. A. Carter, "First principles scheme to evaluate band edge positions in potential transition metal oxide photocatalysts and photoelectrodes." Physical chemistry chemical physics : PCCP **13 37**, 16644–54 (2011).

[225] J. Kim, B. Hou, C. Park, C. B. Bahn, J. P. Hoffman, J. M. Black, A. Bhattacharya, N. Balke, H. Hong, J. H. Kim, and S. Hong, "Effect of defects on reaction of NiO surface with Pb-contained solution," Scientific reports **7** (2017).

[226] A. S. M. Jonayat, A. Kramer, L. Bignardi, P. Lacovig, S. Lizzit, A. C. van Duin, M. Batzill, and M. J. Janik, "A first-principles study of stability of surface confined mixed metal oxides with corundum structure (Fe_2O_3, Cr_2O_3, V_2O_3)," Phys. Chem. Chem. Phys. **20**, 7073–7081 (2018).

[227] A. L. Tiano, J.-b. Li, E. Sutter, S. S. Wong, and M.-V. Fernández-Serra, "Effects of electronic correlation, physical structure, and surface termination on the electronic structure of V_2O_3 nanowires," Phys. Rev. B **86**, 125135 (2012).

[228] C. G. Van de Walle, "Structural identification of hydrogen and muonium centers in silicon: First-principles calculations of hyperfine parameters," Phys. Rev. Lett. **64**, 669–672 (1990).

[229] R. C. Vilão, J. M. Gil, A. Weidinger, H. V. Alberto, J. Piroto Duarte, N. Ayres de Campos, R. L. Lichti, K. H. Chow, S. P. Cottrell, and S. F. J. Cox, "Acceptor level of interstitial muonium in ZnSe and ZnS," Phys. Rev. B **77**, 235212 (2008).

[230] J. M. Gil, H. V. Alberto, R. C. Vilão, J. Piroto Duarte, P. J. Mendes, L. P. Ferreira, N. Ayres de Campos, A. Weidinger, J. Krauser, C. Niedermayer, and S. F. J. Cox, "Novel muonium state in CdS," Phys. Rev. Lett. **83**, 5294–5297 (1999).

[231] S. F. J. Cox, E. A. Davis, S. P. Cottrell, P. J. C. King, J. S. Lord, J. M. Gil, H. V. Alberto, R. C. Vilão, J. Piroto Duarte, N. Ayres de Campos, A. Weidinger, R. L. Lichti, and S. J. C. Irvine, "Experimental confirmation of the predicted shallow donor hydrogen state in zinc oxide," Phys. Rev. Lett. **86**, 2601–2604 (2001).

[232] J. Lord, S. Cottrell, P. King, H. Alberto, N. A. de Campos, J. Gil, J. Duarte, R. Vilão, R. Lichti, S. Sjue, B. Bailey, A. Weidinger, E. Davis, and S. Cox, "Probing the shallow-donor muonium wave function in ZnO and CdS via transferred hyperfine interactions," Physica B: Condensed Matter **308-310**, 920 – 923 (2001), international Conference on Defects in Semiconductors.

[233] K. C. B. Chan, R. L. Lichti, C. Boekema, A. B. Denison, D. W. Cooke, and M. E. Schillaci, "Muon-oxygen bonding in V_2O_3," Hyperfine Interactions **31**, 481–486 (1986).

[234] A. G. Marinopoulos, "Incorporation and migration of hydrogen in yttria-stabilized cubic zirconia: Insights from semilocal and hybrid-functional calculations," Phys. Rev. B **86**, 155144 (2012).

[235] E. L. da Silva, A. G. Marinopoulos, R. B. L. Vieira, R. C. Vilão, H. V. Alberto, J. M. Gil, R. L. Lichti, P. W. Mengyan, and B. B. Baker, "Electronic structure of interstitial hydrogen in lutetium oxide from DFT+U calculations and comparison study with μSR spectroscopy," Phys. Rev. B **94**, 014104 (2016).

[236] L.-B. Mo, Y. Wang, Y. Bai, Q.-Y. Xiang, Q. Li, W.-Q. Yao, J.-O. Wang, K. Ibrahim, H.-H. Wang, C.-H. Wan, and J.-L. Cao, "Hydrogen Impurity Defects in Rutile TiO_2," Scientific Reports **5**, 17634 (2015).

[237] B. D. Patterson, "Muonium states in semiconductors," Rev. Mod. Phys. **60**, 69–159 (1988).

[238] R. C. Vilão, R. B. L. Vieira, H. V. Alberto, J. M. Gil, A. Weidinger, R. L. Lichti, B. B. Baker, P. W. Mengyan, and J. S. Lord, "Muonium donor in rutile TiO_2 and comparison with hydrogen," Phys. Rev. B **92**, 081202 (2015).

[239] K. Nishiyama, S. Ohira, W. Dawson, and W. Higemoto, "Low temperature μSR studies in NiO and CoO," Hyperfine Interactions **104**, 349–355 (1997).

[240] W. L. Roth, "Magnetic structures of MnO, FeO, CoO, and NiO," Phys. Rev. **110**, 1333–1341 (1958).

[241] A. K. Cheetham and D. A. O. Hope, "Magnetic ordering and exchange effects in the antiferromagnetic solid solutions $Mn_xNi_{1-x}O$," Phys. Rev. B **27**, 6964–6967 (1983).

[242] C. G. Shull, W. A. Strauser, and E. O. Wollan, "Neutron diffraction by paramagnetic and antiferromagnetic substances," Phys. Rev. **83**, 333–345 (1951).

[243] A. Schrön, C. Rödl, and F. Bechstedt, "Energetic stability and magnetic properties of MnO in the rocksalt, wurtzite, and zinc-blende structures: Influence of exchange and correlation," Phys. Rev. B **82**, 165109 (2010).

[244] A. Schrön, C. Rödl, and F. Bechstedt, "Crystalline and magnetic anisotropy of the 3*d*-transition metal monoxides MnO, FeO, CoO, and NiO," Phys. Rev. B **86**, 115134 (2012).

[245] C. Rödl, F. Fuchs, J. Furthmüller, and F. Bechstedt, "Quasiparticle band structures of the antiferromagnetic transition-metal oxides MnO, FeO, CoO, and NiO," Phys. Rev. B **79**, 235114 (2009).

[246] G. Trimarchi, Z. Wang, and A. Zunger, "Polymorphous band structure model of gapping in the antiferromagnetic and paramagnetic phases of the mott insulators MnO, FeO, CoO, and NiO," Phys. Rev. B **97**, 035107 (2018).

[247] C. G. Van de Walle and J. Neugebauer, "Universal alignment of hydrogen levels in semiconductors, insulators and solutions," Nature **423**, 626–628 (2003).

[248] A. A. Frost, R. E. Kellogg, B. M. Gimarc, and J. D. Scargle, "Least-squares local-energy method for molecular energy calculations using gauss quadrature points," The Journal of Chemical Physics **35**, 827–831 (1961).

[249] C. G. Van de Walle and J. Neugebauer, "Hydrogen in semiconductors," Annual Review of Materials Research **36**, 179–198 (2006).

[250] C. G. V. de Walle, "Universal alignment of hydrogen levels in semiconductors and insulators," Physica B: Condensed Matter **376-377**, 1 – 6 (2006), proceedings of the 23rd International Conference on Defects in Semiconductors.

[251] A. Mellergård, R. L. McGreevy, A. Wannberg, and B. Trostell, "Modelling of lattice and magnetic thermal disorder in manganese oxide," Journal of Physics: Condensed Matter **10**, 9401 (1998).

[252] A. L. Goodwin, M. G. Tucker, M. T. Dove, and D. A. Keen, "Magnetic structure of MnO at 10 k from total neutron scattering data," Phys. Rev. Lett. **96**, 047209 (2006).

[253] A. J. Steele, *Quantum magnetism probed with muon-spin relaxation*, Ph.D. thesis, University of Oxford (2011).

Acknowledgment

I am thankful to God and nature for the good health and sound mind all these years and also for the luck to cross paths with people that made this academic journey possible.

I am grateful to the administration of the Department of Physics, University of Parma, for the great opportunity to be able to carry out this research.

I express my deepest appreciation to Prof. Roberto De Renzi under whose supervision and guidance I completed this thesis. I am grateful to Roberto for allowing me to tap in his wealth of scientific experience and attitude towards solving scientific problems. I have really learnt a lot during these research years. Also, I appreciate a lot his efforts in helping me sort out domestic issues especially those of accommodation and requirements of permit to live in Parma.

I am grateful to Dr. Pietro Bonfá for the useful scientific discussions and also for his help in sorting out accommodation problems when I first arrived Parma. I also acknowledge his efforts and earlier research that served as the foundation for the completion of this work.

I thank Dr. Ion Errea for always being available for discussions and for insights on phonon calculations. I also thank him for making my visits to Donostia International Physics Center at San Sebastián happen. I can't forget in a hurry the nice memories at San Sebastein.

I will also like to appreciate Dr. Gianrico Lamura and Dr. Toni Shiroka for their guidance and discussion on my first μSR measurements and their constant availability for discussions and collaborations.

I am still grateful to Dr. Nicola Seriani for supervising and directing my early research years at International Centre for Theoretical Physics.

I thank the μSR group under Dr. Alex Amato and also Dr. Rustem Khasanov for accommodating me at the Paul Scherrer Institut, Switzerland and also for the supercomputer access.

I wouldn't fail to acknowledge my parents for sacrificing a lot to ensure that my siblings and I, have quality education that availed the foundation for this research. I am also much grateful to Ebere for always being there for me.

Also, I would like to mention Riaz and Michele for the loud chats at lunch time that ease a lot the stress, also including Anjali, Asha and Victor for the nice boredom relieving weekend outings.

List of Publications

- **Ifeanyi John Onuorah**, Pietro Bonfà, Roberto De Renzi, **"Muon contact hyperfine field in metals: A DFT calculation",** Phy. Rev. B 97, 174414, (2018)
- Sky C. Cheung, Zurab Guguchia, Benjamin A. Frandsen, Zizhou Gong, Kohtaro Yamakawa, Dalson E. Almeida, **Ifeanyi J. Onuorah**, Pietro Bonfà, Eduardo Miranda, Weiyi Wang, David W. Tam, Yu Song, Chongde Cao, Yipeng Cai, Alannah M. Hallas, Murray N. Wilson, Timothy J.S. Munsie, Graeme Luke, Bijuan Chen, Guangyang Dai, Changqing Jin, Shengli Guo, Fanlong Ning, Rafael M. Fernandes, Roberto De Renzi, Pengcheng Dai, and Yasutomo J. Uemura, **"Disentangling superconducting and magnetic orders in NaFe1-xNixAs using muon spin rotation"**, Phys. Rev. B 97, 224508, (2018)
- Pietro Bonfà, **Ifeanyi John Onuorah**, Roberto De Renzi, **"Introduction and a Quick Look at MUESR, the Magnetic Structure and mUon Embedding Site Refinement Suite"** JPS Conf. Proc. 21, 011052 (2018)
- Pietro Bonfà, **Ifeanyi John Onuorah**, Roberto De Renzi, **'First-principles investigation of MnP magnetic states precursors of superconductivity under high pressure'**, arxiv.org/abs/1603.08891, (2016)

Publications still in progress:

- **Ifeanyi John Onuorah**, Pietro Bonfà, Ion Errea, Matteo Calandra, Roberto De Renzi, **"Quantum muon effects within a stochastic self-consistent harmonic approach"**, manuscript
- **Ifeanyi John Onuorah**, Pietro Bonfà, Roberto De Renzi, **"Hydrogen defect levels and muon local field parameters in NiO and MnO"**, manuscript
- Gianrico Lamura, Toni Shiroka, **Ifeanyi John Onuorah**, Pietro Bonfà, Roberto De Renzi, E. Bauer, *et . al* **"Multiple quantum criticality in the phase diagram of Yb2Pd2In1-xSnx heavy fermion"**, manuscript

Copyright Permissions

- Contents of Sec 4.2 including figures 4.3, 4.4, 4.5 and 4.7 were reproduced with permission from:[Phys. Rev. B 97, 224508 (2018)]. Copyright (2018) by the American Physical Society.
- Contents of Chapter 5 including figures 5.1, 5.2, 5.4 and 5.3 were reproduced with permission from:[Phys. Rev. B. (2018)]. Copyright (2018) by the American Physical Society.